NASA TM X-? 70648

RESULTS OF THE U.S. CONTRIBUTION TO THE JOINT U.S./U.S.S.R. BERING SEA EXPERIMENT

MAY 1974
REVISED JUNE 1974

GSFC —— **GODDARD SPACE FLIGHT CENTER**
GREENBELT, MARYLAND

For information concerning availability
of this document contact:

Technical Information Division, Code 250
Goddard Space Flight Center
Greenbelt, Maryland 20771

(Telephone 301-982-4488)

RESULTS OF THE U.S. CONTRIBUTION TO THE JOINT U.S./U.S.S.R. BERING SEA EXPERIMENT

W. J. Campbell
T. C. Chang
M. G. Fowler
P. Gloersen
P. M. Kuhn
R. O. Ramseier
D. B. Ross
G. Stambach
W. J. Webster, Jr., and
T. T. Wilheit

May 1974

GODDARD SPACE FLIGHT CENTER
Greenbelt, Maryland

RESULTS OF THE U.S. CONTRIBUTION TO THE JOINT U.S./U.S.S.R. BERING SEA EXPERIMENT

FOREWORD

The six papers reproduced here contain results of the U.S. contribution to the joint U.S./U.S.S.R. Bering Sea Expedition, conducted by the two countries during the period 15 February - 10 March 1973.

These results will be compared to and integrated with similar results obtained by the U.S.S.R. during a joint scientific Symposium to be held in Leningrad during the week 13-17 May 1974. Subsequently, the Proceedings of the Symposium, containing a report of the total results of the joint experiment, will be published in Leningrad.

The authors felt that, because of the success of this unique joint venture, the immediate compilation of these papers into a preprint volume would be of considerable interest, pending the subsequent publication of the formal Proceedings.

CONTENTS

PAPER NO. 1

SYNOPTIC ICE DYNAMICS AND ATMOSPHERIC CIRCULATION
DURING THE BERING SEA EXPERIMENT

W. J. Campbell*

P. Gloersen†

R. O. Ramseier‡

*U.S. Geological Survey, Ice Dynamics Project, Tacoma, Washington

†National Aeronautics and Space Administration, Goddard Space Flight
Center, Greenbelt, Maryland

‡Department of the Environment, 562 Booth Street, Ottawa, Ontario,
K1A OE7, CANADA

Paper No. 1

SYNOPTIC ICE DYNAMICS AND ATMOSPHERIC CIRCULATION DURING THE BERING SEA EXPERIMENT

W. J. Campbell

P. Gloersen

R. O. Ramseier

ABSTRACT

The atmospheric circulation which occurred during the Bering Sea Experiment, 15 February to 10 March 1973, in and around the experiment area is analyzed and related to the macroscale morphology and dynamics of the sea ice cover. The ice cover was very complex in structure, being made up of five ice types, and underwent strong dynamic activity. Synoptic analyses show that an optimum variety of weather situations occurred during the experiment: an initial strong anticyclonic period (6 days), followed by a period of strong cyclonic activity (6 days), followed by weak anticyclonic activity (3 days), and finally a period of weak cyclonic activity (4 days). The data of the mesoscale test areas observed on the four sea ice option flights and ship weather and drift data give a detailed description of mesoscale ice dynamics which correlates well with the macroscale view: anticyclonic activity advects the ice southward with strong ice divergence and a regular lead and polynya pattern; cyclonic activity advects the ice northward with ice convergence, or slight divergence, and a random lead and polynya pattern.

SYNOPTIC ICE DYNAMICS AND ATMOSPHERIC CIRCULATION DURING THE BERING SEA EXPERIMENT

1.1 INTRODUCTION

Nature cooperated with the planners of the Bering Sea Experiment in that strong cyclonic activity occurred in the test area at the time of the experiment so that high sea state, pronounced sea ice formation and motion, and precipitating storm clouds could be observed by remote sensing aircraft and surface ships. Indeed, greater than normal baroclinic activity occurred in the test region during February-March 1973 in that the mean position of the North Pacific polar front was shifted so that its eastern end was not in its normal position in the Gulf of Alaska, but in the Bering Sea. In March the mean-monthly surface pressure of the Aleutian low had a negative pressure anomaly of 10 mb compared to the many-year average.

The rapid motion of cyclones through and along the southern edge of the test area during the experiment period resulted in a pronounced variety of weather conditions. High pressure ridge weather, which occurred with the development of ridges following the passages of cyclones, was characterized by good visibility, clear skies, cold air, and light winds. The cyclonic weather was characterized by poor visibility, low precipitating clouds, high winds, and warmer temperatures. By being able to stagger the remote sensing flights for the three experimental options it was possible to blend each mission with the varying weather conditions so as to obtain the optimum amount of sequential data.

In order to discuss most efficiently the atmospheric circulation during BESEX, we have decided to show the surface synoptic analysis for each day of

the experiment over an area including the Bering Sea and its surrounding land and water masses. These analyses are shown sequentially from 1200 AST, 15 February 1973 (0000 GMT, 16 February) to 1200 AST, 9 March 1973 (0000 GMT, 10 March) in Figures 1.1 through 1.6. (All times and dates given on these analyses are in GMT.) In the following discussion key aspects of the meteorological regime will be alluded to as well as significant events aloft. For each of the days on which a sea ice option was performed (15, 20, 28 February, 5 March) an ice distribution chart of the Bering Sea will be presented (Figures 1.7 through 1.10) and the synoptic situation for each of these days will be discussed in some detail in conjunction with ship weather data acquired by the USCGC Staten Island.

1.2 MACROSCALE SYNOPTICS, ICE MORPHOLOGY, AND ICE DYNAMICS

A well-developed ice cover existed in the Bering Sea at the start of the Bering Sea Experiment. The ice chart for 15 February 1973, the day the first sea ice option was performed, is shown in Figure 1.7. In this analysis, as well as those for the three following ice distribution analyses shown in Figures 1.8, 1.9, and 1.10, we divide the ice into five categories: 1) grey ice, in the order of 20 cm thickness; 2) grey-white ice, in the order of 40 cm thickness; 3) predominantly white ice, also referred to in the following papers as thin white ice, in the order of 60 cm thickness; 4) white and first-year ice, also referred to in the following papers as thick white ice, in the order of 100 cm thickness; 5) transition zone ice, usually made up of frazil ice, grease ice, and small pancake ice.

All of the ice observations give a picture of the formation and motion of the ice cover that essentially fits the following model: most of the ice is formed in

the Bering Sea, with only small amounts being advected south through the Bering Straits; the extension of the ice cover to the south occurs by the drift of a pack that undergoes gradual expansion by having new ice added to it, mainly by freezing of new ice in the ice divergent zones in its northern part, freezing in the leads and polynyas within the pack as it undergoes a stretching deformation under the action of the generally southerly flowing winds, and slow ice growth in the vertical by heat conduction through the pack; the advance south of the pack is due to ice advection rather than ice formation on the edge of the pack.

The character of the edge of the pack, which we refer to as the transition zone, was quite complex. During most of the Bering Sea Experiment, the flow of surface air was generally from the north, as can be seen by scanning the surface synoptic charts shown in Figures 1-16. Therefore, most of the time the pack was in a stretching deformational mode and was extending to the south along its entire width, even in its eastern section where the surface currents flow to the northeast. During these times, the ice in the transition zone was made up of long plumes or bands of a mixture of frazil, grease, and small pancake ice. The plumes were generally oriented about 45° to the left of the surface wind vector and were quite extensive with common lengths of several kilometers. They were not at all rigid, since as sea surface wave trains passed through them they rode over the waves as a fluid, yet after long periods of strong off-pack winds the zone did not detach itself from the main pack. Also, the size of the zone remained relatively constant throughout the experiment.

On 15 February and for the four preceeding days, moderate (10 m/sec) winds blew from the NE over the major part of the Bering Sea ice cover as a result of the interaction of a large, stable anticyclone over Kolyma and a series

5

of small, shallow transient cyclones passing eastward over the Aleutians. This flow of cold air from the north caused a superadiabatic temperature gradient to be established in the lower half kilometer of the troposphere over the ice cover and south of it. Therefore, strong forced convection and vertical advection of moisture resulted in the formation of roll vortex clouds starting at the transition zone and extending south for hundreds of kilometers. Although this layer was shallow, considerable snow was generated.

This strong flow of surface winds from the NE for five days advected most of the thick ice cover to the SW and large new zones of grey ice were formed south of the Chukotsky and Seward Peninsulas, in Norton Sound and adjacent to SW Alaska. As can be seen in Figure 1.7, the character of the ice cover was quite complex, especially in the vicinity of St. Lawrence Island. The dominant lead and polynya orientation in the band of white and first-year and predominantly white ice that runs SE from the Gulf of Anadyr into Bristol Bay was from ESE-WNW, which indicates that the pack was undergoing stretching deformation with the principal strain axis running from SSW to NNE.

During the period 16-18 February the synoptic situation over the experiment area continued as it was earlier with deeper cyclones over the Aleutians and with a slowly shrinking anticyclone over Kolyma. The continued NE surface winds maintained the superadiabatic lapse rates in the near surface layer, and the low, precipitating roll vortex clouds continued over and south of the transition zone. The ice pack continued to be advected to the SW.

The second sea ice option was performed on 20 February when weak N winds were flowing over the test area. The ice distribution chart for this data (Figure 1.8) shows that the entire pack was advected SW from its position on

15 February and that much of the grey ice had matured into grey-white ice. However, fresh zones of grey ice had formed in the divergent areas south of the Chuckotsky and Seward Peninsulas, in Norton Sound and off SW Alaska. As in the case of 15 February, these grey ice zones formed in the zones stripped of older ice by the SW advecting pack.

An accurate measurement of the ice drift vector within the test area was made each night by the USCGC Staten Island. The ship used no propulsive power at night and drifted with the pack; by taking numerous navigational fixes, the night-time drift of the pack could be deduced. These results are shown in Figure 1.13 and Table 1.1. During the night of 19/20 February the pack drifted S with a velocity of 1.5 km/hr.

The lead and polynya patterns of the 20 February ice cover were more complex than on 15 February, with orthogonal arrays of openings with NW-SE and NE-SW orientations. The deformational mode of the test areas will be discussed later in detail.

A marked change in the synoptic situation started on 21 February when a large cyclone moved into the SW corner of the experiment area, displacing the Kolyma anticyclone. This cyclone proceeded through the area (see Figures 1.2 and 1.3) causing a strong flow of ocean air from the SW over the ice cover, filled slowly and passed out of the test area on 24 February, only to be replaced by another strong cyclone which entered the area on 25 February. The rapid change of surface weather conditions in the test area can best be noted in Figure 1.12, showing the temperature and wind data obtained from the USCG Staten Island. The wind shift from NE to SE brought warm air over the test area with a dramatic raise in temperature of 14°C. The relative humidity of this ocean

7

air was high (80-98%) and considerable low level fog formed. Aloft the temperature and humidity also increased up to the 3 km level, the low level inversion disappeared, and a dense layer of nimbostratus formed.

This week-long period of cyclonic weather over the test site ended on 28 February when a high pressure ridge (see Figure 1.4) extended from the Siberian anticyclone into the Bering Sea, establishing once again over the test area a flow of cooler surface air from the NE (see Figure 1.12). This ridge persisted until 2 March.

The third sea ice option was flown on 28 February and the ice distribution chart for that day is shown in Figure 1.9. Significant changes in the morphology of the ice cover occurred between this date and the previous sea ice option flight (see Figure 1.8). The entire pack shifted to the NW, and new grey ice areas appeared to the NW of Nunivak Island, off the west coast of Alaska (the largest one observed there during the Bering Sea Experiment), off western St. Lawrence Island and south of the Chukotsky Peninsula. By noting Figure 1.13 and Table 1.1, we see that the drift motion during the 20-28 February period was generally towards the NW. On 28 February the zone of predominantly white ice and white and first-year ice had shifted NW from its earlier position and the zones of grey-white ice had been compressed or formed into predominantly white ice.

The flow aloft during this second Bering Sea Experiment period of anti-cyclonic weather was similar to that observed earlier but less intense. The low level superadiabatic lapse rates had a lower gradient and the inversion layer was thinner.

On 2 March the second and final period of Bering Sea Experiment cyclonic weather started when an intense cyclone, with a central surface pressure of

8

960 mb and a well-established frontal zone (see Figure 1.4), entered the southern sector of the test area and the Siberian high cell was displaced northward. This cyclone moved eastward and was replaced by another one of equal intensity which on 5 March was over the Aleutians (see Figure 1.5). This was the day of the fourth and final sea ice option flight.

The ice distribution chart for these data is shown in Figure 1.10. As in the earlier comparison between the ice distribution charts of 20 and 28 February, significant changes occur between 28 February and 5 March. During this period the entire pack moved toward the SW. The ice drift vectors of the USCGC Staten Island (see Figure 1.13) during this period show that the ice in the test area was also advected to the SW. The zones of predominantly white ice and white and first-year ice have clearly shifted to the SW, as can be seen by noting the long shadow effect formed SW of St. Matthew Island as ice from both of these zones was advected around it. Large grey ice and grey and white ice zones appeared SW of the Chukotsky and Seward Peninsulas, in Norton Sound, and off the SW coast of Alaska. The ice distribution pattern for 5 March resembles that of 20 February, and both were formed by the pack being advected to the SW by NE winds.

The timing of the four sea ice options in relation to variations in the meteorological regime over the test area during the Bering Sea Experiment was indeed fortuitous. As we have seen, the test area synoptic situation started with strong anticyclonic activity, then became strongly cyclonic, then became weakly anticyclonic, and finally became weakly cyclonic. Comparing the ice distributions of the first and second sea ice option flights (15 and 20 February), we see how strong anticyclonic activity has stretched the pack and advected it to the SW. Comparing

9

these for the second and third sea ice options (20 and 28 February) we see how strong cyclonic activity has compressed the pack and advected it toward the NW. And finally, by comparing those of the third and fourth sea ice options (28 February and 5 March) we see how a short period of weak anticyclonic activity followed by a short period of weak cyclonic activity, during both of which the surface winds were generally from the NE, has advected the pack toward the SW while it once again underwent a stretching deformation.

1.3 SHIP TRACK, WEATHER, AND DRIFT

Of fundamental importance to the Bering Sea Experiment was the need to acquire ice and weather data deep within the Bering Sea ice cover between and during the remote sensing overflights. As can be seen in this and the following papers, the men of the USCGC Staten Island succeeded admirably in obtaining these data.

The entire track of the USCGC Staten Island during the Bering Sea Experiment is shown in Figure 1.11. Tracks of both powered and drifting trajectories of the ship are shown in this illustration. The complex track results from the demands dictated by the varying remote sensing flight options which were in turn dictated by the meteorological and surface conditions.

Surface and upper air weather data were obtained with two balloon ascents daily and surface observations taken every three hours. An interesting summary of the ship's weather is shown in Figure 1.12, in which average air temperature, wind speed, and wind direction are given for the period 14 February to 10 March 1973.

The bimodal character of the surface circulation and weather alluded to earlier can best be seen by comparing the curves for air temperature and wind

10

direction. During the strong anticyclonic period of 15-20 February the wind direction was from the N and air temperatures were low. The abrupt change into the strong cyclonic period of 21-27 February can be seen when the winds shifted from the SE and warm air was advected over the test area. The following weak anticyclonic period of 28 February to 1 March can be seen as the winds shift to N. During the period of weak cyclonic weather, 2 to 10 March, the final days of the Bering Sea Experiment, the NE winds continued and the air temperature gradually cooled as cold continental air was advected in from Alaska. Thus the ship curves of air temperature and wind direction correlate well and fit nicely the synoptic sequence based on surface weather charts (discussed earlier).

The night-time drifts of the ship in the pack ice allows us to compare ice drift with wind for short periods throughout the Bering Sea Experiment. In Figure 1.13 and Table 1.1 are shown the vectors for drift and wind averaged over the period of each drift. We would not expect the drift-wind correlation to match the theoretical predictions given by the steady-state models of Shuleikin (1938) or Reed and Campbell (1960, 1962) which consider ice moving under the action of air stress, water drag, and the Coriolis force, since it would take approximately two hours for steady-state ice motion to be established following a change in the surface wind stress and frequent short-time changes in magnitude and direction of the wind occurred. Nevertheless, during the majority of drifts the drift vector is to the right of the wind vector by 20° to 40°, which is what the theories predict. The correlations between wind speed and drift speed agree fairly well with the Reed-Campbell theory which predicts that for an average ice surface aerodynamic roughness of 0.02 cm the ratio of wind speed

to drift speed should be about 0.03. About half of the drifts give ratios reasonably close to this prediction. These correlations can be considered fairly good since we have no way of accurately estimating the effect of surface gradient currents (sea surface tilt) and internal ice stresses, the latter force probably becoming important when the pack is compressed when being advected northward.

1.4 MESOSCALE TEST AREA ICE DYNAMICS

The four Bering Sea Experiment sea ice option flights have given us the best existing sequential data on mesoscale ice morphology and dynamics for first-year and younger sea ice. By a fortuitous series of circumstances, it happened that the four selected sea ice option test areas were in approximately the same position, as can be seen in Figure 3.1. Indeed, all four selected test areas overlap. It must be borne in mind that this does not mean that the same area of sea ice was viewed each time, since the ice was being advected through each area with the continuous shifting of the ice pack. In the following discussion, the advective mode of the ice prior to each mesoscale test area observation will be given.

The detailed description of the type of ice within each test area during each sea ice option flight and its metamorphosis will be covered in Papers 2 and 3. This section of this paper will discuss the ice dynamics of each test area prior to and at the time of each observation and the way it relates to the macroscale situation.

As we saw earlier, the anticyclonic circulation over the experiment area for several days prior to and following the first sea ice option flight of 15 February had advected the pack to the south and put it into a stretching deformational

mode with a preferred lead and polynya orientation of ESE-WNW. Although we do not have a ship drift for 15 February, we can infer the advection of ice through the test area by noting the drift for 16 February. At this time the ice was moving at 4 km/hr to the S, and, since the wind direction and speed during this observation were approximately equal to that of the 15th, we can assume that the ice advection during the first sea ice option was the same.

The photomosaic (Figure 3.11) and 1.55 cm microwave mosaic (Figure 3.10) of the test area on this day show a preferred lead orientation of E-W with a polynya array in the western edge running N-S. The percentage of open water in the microwave mosaic is estimated as 26% from the histogram analysis (Figure 3.14), thus the ice at this time had undergone strong divergence.

The anticyclonic circulation over the experiment area continued until the second sea ice option on 20 February. The ship drifted S during the night of 19/20 February at a speed of 1.5 km/hr. The entire ice pack was advected S during the 15-20 February period (see Figures 1.7 and 1.8) and continued to undergo stretching deformation. The lead and polynya array was more complex on 20 February than on the 15th, with two sets of roughly orthogonal orientations running E-W and N-S. The 1.55 cm microwave mosaic for 20 February (see Figure 3.10) shows a strong N-S orientation in the center of the test area with an E-W one in the eastern part. The amount of open water estimated from the histogram analysis (Figure 3.14) is 16%, thus the ice continued to undergo strong divergence during this period.

The test area for 20 February was approximately 55 km SW of the one for 15 February (see Figure 3.1). The integrated night-time ship drift for the period 16-20 February indicates that the ice within the 15 February test area moved

13

south with a mean speed of approximately 1.6 km/hr. If we assume that this speed also applies to the daytime ice drift, then essentially none of the ice viewed in the test area of 15 February was within the test area of 20 February. If we assume that the average drift speed was less than 1.6 km/hr, then some of the ice in the northern section of the test area on 15 February may have been in the southern section of the test area on 20 February.

For a week prior to the 28 February sea ice option, strong cyclonic activity advected the ice cover of the Bering Sea towards the NW (see Figures 1.8 and 1.9). The ship drifts during the period 20-28 February show that the average ice drift was about 1.2 km/hr to the WNW, therefore we can conclude that all of the ice observed in the test area during the prior mission on 20 February had been advected out of the test area of 28 February.

On 28 February the synoptic regime abruptly changed and a few hours prior to the time of observation of the test area the ice pack had started to move S at a speed of 2.1 km/hr (Figure 1.13, Table 1.1).

The photomosaic (Figure 3.13) and microwave mosaic (Figure 3.12) of the test area for this day show an irregular lead and polynya array, and the aircraft observations of the ice in the experiment area show that this was the case over all of the eastern Bering Sea ice pack. The amount of open water in the test area estimated from the histogram analysis (Figure 3.14) for this time is 10%. Since the ice pack started to move S a few hours before the time of observation, this slight divergence may have only recently occurred. At any rate, this was the least amount of open water observed in any test area during the Bering Sea Experiment.

During the period between the third and last ice option, weak cyclonic activity advected the ice cover of the experiment area to the SW (see Figures 1.9 and 1.10). The ship drift data give an average ice drift during this period of 1.6 km/hr to the SW, therefore we may assume that all of the ice observed in the test area on 28 February had been advected out of it by 5 March.

The photomosaic (Figure 2.18) and microwave mosaic (Figure 2.19) of the test area for this day show a rough E-W lead orientation and a band of polynyas running NE-SW. The histogram analysis (Figure 3.14) indicates that 18% of the test area was open water. Therefore, the ice in the test area on 28 February underwent recent divergence as it was advected south.

Viewed in sequence, these data show that when the ice pack is advected in a southerly direction it undergoes strong divergence and a stretching mode of deformation. The lead and polynya patterns are more regular in this mode than when the ice is advected northward by strong cyclonic activity and undergoes convergence.

ACKNOWLEDGMENT

BIBLIOGRAPHY

Reed, R. J. and W. C. Campbell, "Theory and observations of the drift of Ice Station Alpha," Final Report, Task Number N.R. 307-250, University of Washington, 255 pp. (1960).

Reed, R. J., and W. C. Campbell, "The equilibrium drift of Ice Station Alpha," J. Geophy. Res., 67, 281-297 (1962).

Shuleikin, V. V., "The drift of ice-fields," Comptes Rendus (Doklady) de l'Acad. des Sci. de l'USSR, 19, 589-594 (1938).

Table 1.1

Ship Drift and Wind Vectors During Besex

DATE	LATITUDE	LONGITUDE	SHIP DRIFT	SHIP DIRECTION	WIND SPEED	WIND DIRECTION	DURATION
FEB	N	W	$km.h^{-1}$		$km.h^{-1}$		h
16	61° 39'	176° 08'	4.0?	185	20.3	170	4.7
17/18	63° 00'	175° 19'	0.3	145	14.8	170	13.3
18/19	62° 54'	173° 51'	0.8	90	27.7	160	13.4
19/20	62° 48'	173° 51'	1.5	180	37.0	180	18.2
21/22	61° 21'	174° 06'	1.7	350	31.4	280	13.5
22/23	61° 07'	174° 09.5'	1.2	335	29.6	290	11
23	61° 21'	174° 45.8'	0.06	–	1.3	270	6.5
24	61° 00'	173° 00'	0.2	295	29.6	280	17
25	60° 30'	174° 00'	1.05	290	16.6	300	6
25/26	60° 36.8'	174° 13'	0.9	280	25.9	300	10.25
26/27	61° 11.5'	174° 35'	0.07	225	11.1	260	7.8
27/28	62° 16.1'	176° 21.5'	2.3	225	16.6	190	14.4
28	61° 38'	175° 19'	2.1	150	18.5	170	4.2
MAR							
1/2	63° 04.1'	173° 58.5'	1.3	210	24.05	240	13
2/3	63° 05.2'	173° 52'	1.2	200	44.4	240	13.4
3/4	63° 04.8'	174° 21'	2.0	270	38.8	230	8.9
4	62° 30.3'	174° 59.6'	1.1	230	31.4	220	14.45
5/6	61° 32.1'	177° 03.5'	0.9	260	25.9	220	13.25
6	61° 29.8'	177° 18'	1.8	260	27.7	210	2

SURFACE WEATHER CONDITIONS

BERING SEA EXPERIMENT

16 FEBRUARY 1973
0000 GMT

17 FEBRUARY 1973
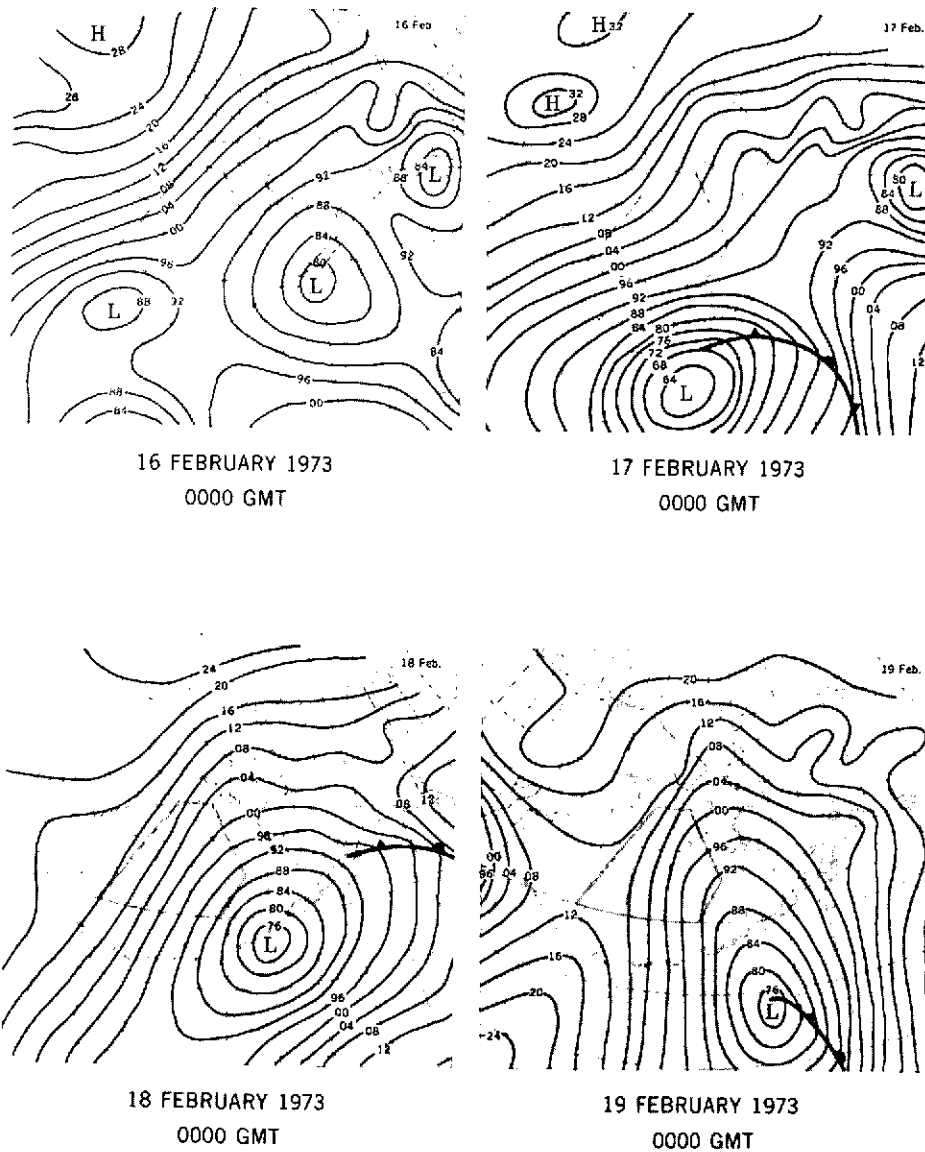0000 GMT

18 FEBRUARY 1973
0000 GMT

19 FEBRUARY 1973
0000 GMT

Figure 1.1.   Surface Weather Conditions, 16, 17, 18, and 19 February 1973

SURFACE WEATHER CONDITIONS
BERING SEA EXPERIMENT

20 FEBRUARY 1973
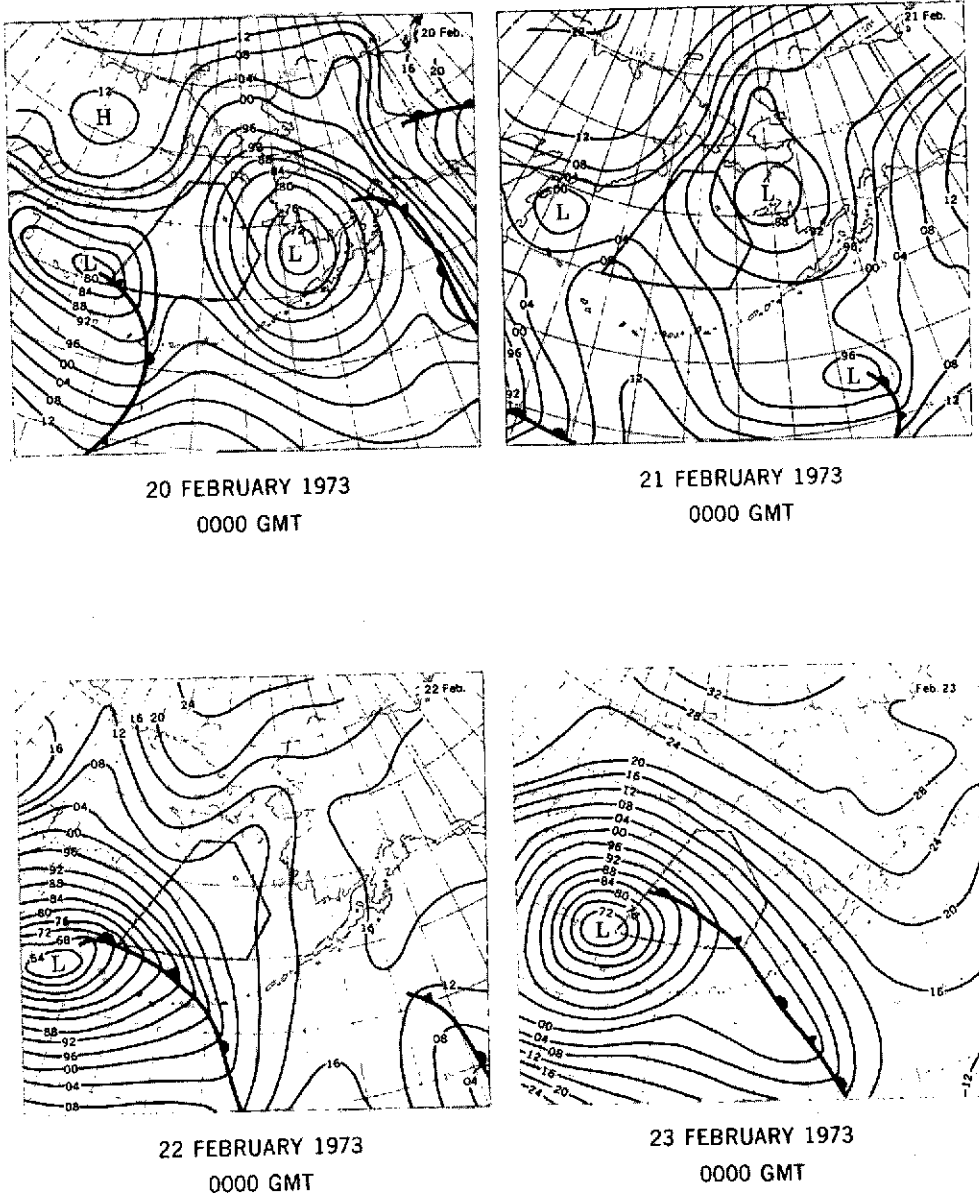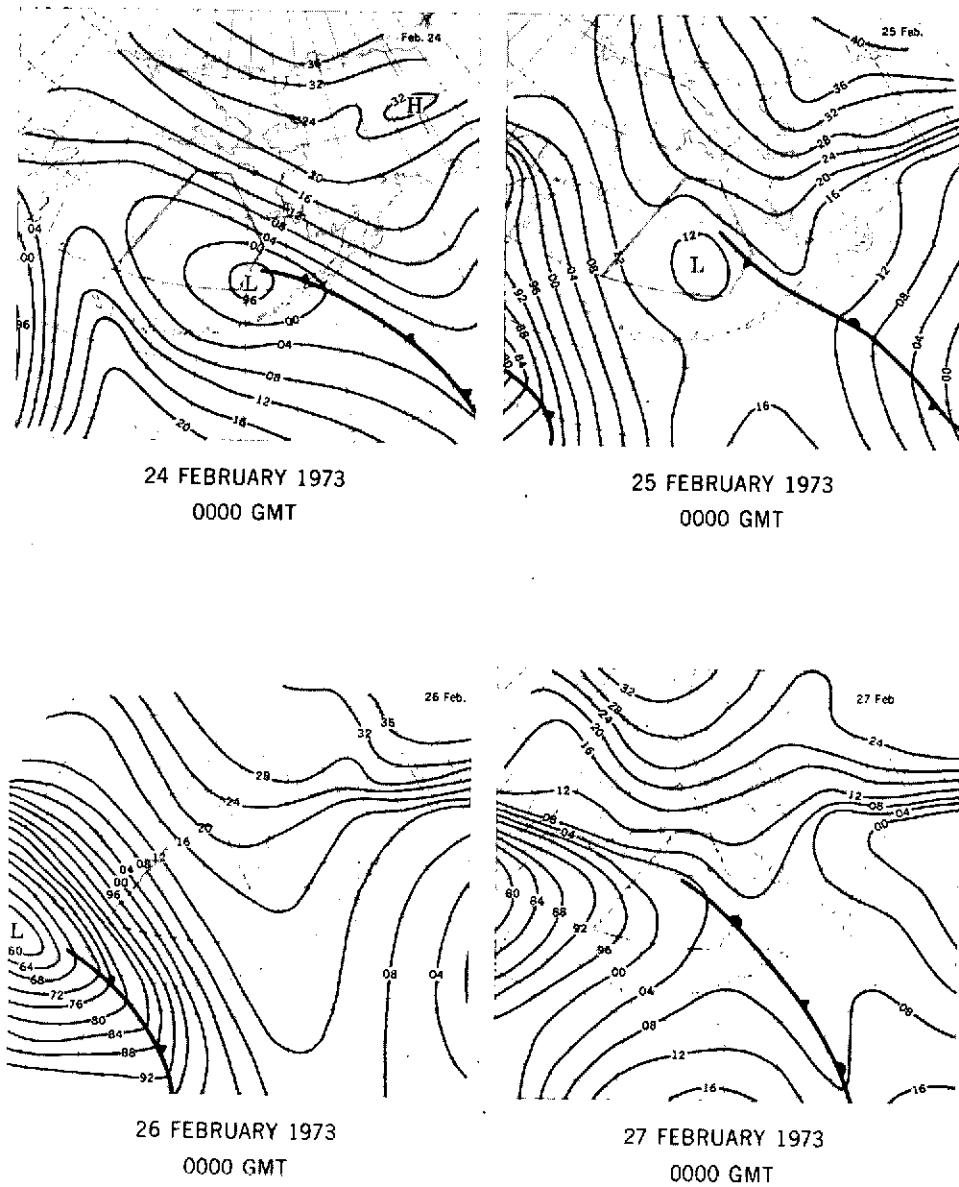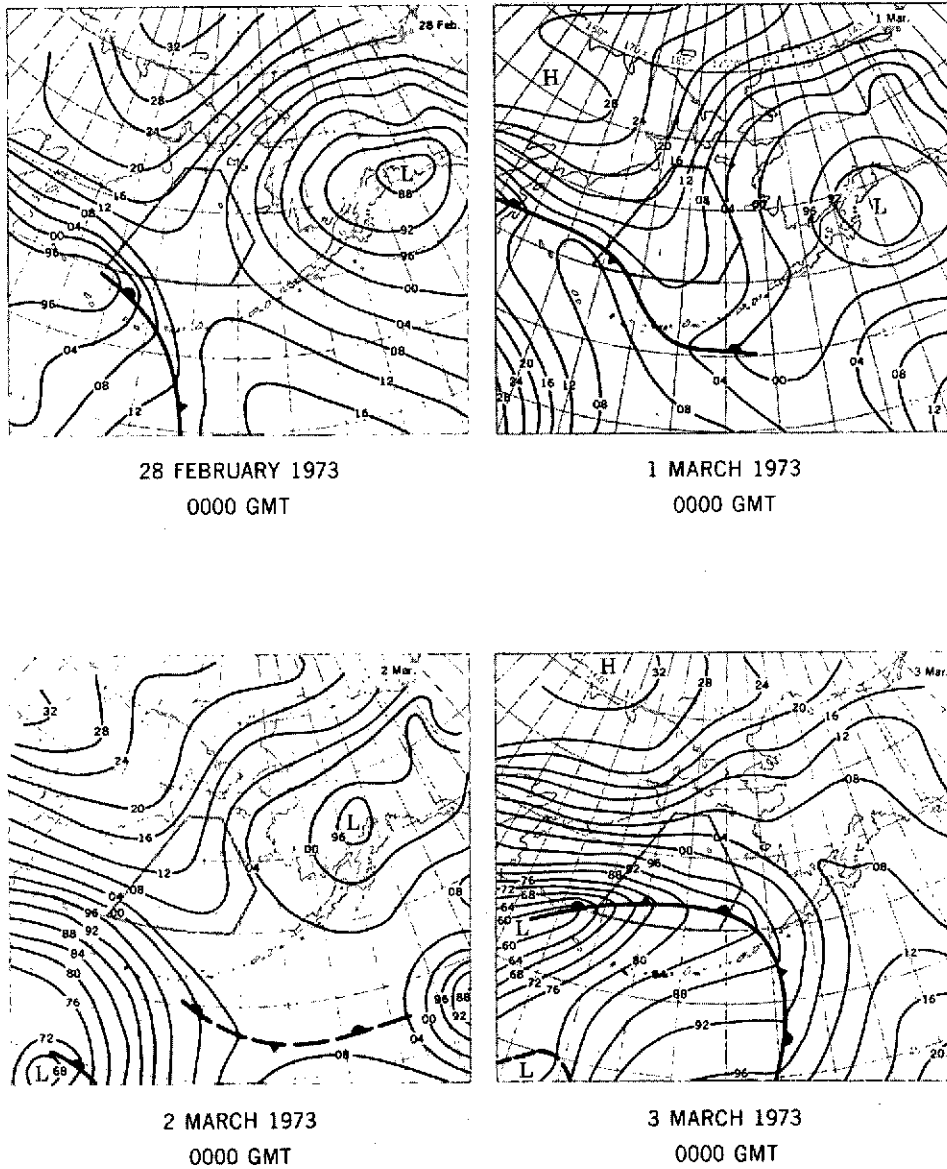0000 GMT

21 FEBRUARY 1973
0000 GMT

22 FEBRUARY 1973
0000 GMT

23 FEBRUARY 1973
0000 GMT

Figure 1.2. Surface Weather Conditions, 20, 21, 22, and 23 February 1973
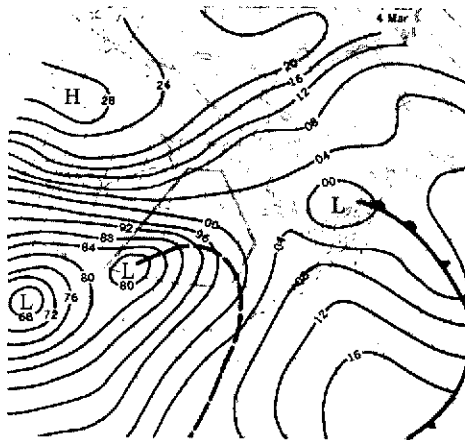
SURFACE WEATHER CONDITIONS

BERING SEA EXPERIMENT

24 FEBRUARY 1973
0000 GMT

25 FEBRUARY 1973
0000 GMT

26 FEBRUARY 1973
0000 GMT

27 FEBRUARY 1973
0000 GMT

Figure 1.3. Surface Weather Conditions, 24, 25, 26, and 27 February 1973
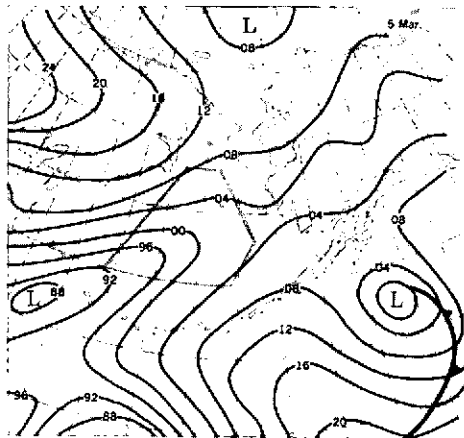
SURFACE WEATHER CONDITIONS
BERING SEA EXPERIMENT

28 FEBRUARY 1973
0000 GMT

1 MARCH 1973
0000 GMT

2 MARCH 1973
0000 GMT

3 MARCH 1973
0000 GMT

Figure 1.4. Surface Weather Conditions, 28 February and
1, 2, and 3 March 1973
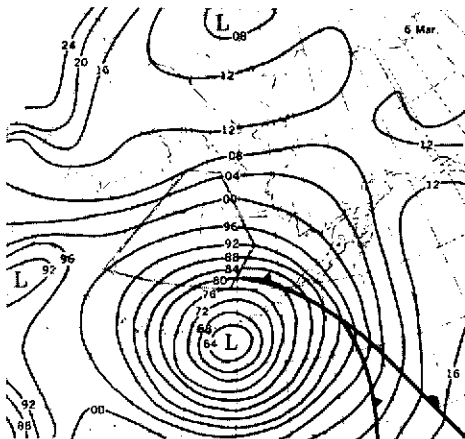
SURFACE WEATHER CONDITIONS
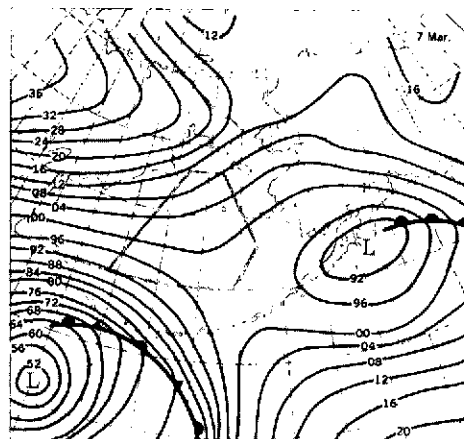## BERING SEA EXPERIMENT

4 MARCH 1973
0000 GMT

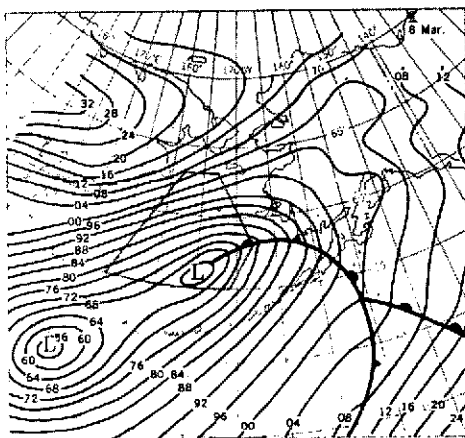5 MARCH 1973
0000 GMT

6 MARCH 1973
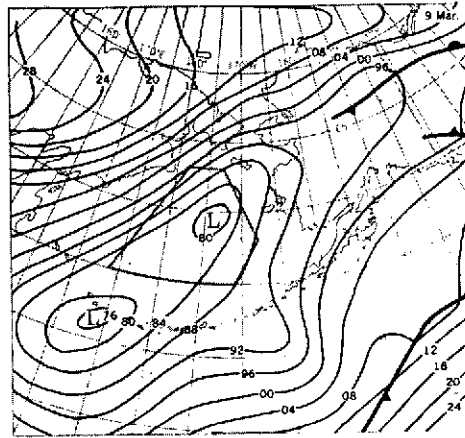0000 GMT

7 MARCH 1973
0000 GMT

Figure 1.5. Surface Weather Conditions, 4, 5, 6, and 7 March 1973
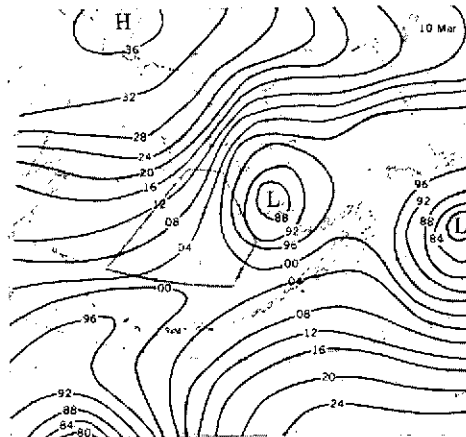
SURFACE WEATHER CONDITIONS
BERING SEA EXPERIMENT

8 MARCH 1973
0000 GMT

9 MARCH 1973
0000 GMT

10 MARCH 1973
0000 GMT

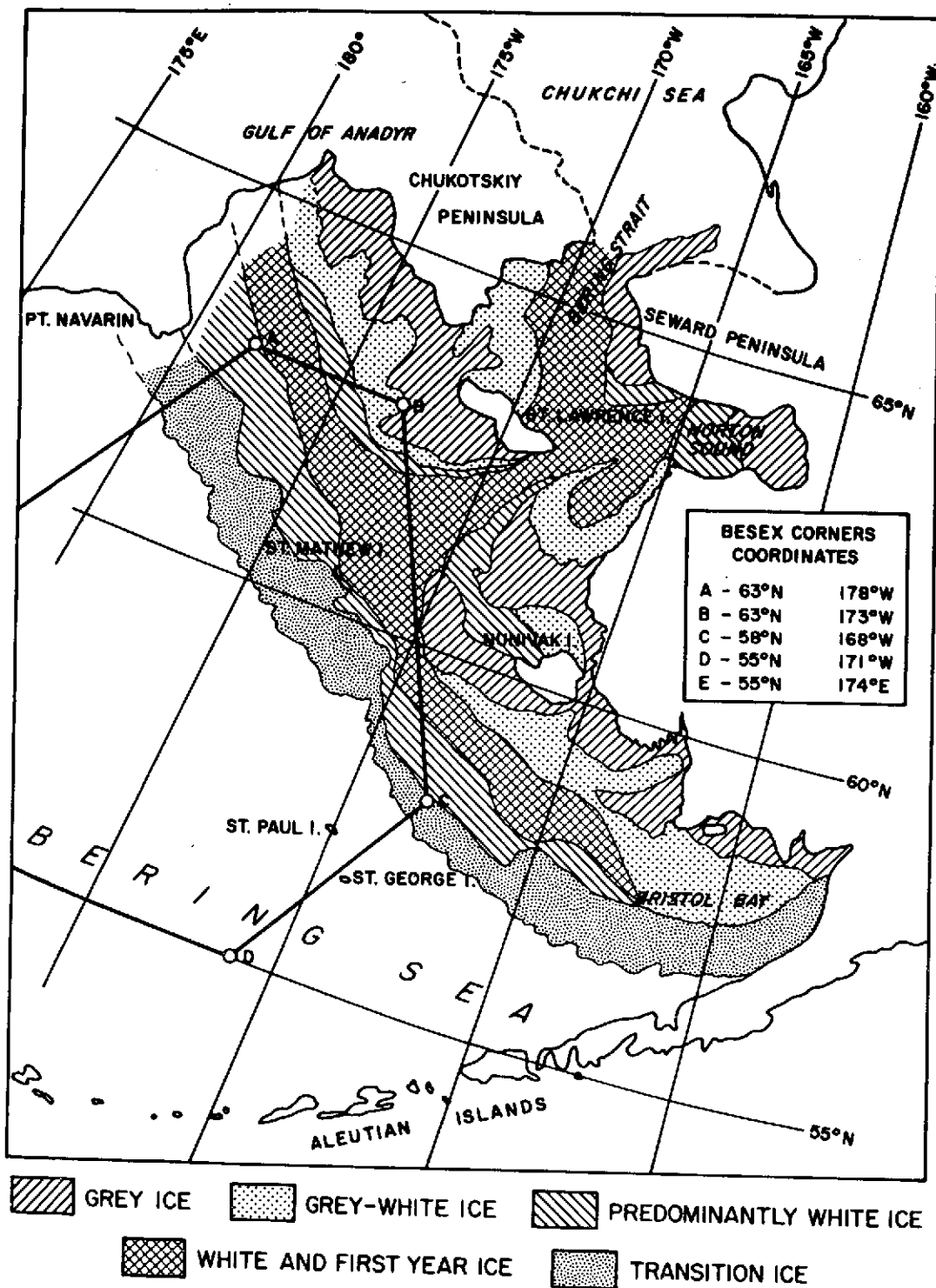Figure 1.6. Surface Weather Conditions, 8, 9, and 10 March 1973

23

GREY ICE   **GREY-WHITE ICE**   **PREDOMINANTLY WHITE ICE**

WHITE AND FIRST YEAR ICE   **TRANSITION ICE**

Figure 1.7. Sea Ice Distribution, 15 February 1973

BESEX CORNERS COORDINATES

A	63°N	178°W
B	63°N	173°W
C	58°N	168°W
D	55°N	171°W
E	55°N	174°E

GREY ICE   GREY–WHITE ICE   PREDOMINANTLY WHITE ICE

WHITE AND FIRST YEAR ICE   TRANSITION ICE
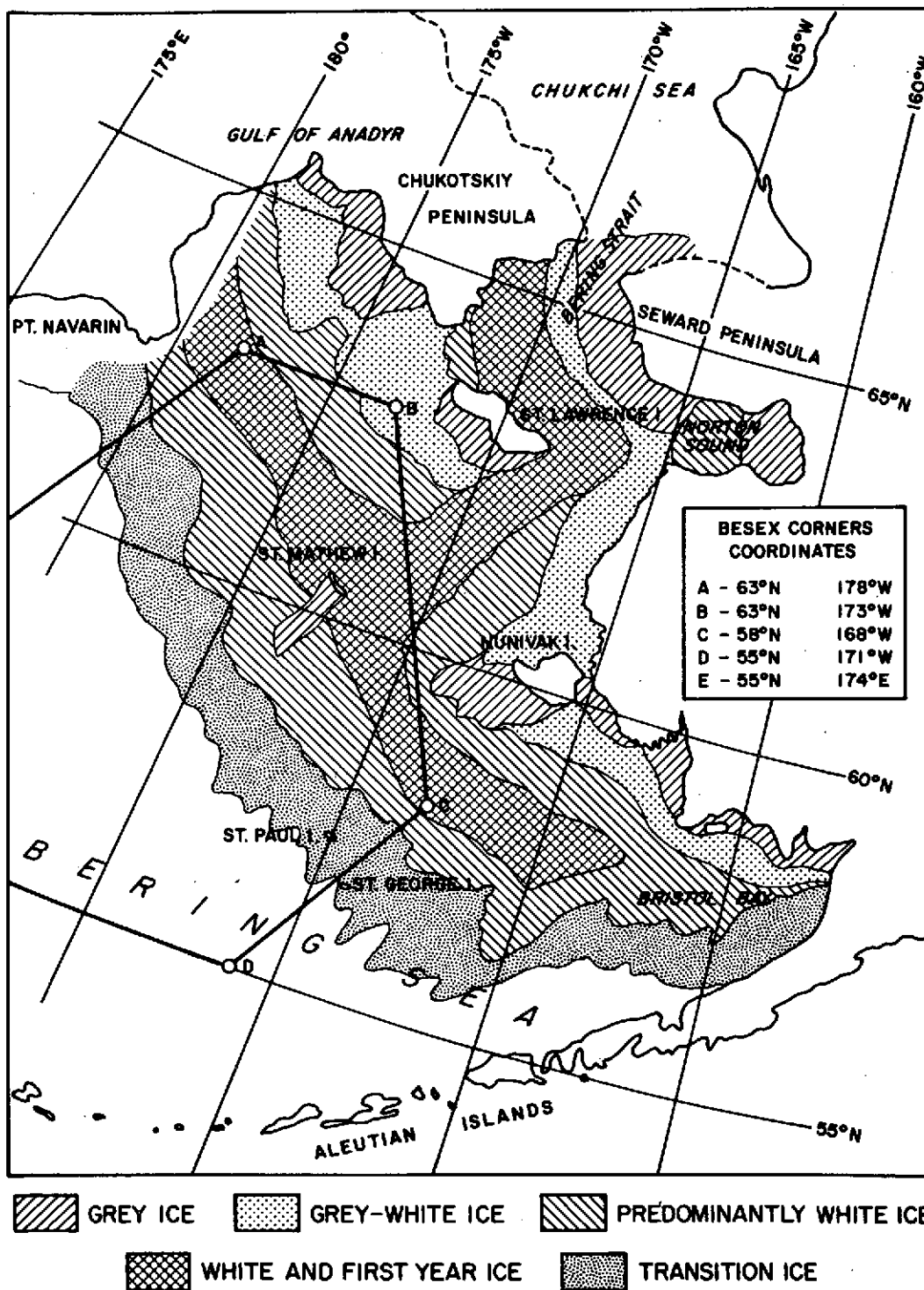
Figure 1.8. Sea Ice Distribution, 20 February 1973

BESEX CORNERS COORDINATES

A – 63°N		178°W
B – 63°N		173°W
C – 58°N		168°W
D – 55°N		171°W
E – 55°N		174°E

GREY ICE GREY-WHITE ICE PREDOMINANTLY WHITE ICE

WHITE AND FIRST YEAR ICE TRANSITION ICE
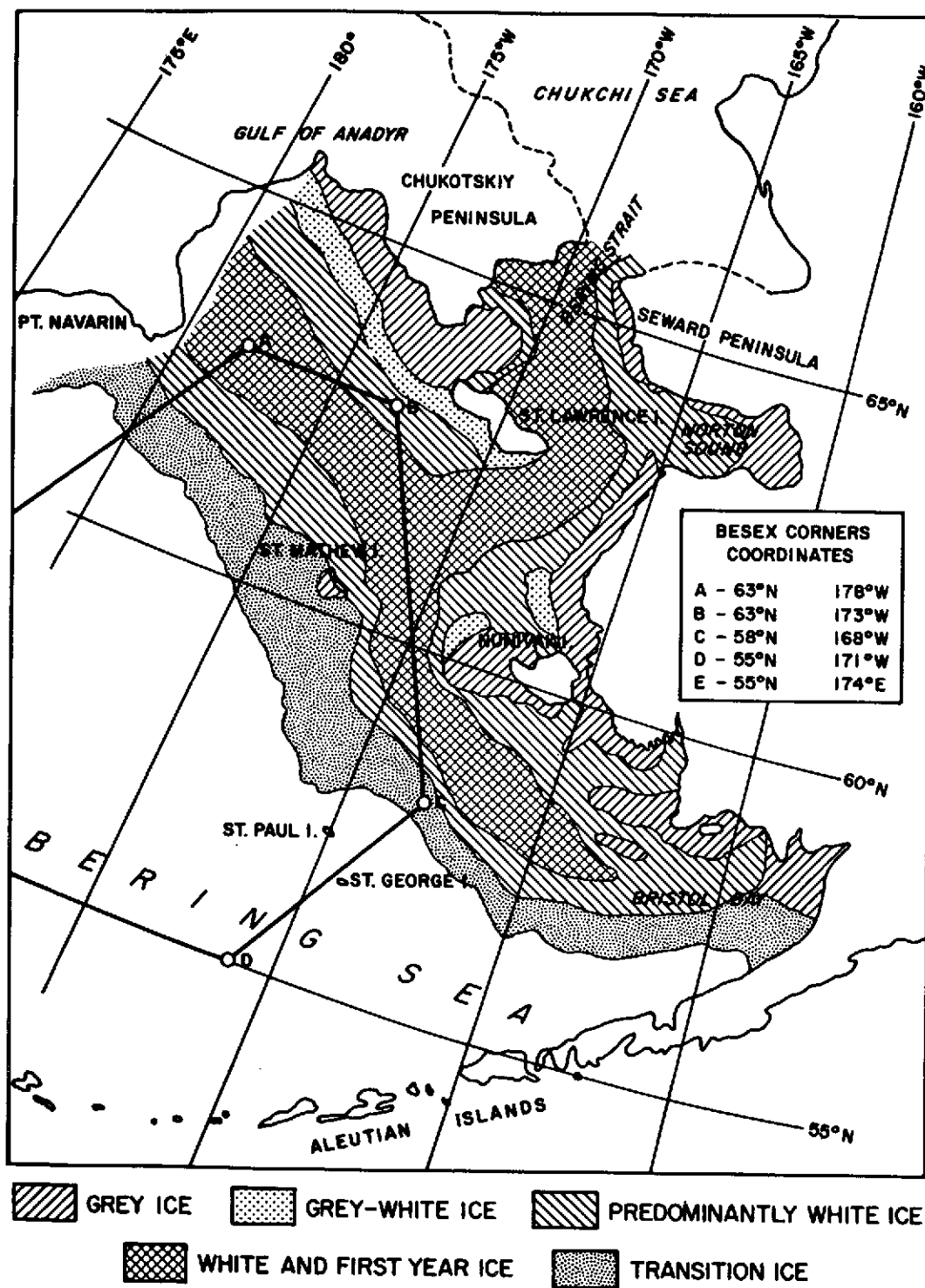
Figure 1.9. Sea Ice Distribution, 28 February 1973

BESEX CORNERS
COORDINATES

A – 63°N	178°W
B – 63°N	173°W
C – 58°N	168°W
D – 55°N	171°W
E – 55°N	174°E

GREY ICE   GREY-WHITE ICE   PREDOMINANTLY WHITE ICE

WHITE AND FIRST YEAR ICE   TRANSITION ICE
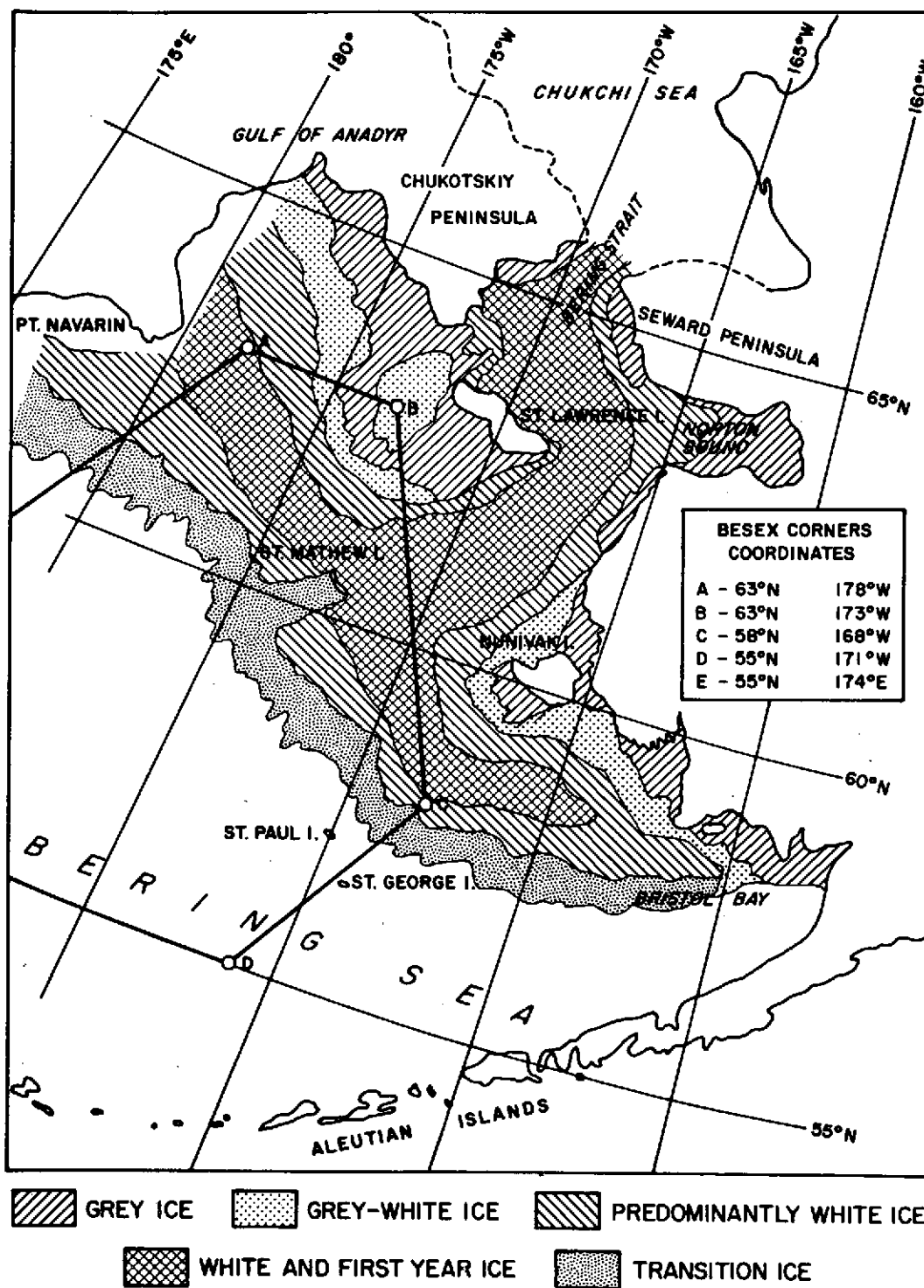
Figure 1.10.   Sea Ice Distribution, 5 March 1973

27

Figure 1.11. Positions of the USCGC Staten Island During the Bering Sea Experiment

AIR TEMPERATURE, WIND DIRECTION AND SPEED OBSERVED FROM USCGC STATEN ISLAND DURING THE BERING SEA EXPERIMENT
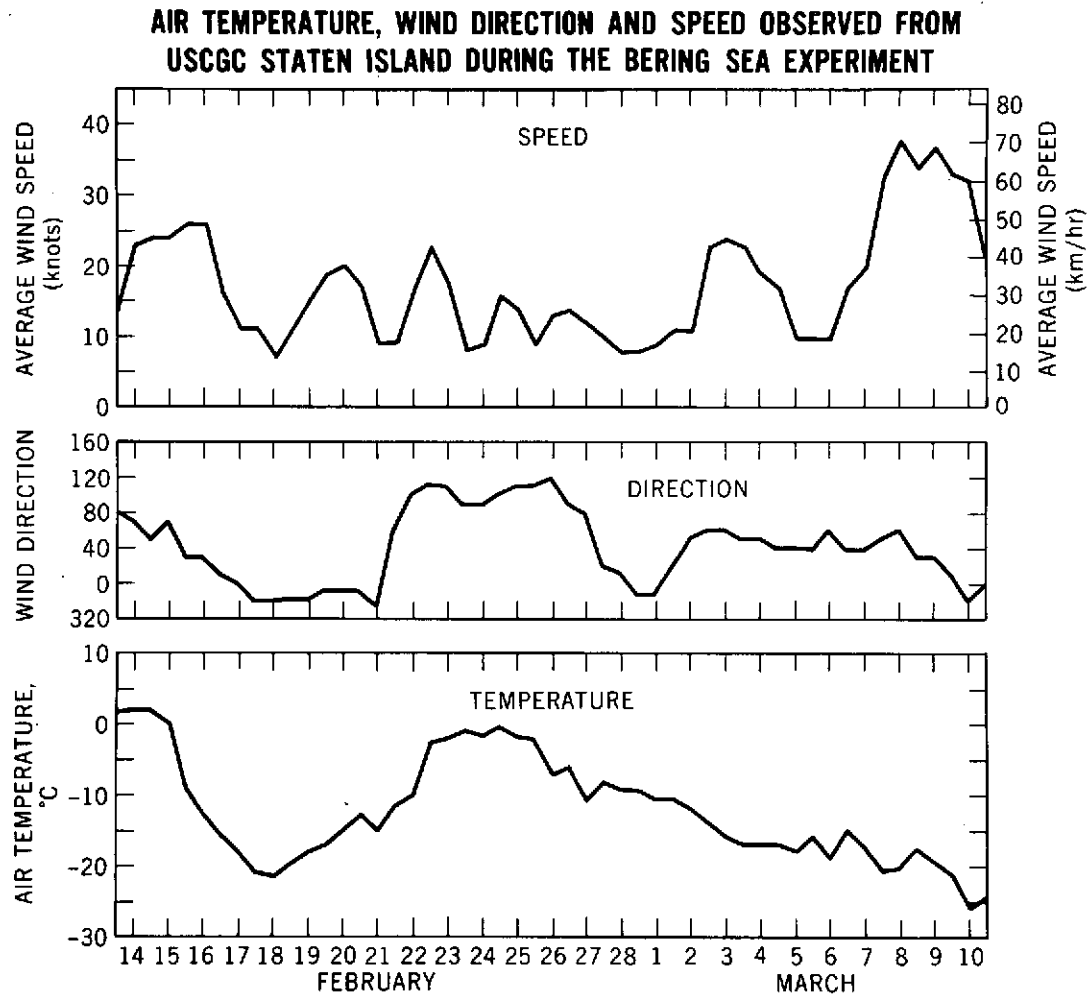
Figure 1.12. Wind Speed, Wind Direction, and Temperature from the Records Taken on the USCGC Staten Island
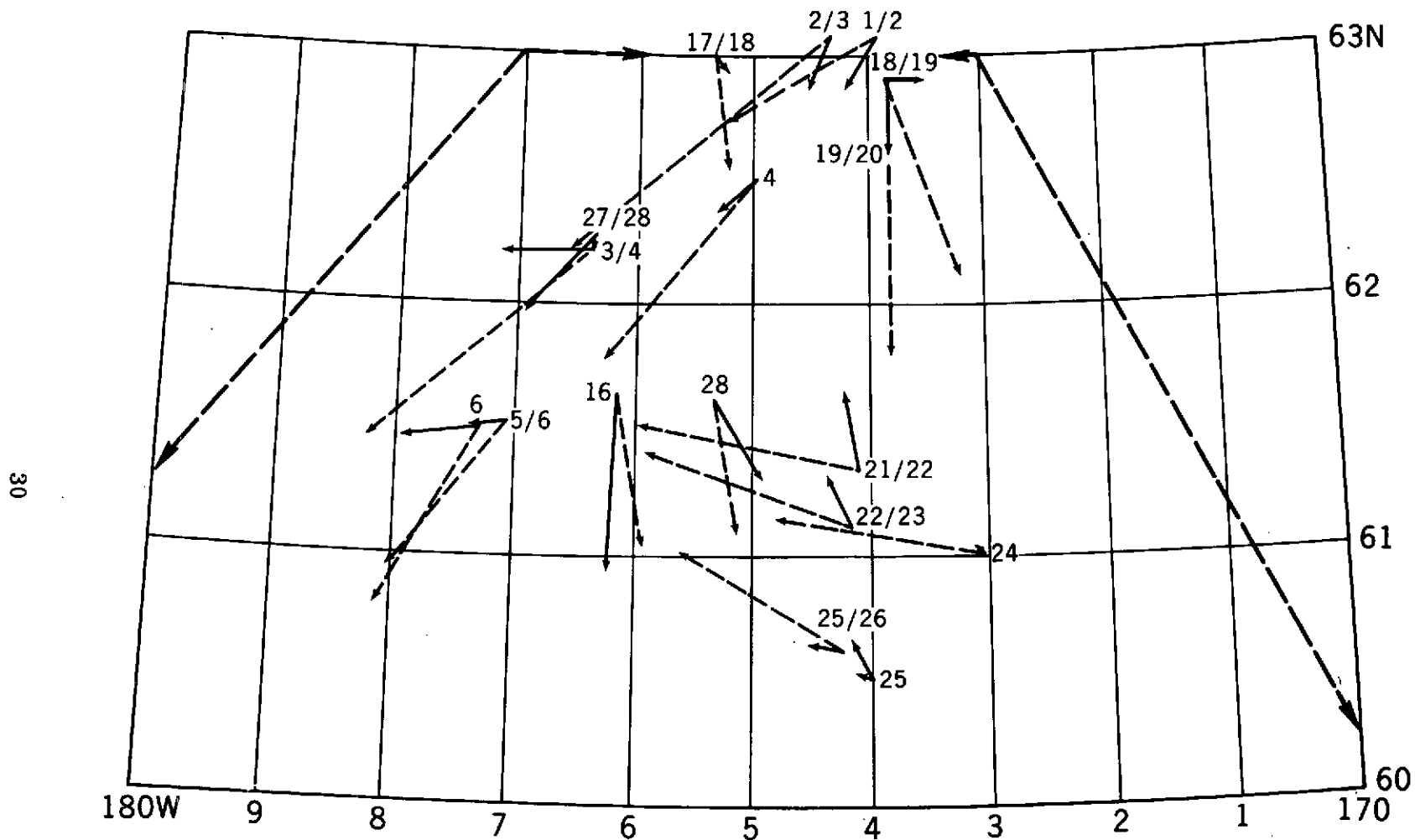
Figure 1.13. USCGC Staten Island drift vectors and wind vectors during the Bering Sea Experiment. The wind vectors are the broken lines; the ship drift vectors are the solid lines. The ratio between the wind and drift vectors is 6:1.

PAPER NO. 2

MESOSCALE DESCRIPTION FOR THE PRINCIPAL

BERING SEA ICE EXPERIMENT

R. O. Ramseier*

P. Gloersen[†]

W. J. Campbell[‡]

T. C. Chang[**]

*Department of the Environment, 562 Booth Street, Ottawa, Ontario,
K1A OE7, CANADA

[†]National Aeronautics and Space Administration, Goddard Space Flight
Center, Greenbelt, Maryland

[‡]U. S. Geological Survey, Ice Dynamics Project, Tacoma, Washington

[**]NAS – NRC Resident Research Associate

MESOSCALE DESCRIPTION FOR THE PRINCIPAL
BERING SEA ICE EXPERIMENT

R. O. Ramseier

P. Gloersen

W. J. Campbell

T. C. Chang

ABSTRACT

In this paper, the experimental data acquired on the occasion of the principal sea ice experiment in the Bering Sea on 5 March 1973 are described and analyzed. Sea ice properties (salinity, density, and temperature profiles) acquired by measurements on the surface along the three diagonals of the U.S.A., Overlap, and U.S.S.R. experiment areas on that date are tabulated, along with photographic records of the various test sites. Some select sea ice samples were returned to the home laboratory for more detailed study, including microphotography and the measurement of the complex dielectric constant, which are also described. A conclusion from these studies is that the upper frazil ice layer is largely responsible for the microwave signatures at all the wavelengths studied. In surveying the microwave data obtained on board the CV-990 aircraft, it was found that no multiyear ice was evident in the test area. However, a new ice signature, similar to that of multiyear ice, was found to occur over grey ice on which the existence of a film of moisture was discovered during the surface measurements.

The moisture film is attributed to a high salt concentration at the surface of the ice, and hence a lowering of the melting point, as a result of sublimation of the ice from the surface. Analysis of the 1.55 cm radiometer data resulted in a determination of an 82% ice concentration in the U.S.A. test area on 5 March 1973.

MESOSCALE DESCRIPTION FOR THE PRINCIPAL
BERING SEA ICE EXPERIMENT

1. INTRODUCTION

In this paper a detailed study of the surface truth data obtained with the assistance of the USCGC icebreaker Staten Island on 5 March is presented, preceeded by a section on the general experimental procedures. This is followed by a general discussion of ice morphology and specific passive microwave signatures.

The atmospheric and overall ice conditions have been discussed in Paper No. 1. The ice in the test area on 5-6 March moved in a westerly direction in the order of 0.9 km h^{-1}. The wind speed averaged 25.6 km h^{-1}. The direction was SW. The ice drift vector as measured by the drift of the ship was to the right of the wind vector. This agrees well with expectations based on the Coriolis forces applied to the ice. The ice drift was somewhat higher than observed on earlier occasions (Zubov, 1947; Reed & Campbell, 1962) in the Arctic Ocean. The air temperatures averaged –18°C during this two-day period.

2. SURFACE-BASED MEASUREMENTS

The stations occupied during the two-day period are shown in Figure 2.1. The two boxes enclosing the stations indicate the areas overflown by the USSR and USA aircraft. The stations A5 to A1 in the USA test area were occupied in the time period 2100 to 2345 GMT on 5 March. (All times are GMT.) The stations I4 to I1 which were located in the overlap area were occupied between 0030 and 0145 on 6 March. Finally, the stations R1 to R5, located in the USSR test area, were occupied between 2100 and 2300 on 6 March. The USA CV 990 aircraft

overflew its test area between 2216 and 2342 on 5 March, coinciding with the surface measurements. The USSR IL 18 aircraft overflew its test area between 2229 on 5 March and 0200 on 6 March. The USSR AN 24 aircraft with its side-looking radar overflew the test area between 0057 and 0241 on 6 March. Therefore, the A and I stations were occupied during the overflight of all three aircraft. Unfortunately, the R surface stations were occupied about 20 hours after the USSR aircraft had terminated their measurements. This delay in station measurement was caused by a fuel leak in the pilot compartment of the helicopters, which had to be repaired before the resumption of further measurements. Based on ship drift, it was calculated that the ice moved a maximum of 18 km in a westerly direction. Therefore the surface stations were still within the USSR test area as in Figure 1.

2.1 EXPERIMENTAL METHODOLOGY

The whole surface measurement program was staged from the USCGC ice breaker Staten Island which steamed a total of 2035 km during the Bering Sea Experiment. Most of the measurements were made with the aid of the two on-board helicopters. They provided the backbone of the whole operation, logging a total of 3885 km. Prior to each day's mission, a conference between the senior scientist onboard and the NASA scientists at Anchorage took place via a satellite relay. At this time, the preceding day's activity and ice conditions were discussed. The following day's plan was then formulated. If a sea ice option was contemplated, confirmation of the proposed coordinates was obtained from the USSR scientific team stationed at Cape Schmidt. Following the communications with Anchorage, an informal shipboard planning conference was held between the

senior scientist, the executive officer, operations officer, and aviation officer, at which the details of the next day's mission were worked out.

Once the helicopters were underway the positioning usually was accomplished with the help of the ship radar and radio beacon. On a few occasions, the helicopters were out of ship's range, and the helicopters' own instrumentations were used for bearings. Once the prearranged station area was reached the senior scientist would select a representative ice condition typical of the area. The low-flying helicopter would then be directed by the high-flying helicopter to the selected spot. A high-level photograph, preferably with the low flying helicopter in the field of view, would then be taken for documentation of the sites that were sampled.

The aerial photograph was usually taken out of the side window of the helicopter from an altitude of 300 m if the weather was good, as was the case for the A and I stations (Figure 2.2). The R stations were photographed from an altitude of 100 m due to poorer visibility. The low flying helicopter would then land and disembark a seaman and crew member. It would then take off again and land at a convenient location to await the landing of the high level helicopter with the senior scientist and his equipment. Once the measurements were taken the helicopters would take off in reverse order. Depending on the ice conditions this procedure varied to some extent, especially if the floes were free-floating.

At each station two cores were collected. A continuous 0.075 m diameter core was used for the in situ temperature and salinity measurements. The 0.20 m diameter surface core was used for structure, texture, density and in some cases dielectric properties determinations. The temperature measurements were made as soon as the core or core pieces were extracted from the

ice cover or floe. The core was then labelled and placed in a plastic sleeve and stored in an insulated box in one of the helicopters to be transported back to the Staten Island. The 0.20 m diameter surface core, which was about 0.30 m thick, was put in a plastic bag and also stored. Besides taking the core temperatures, the amount of snow, the total ice thickness, and the freeboard were measured. In some cases, the snow density was also obtained.

After repeating this procedure for 4 to 5 stations, the helicopters returned to the ship. The cores were transferred into another insulated box. Upon arrival, the salinity cores were immediately processed. A marine science technician and seaman would cut up the salinity cores into 0.025 m wafers on a band saw located on the fantail under the helicopter deck. The wafers were placed in plastic bags, the bags were sealed and stored in a warm place to melt. At some later time, the 0.20 m diameter cores would be processed. The density measurements could only be made during periods when the ship was at a complete stand-still in a calm sea. This usually took place at night. Normally two sorties were made each day during the entire Bering Sea Experiment.

The ice core temperatures were measured with a digital thermometer using a silicon semiconductor probe. A temperature reading could be obtained within a few seconds, avoiding any substantial core cooling or warming. The accuracy was ±0.05°C. The salinities of melted ice samples were measured with a two-electrode conductivity bridge. The bridge was calibrated in two ranges: 0-4 ppt and 0-40 ppt. The accuracy was ±0.1%. The densities were determined by using the hydrostatic method. A beam balance accurate to ±0.25 g was used for all density measurements.

The structural analysis was performed by cutting a 0.02 m thick vertical ice slab from the 0.20 m diameter core. This slab was then photographed for later analysis. A number of thick sections were shipped back to the laboratory at the Department of Environment for texture studies. In addition, dielectric properties were also measured in that laboratory using these selected thick sections. The ice samples were accurately machined and placed in the wave guide sample holder of the 3 cm wavelength CW microwave bridge (Vant, et al, 1974) used for these measurements.

2.2 GENERAL STATION ICE CONDITIONS

The aerial and surface photographs taken during the helicopter operations are shown in Figures 2.2 to 2.5. Under each photograph, the station number is indicated. If the photograph was taken from the surface, (in situ) has been added to the station number. The helicopter altitude varied between 260 and 490 m for stations A and I and from 90 to 150 m for the R stations. The low-level flying helicopter is always visible and can be used as a scale. The length of the helicopter body is about 11 m.

In discussing the ice conditions, we have grouped similar stations together into four groups. The first group, consisting of stations A5, A2, A1 and I2, consists primarily of white ice in the form of floes with an average size of 900 m^2. The ice has undergone a considerable amount of rafting as is evident by the rough surface. Snow-covered grey ice between the floes acted as a cement holding the floes together. The percentage of snow-covered grey ice amounted to less than 5%.

The second group, consisting of stations A4 and A3, represent predominantly grey ice areas. A considerable amount of rafting has taken place, but otherwise

38

the surface is often smooth. Various degrees of hoarfrost formed on the surface; usually the thinner the ice the smaller the amount of hoarfrost. The white ice floes visible at station A4 are on the average 400 m^2 in extent and show a greater percentage of grey ice between them.

The third group, representing stations I4, I3, and I1, contain a number of refrozen and open leads amongst white floes. The average floe size is 150 m^2 and the amount of grey ice is about 15%. The amount of open water is negligible. The larger floes visible in the bottom center of station I4 show a considerable amount of surface roughness which was caused by the consolidation of a number of floes.

The final group of stations with similar features are all the R stations located in the USSR test area. Because of poor visibility, the photographs were taken from an altitude of about 100 m. First of all the floe size is much smaller, having a size of 36 m^2 on the average. The amount of grey ice is about 30%, which is significantly more than the amount of grey ice observed in the first group of test stations in the US test area. The floe size is also smaller, being about one tenth the area of the first group. Not much open water was observed at the stations.

Generally, the ice had undergone extensive rafting everywhere. Also, generally, the white floes became smaller and more dispersed and the amount of grey ice surrounding the floes increased with proximity to the ice edge.

2.3 SURFACE PROPERTIES OF BERING SEA ICE

From measurements made on the microwave properties of first year ice during the Arctic Ice Dynamics Joint Experiment (AIDJEX) during March 1972,

in the Beaufort Sea, it was shown that the microwave emission essentially took place within a fraction of a wavelength of the surface (Meeks, et al, 1974). Accordingly, surface truth measurements for the Bering Sea Experiment were concentrated in the upper portion of the sea ice samples.

2.3.1 Structural and Textural Properties

The data for all the station measurements are presented in Figures 2.6 to 2.15. The number on the top left corner above each profile designates the station number and white ice. If the number is followed by a G, this indicates that the sample represents grey ice. The station position data and other relevant data are given in Table 2.1. The schematic of the core structure is shown on the left hand side of the depth profile data. The number on top of the core designates the amount of snow on top of the ice (cm), and the number at the bottom of the core gives the total ice thickness (cm). The thickness data have been summarized in Table 2.1 including the thickness of frazil ice. The small dashed lines on both sides of the core near the top, where present, indicate the water level and the amount of freeboard. The line which crosses the core at the end of the schematic ice characteristics representation indicates to what depth the structural and textural data were obtained.

The structural data indicated the existence of three distinct ice categories. These are, from top to bottom, frazil ice, a mixture of frazil and columnar ice, and columnar ice. An example is shown in Figure 2.16.

For all cases measured, the top layer of the ice is frazil ice. (In the ice observer language, this is known as grease ice when it forms.) Its thickness varies between 0.02 to <0.36 m, with an average thickness of 0.13 m. The second and most predominant category is columnar ice. In some cases, a mixture of

frazil and columnar ice is seen. This is very often associated with rafting of very thin ice.

A thin and thick section of a typical surface core are shown in Figure 2.16. The top portion of the sections consists of frazil ice; the bottom consists of columnar ice. The grain size varies from 0.001 to 0.002 m. The grains usually have equal axes but in some cases are slightly elongated. The crystallographic orientation is random. The visible bubble content is small. The dark spots in the thick section indicate brine pockets which have a random distribution and spherical appearance.

The columnar ice in the lower portion of the sample takes its characteristics from the frazil ice. It starts out with a small grain size and random orientation. The grain size increases with depth and the random crystallographic orientation gives way to a preferred horizontal orientation. The brine pockets which appear as dark lines in the thick section are elongated and form parallel to the growth direction.

Variations of this structure and texture have been observed for many cases. Banding which appears in some samples (not shown) can be associated with rafting. Based on the thickness measurement, the white ice can be divided into two categories. The thinner white ice, ranging in thickness from 0.36 to 0.76 m, has an average thickness of 0.59 m, whereas the thicker white ice, ranging from 0.81 to 1.5. m, is on the average 1.18 m thick. This is just twice the thickness of the thinner white ice. At first, it was thought that the thicker white ice represented rafted ice as compared to the thinner ice which was not rafted. On closer examination of the salinity depth profile, however, all stations, with the exception of A2 and I3, have some evidence of rafting. Thus, the thicker ice had

41

some rafting which recently doubled its thickness, as compared to the thinner ice, which rafted at an earlier stage.

The grey ice thickness varied from 0.105 to 0.255 m. The average was 0.17 m. The grey ice was always snow-free, but covered with a hoarfrost layer. During the AIDJEX experiment (Ramseier, unpublished data), it was observed that the hoarfrost layer on the Beaufort grey sea ice contained a very high concentration of brine. This was again observed during the Bering Sea experiment. Several measurements were attempted on the salinity of this layer, but the salinity was so high as to be beyond the range of the conductivity bridge, i.e., greater than 40 ppt. A moist brine layer was usually found on top of the grey ice. Based on the assumption that this layer was a thin film of brine and taking into account the measured surface temperature of the ice, it was calculated that the brine concentration must have been of the order of 260 ppt in this film. The thickness of this layer could not be established. Its importance in terms of microwave emission will be discussed later.

The amount of snow which covered the test area was minimal. As mentioned earlier, the grey ice was snow-free. The snow thickness over the rest of the area varied from 0.015 to 0.16 m. The average amounted to 0.08 m. The snow density was of the order of 0.237 $g.cm^{-3}$.

2.3.2 Physico-chemical Properties

In Table 2.1, the surface properties obtained by extrapolating the bulk properties in Figures 2.6-2.15 are given. The surface salinity varied from 1.9 to <20 ppt. On the average, the surface salinity was 12.4 ppt. The lower surface salinities can be associated with thicker ice and lower densities. Even though no distinct snow ice features were visible, there are three cores, A1, A3, and I1,

which have the lowest surface salinities and also the lowest densities. Two of the cores, A1 and I1, are also among the thickest ice. We are not certain that the top layer of these samples was snow ice, since measurements taken during AIDJEX indicated the salinity of snow ice always to be less than 1 ppt whereas the present samples were about 2 ppt or more. A better explanation may be the occasional occurrance of warmer periods which cause brine drainage, resulting in a lower surface salinity and surface density. This holds particularly for station I1 where the salinity dropped to 1.9 ppt, and the thickest ice and the lowest densities were measured.

The surface temperatures were obtained by inserting the silicone probe either directly at the snow-ice interface or in 0.003 m deep hole into the snow-free surface. The temperatures thus obtained varied between -6.6 and -12.4°C, being on the average -9.4°C.

The average density for grey ice was found to be 0.900 g.cm^{-3}, compared to 0.885 and 0.881 gm cm^{-3} for the thin white ice and thick white ice, respectively.

In conclusion it can be said, based on the extent of rafting, that the ice had undergone a large amount of strain since in 11 out of 13 cases, not counting the grey ice, rafting had occurred at least once.

The inclusion of organic material (algae and plankton) was also noted during the structural studies by the discolored ice in certain portions of the core, but particularly during the salinity measurements. Based on visual observations, a brownish-appearing melt of a sea ice wafer was classified as A^{++}, whereas slightly discolored melt which was just visible was classified as A^{--}, the values in between being A^{+}, A, and A^{-}. These qualitative measurements have been indicated on the depth axis. Out of 20 cases organic matter was observed in 15.

2.3.3 Electrical Properties of Frazil and Columnar Ice

The dielectric constant (ϵ_r') and the dielectric loss (ϵ_r'') were determined for a number of ice samples brought back from the Bering Sea to the laboratory in Ottawa. In the case of the frazil ice samples, some of the brine had drained out, which is reflected in the lower salinities measured in the laboratory. The salinities of the columnar ice samples are in accordance with bulk salinities measured in the field. The measurements were made at a frequency of 10 GHz (Vant, et al. 1975). The results are shown in Figure 2.17 where the dielectric constant and the dielectric loss have been plotted as a function of temperature. Curves 1 and 2 were obtained from frazil ice with a density of 0.836 g.cm and a salinity of 4.4 and 3.2 ppt respectively. In the case of columnar ice with the electric field perpendicular to the brine pockets, curves 3 and 4 resulted, having a density of 0.878 and 0.896 g.cm and a salinity of 3.2 and 4.6 ppt respectively. The dielectric constant and loss rise sharply at higher temperatures for frazil ice as compared to columnar ice. This is of particular interest since the measurements during the Bering Sea experiment were made at higher temperatures and even more important that for all practical purposes the ice from which the measurements were made was frazil ice. As will be pointed out in Paper No. 4, the skin depth for the microwave radiation in the first-year sea ice is such that the observed radiation emanates largely from the frazil ice layer at all the wavelengths studied here.

2.4 GENERAL ICE MORPHOLOGY

A photomosaic of the US test area on March 5 is shown in Figure 2.18. The elements consist of contact prints, 12.70 × 12.70 cm, of the film used in the

7.62 cm focal length camera. Only a part of the test area is photographed because the field-of-view of the aerial camera was not sufficient to cover the entire distance between aircraft tracks from the altitude flown, 11 km. Figure 2.19 shows that there were numerous open water leads in the test area, particularly in the southwestern and southern sectors. Cloud obscuration in the northeastern sector precludes determining whether the polynyas observed were open water or refrozen. Of particular interest is a parallelogram-shaped region of grey ice, about 8 km on a side, which appears at the center of the mosaic. As indicated in Figure 2.18, the surface test point A3 was located at the northwest corner of this grey ice area. The exact location of A3 was determined by comparing the photomosaic element print with 35 mm slides obtained from the helicopter and on the surface.

A false-color representation of the 1.55 cm brightness temperatures recorded over the US test area is shown in Figure 2.19. Here, the measured brightness temperatures have been divided into twenty intervals and each interval has been assigned a color. Generally, the microwave image shows the same lead and polynya patterns as the photomosaic with lower spatial resolution, but without cloud obscuration. With the particular color representation chosen, the large white areas are not entirely open water, but contain grease ice and ice fragments, as evidenced in the digital printouts of the brightness temperatures represented in Figure 2.19. The surface test points, A1-A5 and I2-I4, have been indicated on Figure 2.19, as well as the areas of overlap with the USSR photomosaic and radar mosaic obtained on the same day. Due to a malfunction in the inertial navigation system of the aircraft which occurred during the descent for the low-level diagonal pass, we did not succeed in following the prescribed path from the northwest

45

corner of the test area to the southeast corner. The actual low-level diagonal path of the aircraft is indicated also on the microwave mosaic. While the large grey ice area in the center of the test area was missed as a result, smaller areas of similar ice were encountered during the low pass.

The grey ice feature in the center of the test area is of special interest, since its brightness temperature corresponds to that of multiyear sea ice (Gloersen, et al., 1972, 1973). However, the data presented earlier from surface test point A3G identify the parallelogram feature as grey ice without snow cover. As has been pointed out (Section 2.3.1), the grey ice had a thin wet film on the surface. Apparently, sublimation of the ice from the surface of the sea ice leaves behind a sufficiently high salinity at the surface to lower the melting point to the surrounding air temperature (262°K). This feature was also observed with the 21 cm and the horizontal polarization channel of the 0.8 cm radiometers, in both cases resulting in a 10 to 15°K drop in brightness temperatures. In the case of the 21 cm radiometer, part or all of this decrease might be attributed to thin ice. (See Paper 3.) Within the noise limitations, none of the other micro-wave radiometers responded to this feature.

For the purpose of relating these observations to what might be observed from satellite altitudes, the US test area was divided into sections of various sizes and histograms of the fractional number of observations at various bright-ness temperatures were produced. In Figure 2.20, the US test area was divided into 25 approximately equal sections, and the number of observations in various 3°K brightness temperature intervals were tabulated. To facilitate the comparison between the various histograms presented, the data are normalized to 100 observations per sector, i.e., are given as percentages. It can be seen that

sectors containing largely consolidated first-year ice are characterized by narrow distributions, with the peak occurring at 246°K, as for example in the northwestern sectors. The central sector has a different signature, a flatter distribution and a peak shifted about 10°K lower, corresponding to the grey ice parallelogram discussed earlier, for the most part. A third category of histograms occurs as the concentration of the ice decreases, as in the southern central sectors. The open water in these areas causes a characteristic flattening of the distribution and a shift of the peak to lower brightness temperatures, the amount of shift and flattening being dependent on the ice concentration. The area of these sectors is nearly the same as the spatial resolution element of the 1.55 cm scanning radiometer on board the Nimbus-5 satellite. The satellite radiometer, of course, would read only the average brightness temperature for the entire sector.

The test area was divided also into five strips, corresponding to the five aircraft tracks flown over the area. The histograms resulting from the tabulation of the data in each of these strips are shown in Figure 2.21. It can be seen that differences in the histograms occur even for the coarser spatial resolution of the strips.

Similar studies with the data from the other microwave radiometers were not attempted since their coarser spatial resolution and lack of scanning would not yield enough observations for a meaningful histogram. However, wavelength dependence for the two most radiometrically distinguishable ice types, grey ice and thick first-year ice, was examined. The results are shown in Figure 2.22. The data were obtained at high altitude. The grey ice statistics were obtained from the middle 1/5th of the central high altitude aircraft leg, over the

47

parallelogram feature described earlier. The thick first-year data were obtained from the northernmost 1/5th of the westernmost aircraft leg. The lack of coincidence of brightness temperatures profiles over thick first-year ice for the various wavelengths can probably be attributed to imperfect absolute calibration of the various radiometers. It is the relative signatures from grey ice to thick ice that is noteworthy. It is also noteworthy that the 2.8 cm radiometer displays polarization over both ice types; this was not observed at 0.8 cm, possibly because of atmospheric interference by liquid water droplets in the haze.

2.5 SUMMARY AND ASSESSMENT

During the 5 March Bering Sea Experiment, no multiyear ice was definitely identified either remotely from the aircraft or during the surface measurement activities. An heretofore unreported phenomenon relating to grey ice was observed. It was found that grey ice, with a moisture film on the surface resulting from high salinities, gives rise to a lowering of the emissivity of the ice at the shorter wavelengths. This, in turn, results in an ambiguity when attempting to identify multiyear ice entirely by remote microwave sensing, since the emissivity is lowered by comparable amounts for both ice types, compared to thick, snow-covered first-year sea ice. This ambiguity can be diminished by observing the shape of the sea ice feature in question; the grey ice features are likely to have angular and extended boundaries while multiyear features would tend to appear more rounded. Another such ambiguity arises when attempting to determine if a lead observed in a microwave image is fully resolved and filled with moist grey ice or is partly resolved and open. The latter ambiguity probably cannot be resolved.

Another feature observed during this experiment was the lowering of the

long wavelength microwave brightness temperatures when thin first-year ice

was encountered. Similar features have been observed during earlier Arctic

experiments (Gloersen, et al., 1972). This phenomenon is discussed in more

detail in Paper No. 4.

In comparing these data with those obtained by the Soviet scientists in the

overlap areas, we find them to be substantially in agreement, with any differ-

ences in detail probably attributable to the dynamic nature of the sea ice and

the sequential nature of the data acquisition.

REFERENCES

Gloersen, P., T. Wilheit, and T. Schmugge, "Microwave emission measurements of sea surface roughness, soil moisture, and sea ice structure," 4th Annual Earth Resources Program Review 1, 8-1 (1972) (NASA/JSC Document MSC-05937)

Gloersen, P., W. Nordberg, T. J. Schmugge, and T. T. Wilheit, "Microwave signatures of first-year and multiyear sea ice," J. Geoph. Res. 78, 3564 (1973)

Meeks, D. C., R. O. Ramseier, and W. J. Campbell, "A study of microwave emission properties of sea ice-AIDJEX 1972," Proc. 9th Int. Symp. on Rem. Sensing of Environment (University of Michigan 1974) (In press).

Reed, R. J., and W. C. Campbell, "The equilibrium drift of Ice Station Alpha," J. Geoph. Res. 67, 281 (1962).

Vant, M. R., R. B. Gray, R. O. Ramseier, and V. Makios, "Dielectric properties of fresh and sea ice at 10 GHz and 35 GHz (To be published (1975)).

Zubov, N. N., "Wind and the drift of ice," H. O. Translation 217 of Chapter 8, Dynamic Oceanology, (1947) (Technical Service Branch, Division of Oceanography, U. S. Navy Hydrographic Office, pp. 336-353).

Table 2.1

Surface Station Data

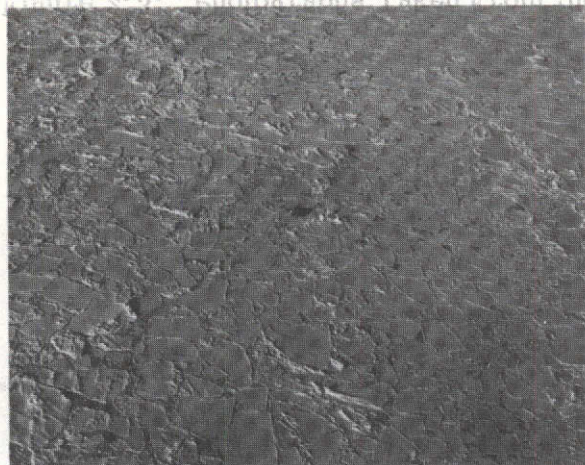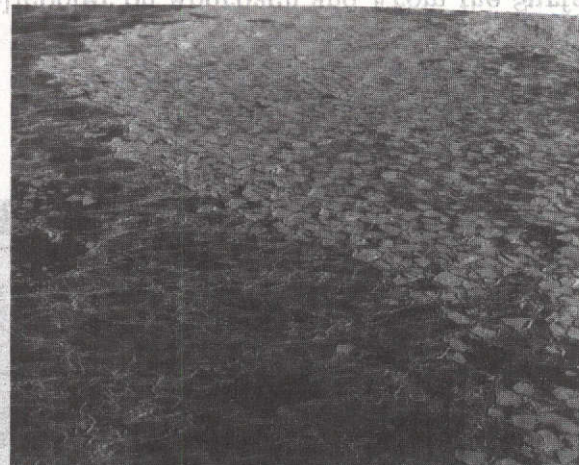| Station	GMT		Location		Ice Thickness, m (h_I)	Frazil Ice Layer Thickness, m (h_F)	Snow Thickness, m (h_s)	Surface Salinity, ppt (S_s)	Surface Temperature, °C (θ_s)	Surface Density, g.cm^{-3} (ρ_s)
A5	5 Mar	2100	61°43.4'N	175°35' W	0.71	< 0.36	0.095	10.3	9.4	0.910
A4		2130	61°50.5'N	175°47.4'W	0.76	0.21	0.09	—	11.8	0.873
A4G		2130	61°50.5'N	175°47.4'W	0.22	0.05	0	15.2	11.7	0.892
A3		2210	61°58.6'N	176°04' W	0.64	0.16	0.03	5.1	9.0	0.843
A3G		2210	61°58.6'N	176°04' W	0.255	0.135	0	< 20	12.4	0.902
A2		2230	62°05.1'N	176°19' W	0.36	0.10	0.015	14.8	—	0.853
A1		2345	62°12' N	176°33.5'W	1.30	0.10	0.11	4.6	—	0.851
I4	6 Mar	0030	61°31.5'N	176°28.5'W	0.455	0.05	0	< 20.3	11.0	0.907
I3		0050	61°36.3'N	176°38.1'W	0.60	0.09	0.11	15.5	6.4	0.898
I3G		0050	61°36.3'N	176°38.1'W	0.115	0.05	0	19.6	8.6	0.918
I2		0120	61°42.5'N	176.50.5'W	1.07	0.32	0.095	11.8	7.6	0.865
I1		0145	61°48' N	177°03' W	1.51	0.22	0.09	1.9	10.4	0.852
R1		2100	61°25.2'N	178°17.5'W	0.48	—	0.025	21.6	10.6	0.918
R1G		2100	61°25.2'N	178°17.5'W	0.12	0.03	0	12.1	10.6	0.915
R2		2135	61°25.8'N	178°03' W	1.14	0.05	0.11	9.8	7.8	0.898
R2G		2135	61°25.8'N	178°03' W	0.19	0.15	0	16.3	7.6	0.860
R3		2200	61°18.5'N	177°48.5'W	0.59	0.06	0.13	6.5	6.6	0.875
R4		2235	61°11.2'N	177°34' W	1.235	0.215	0.16	6.8	—	0.906
R5		2300	61°04.5'N	177°19.5'W	0.815	0.185	0.07	6.7	—	0.912
R5G		2300	61°04.5'N	177°19.5'W	0.105	0.02	0	16.2	—	0.914
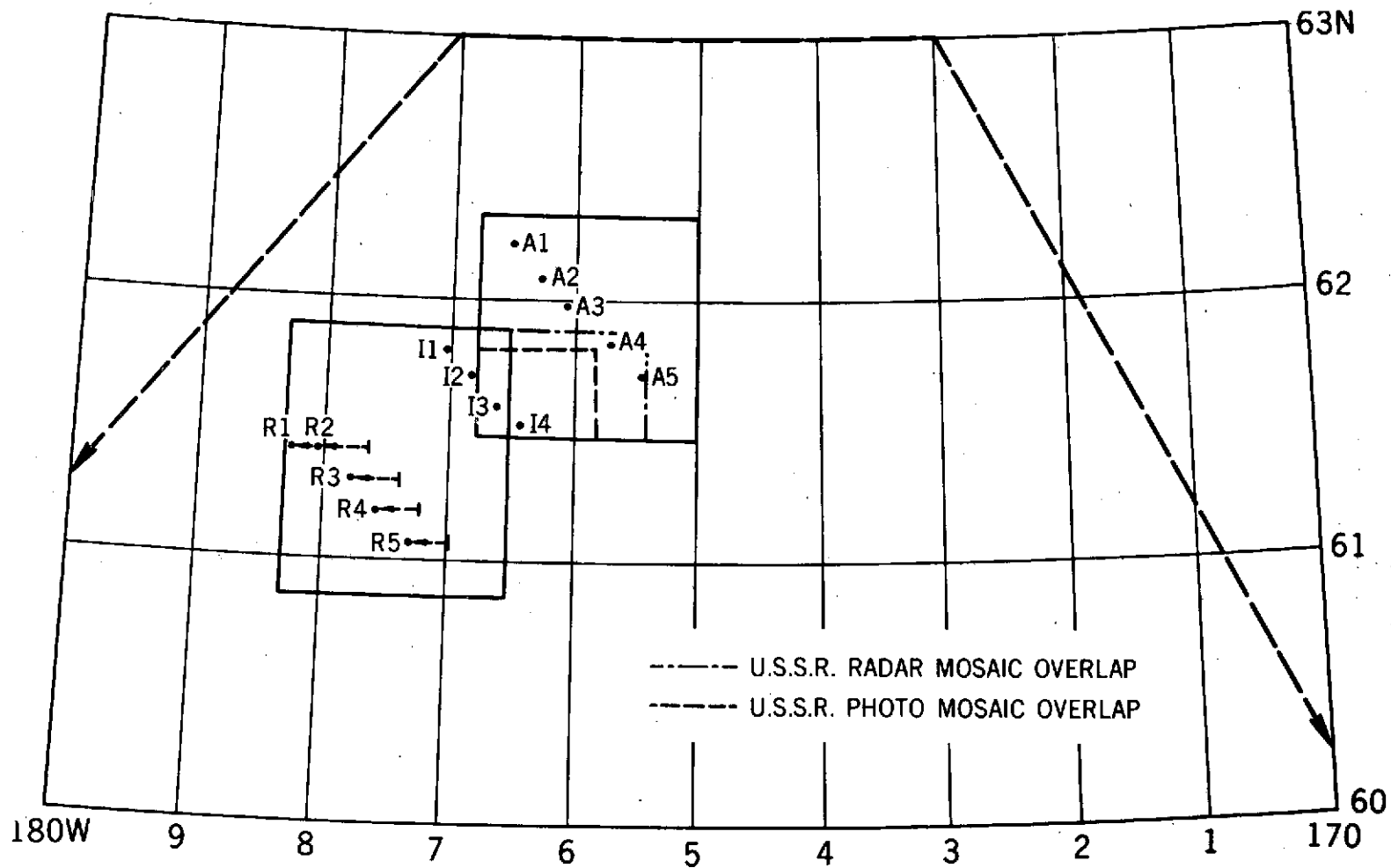
Figure 2.1. Test areas of U.S.A. and U.S.S.R. for 5 March 1973. Positions of surface truth stations are indicated as A1 to A5 for U.S.A. area, I1 to I4 for overlap area, and R1 to R5 for U.S.S.R. area. Coordinates of the stations are from Staten Island fixes. Broken lines in the U.S.A. test area indicate additional areas overlapped by the U.S.S.R. photomosaic and radar mosaic.
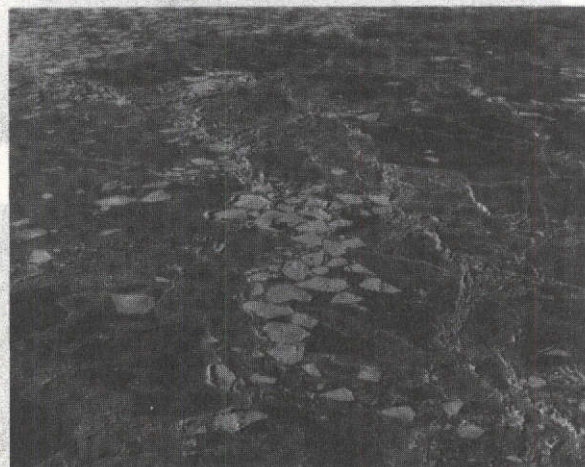
STATION A5

STATION A4

STATION A3
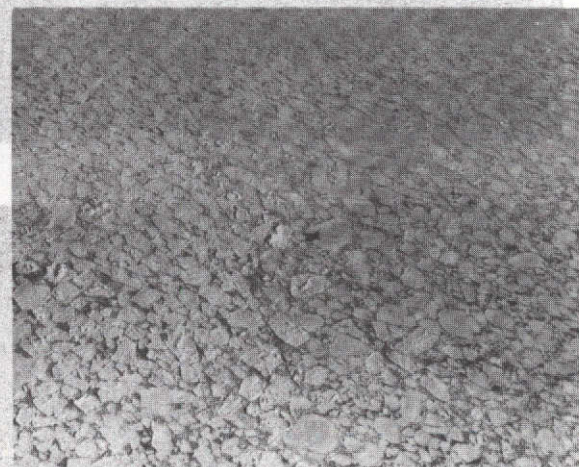
STATION A2

Figure 2.2. Aerial Views of U.S.A. Surface Test Area Stations A5-A2, Taken
From the Transport Helicopter
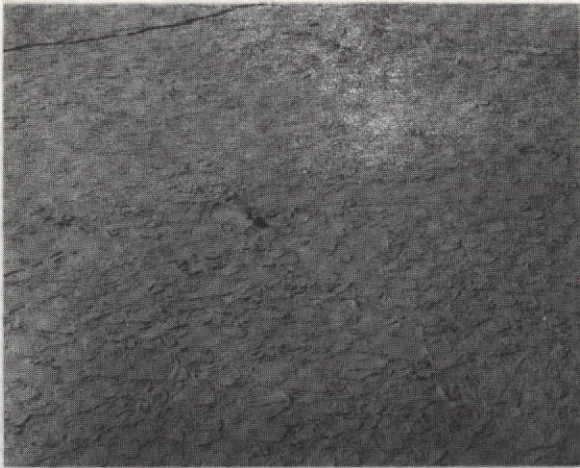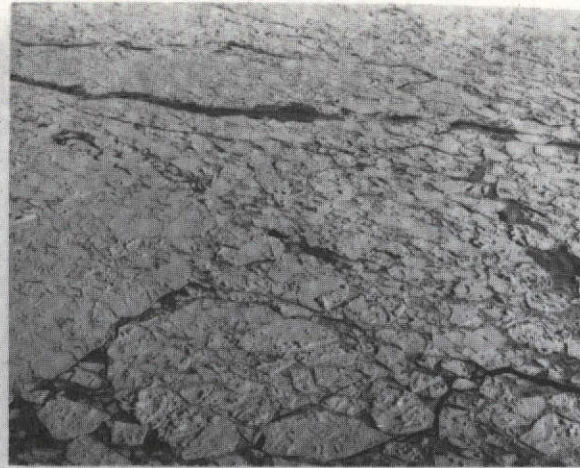
STATION A1   STATION I4
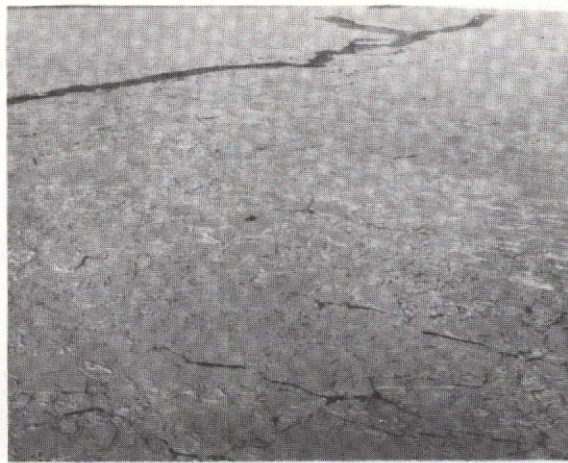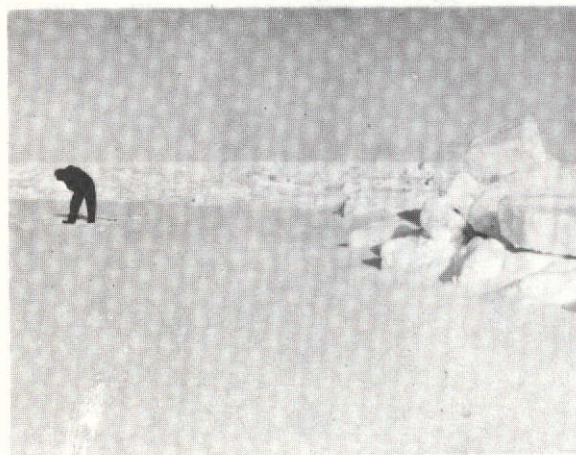
STATION I4 (IN SITU)   STATION I3

Figure 2.3.   Photographs Taken From the Helicopter on Approach and From the Surface
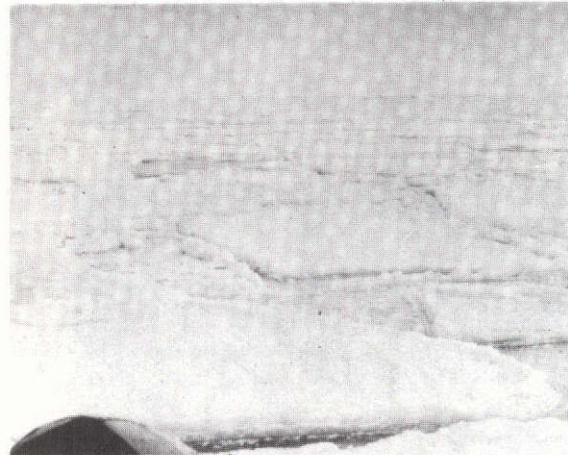of U.S.A. Area Station A1 and Overlap Area Stations I4-I3

STATION I2

STATION II

STATION II (IN SITU)

STATION RI (IN SITU)

Figure 2.4. Photographs Taken From the Helicopter on Approach and From the Surface of Overlap Area Stations I2-I4 and U.S.S.R. Area Station R1

STATION R2

STATION R3
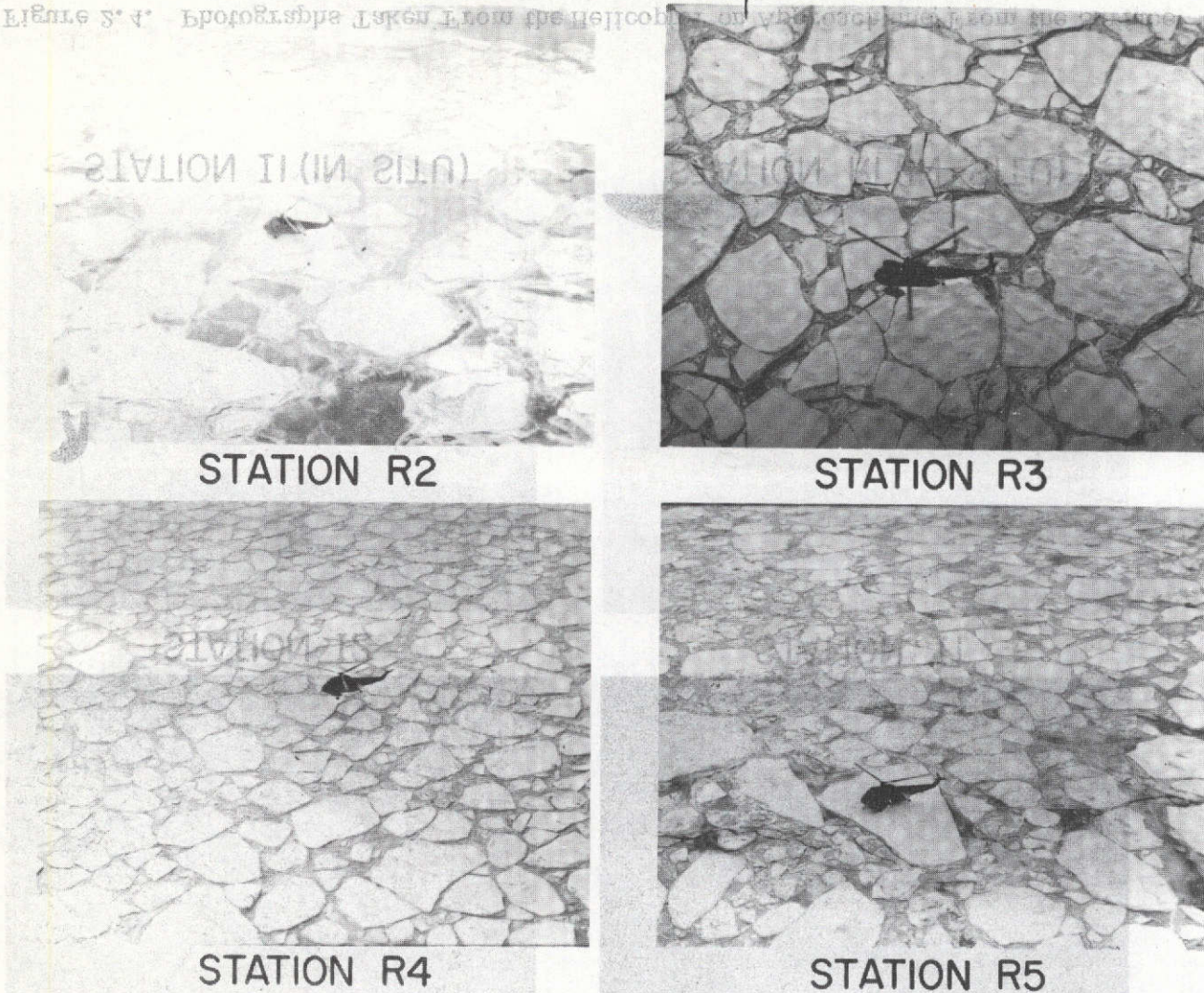
STATION R4

STATION R5

Figure 2.5. Aerial Photographs Taken From the Helicopter of U.S.S.R. Area Stations R2–R5
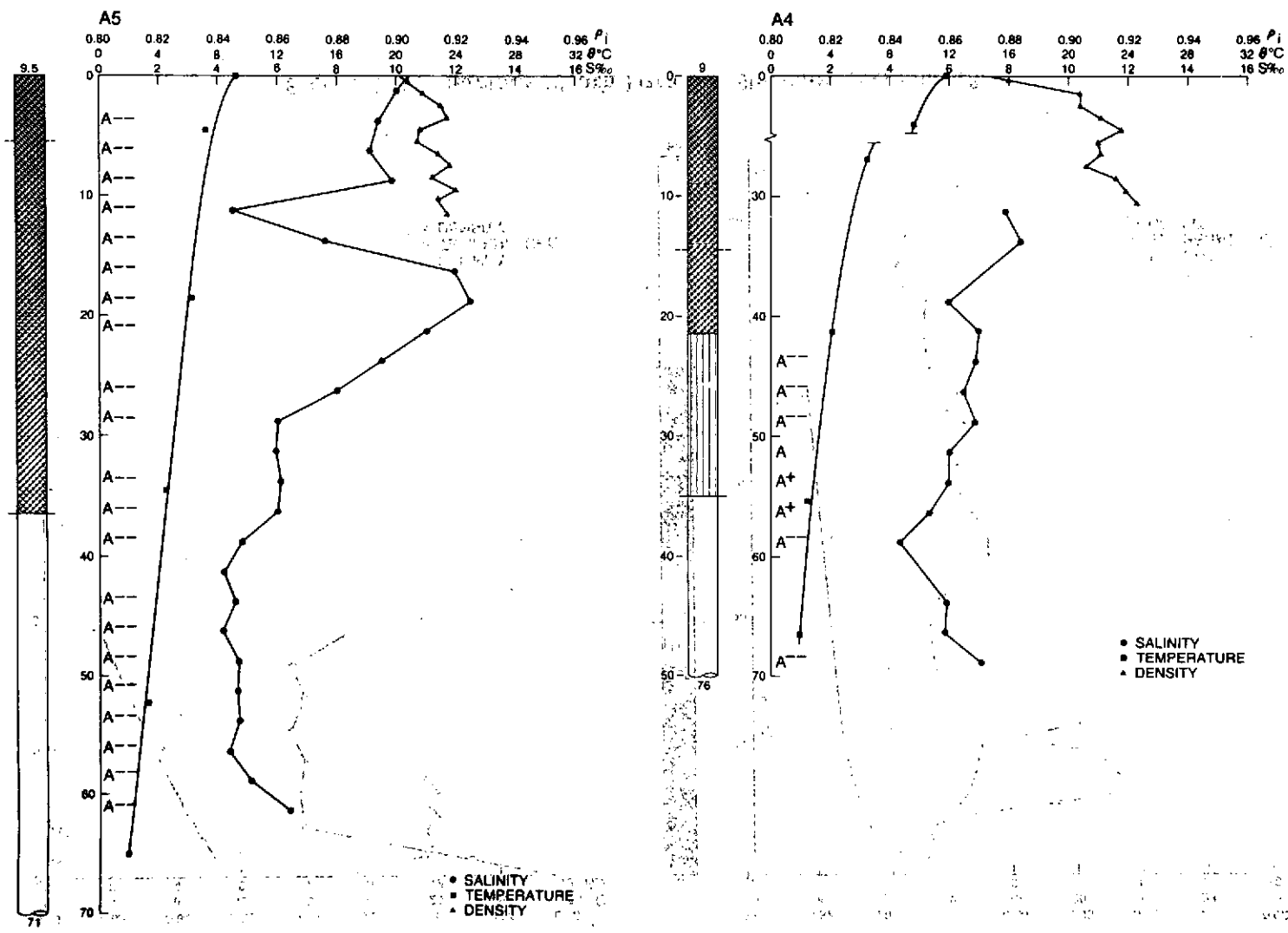
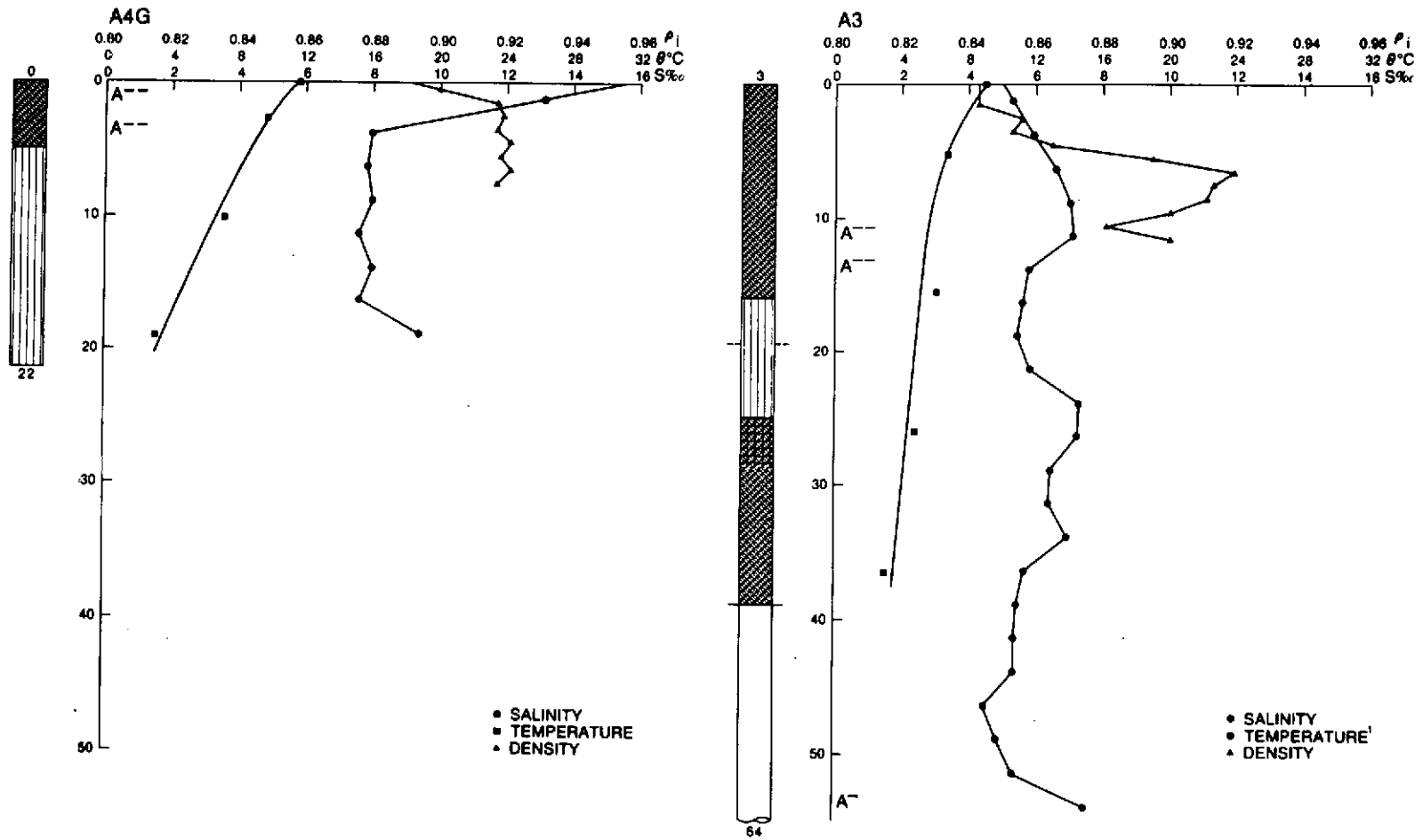Figure 2.6. Surface Truth Data for Stations A5 and A4

57

Figure 2.7.   Surface Truth Data for Stations A4G and A3

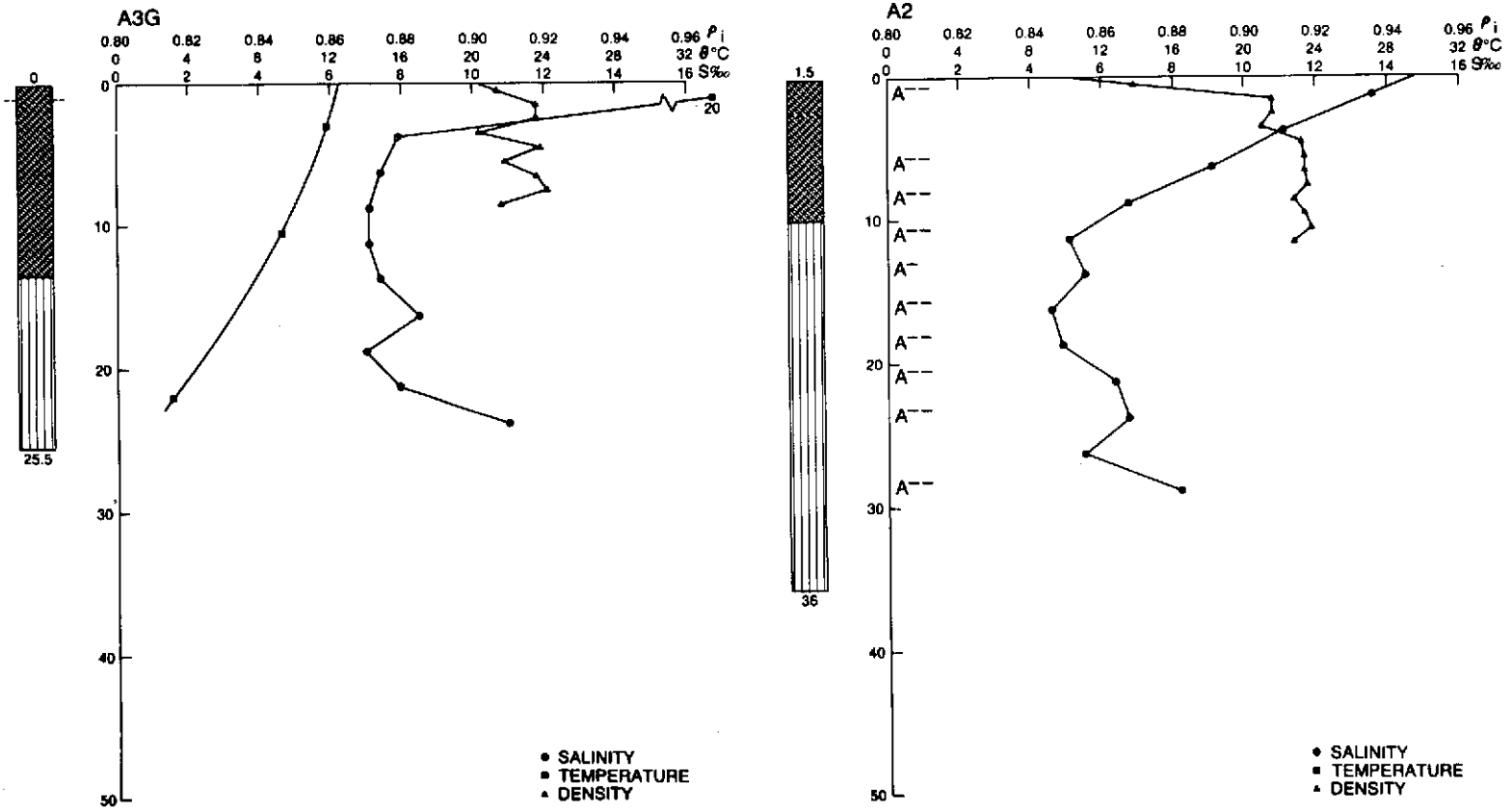Figure 2. 8.   Surface Truth Data for Stations A3G and A2

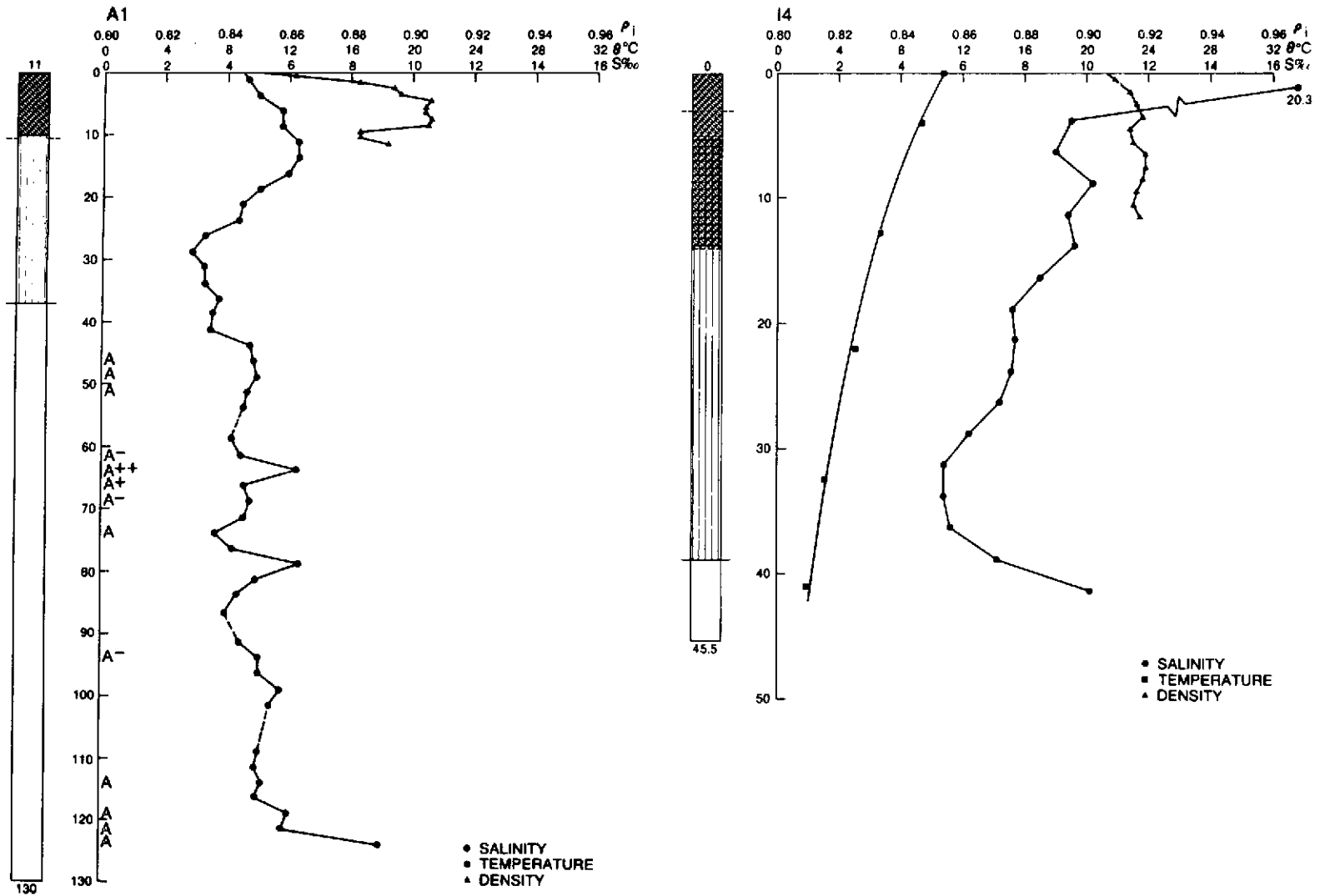Figure 2.9. Surface Truth Data for Stations A1 and I4
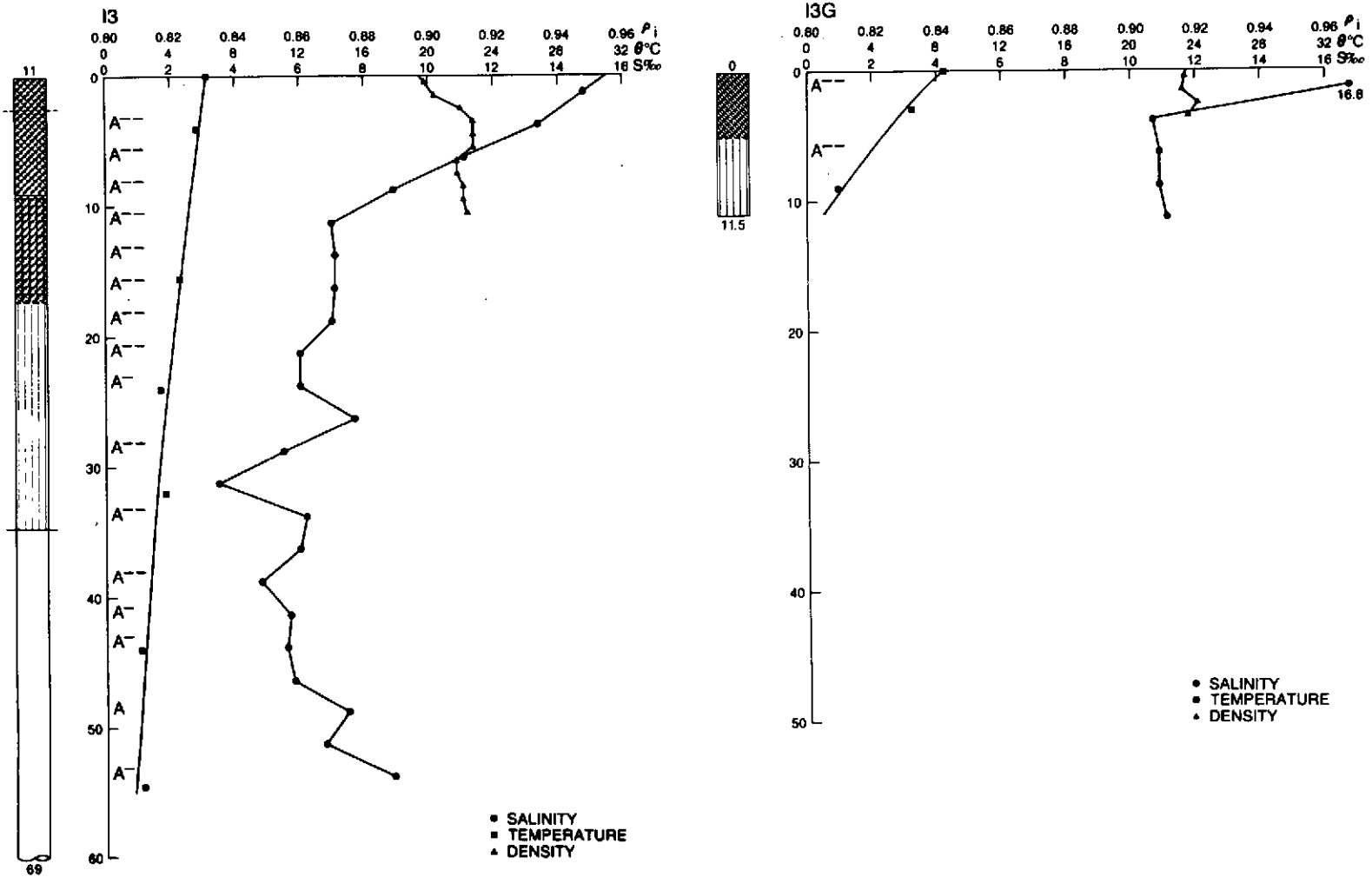
Figure 2.10. Surface Truth Data for Stations I3 and I3G

Figure 2.11.   Surface Truth Data for Stations I2 and I1

62
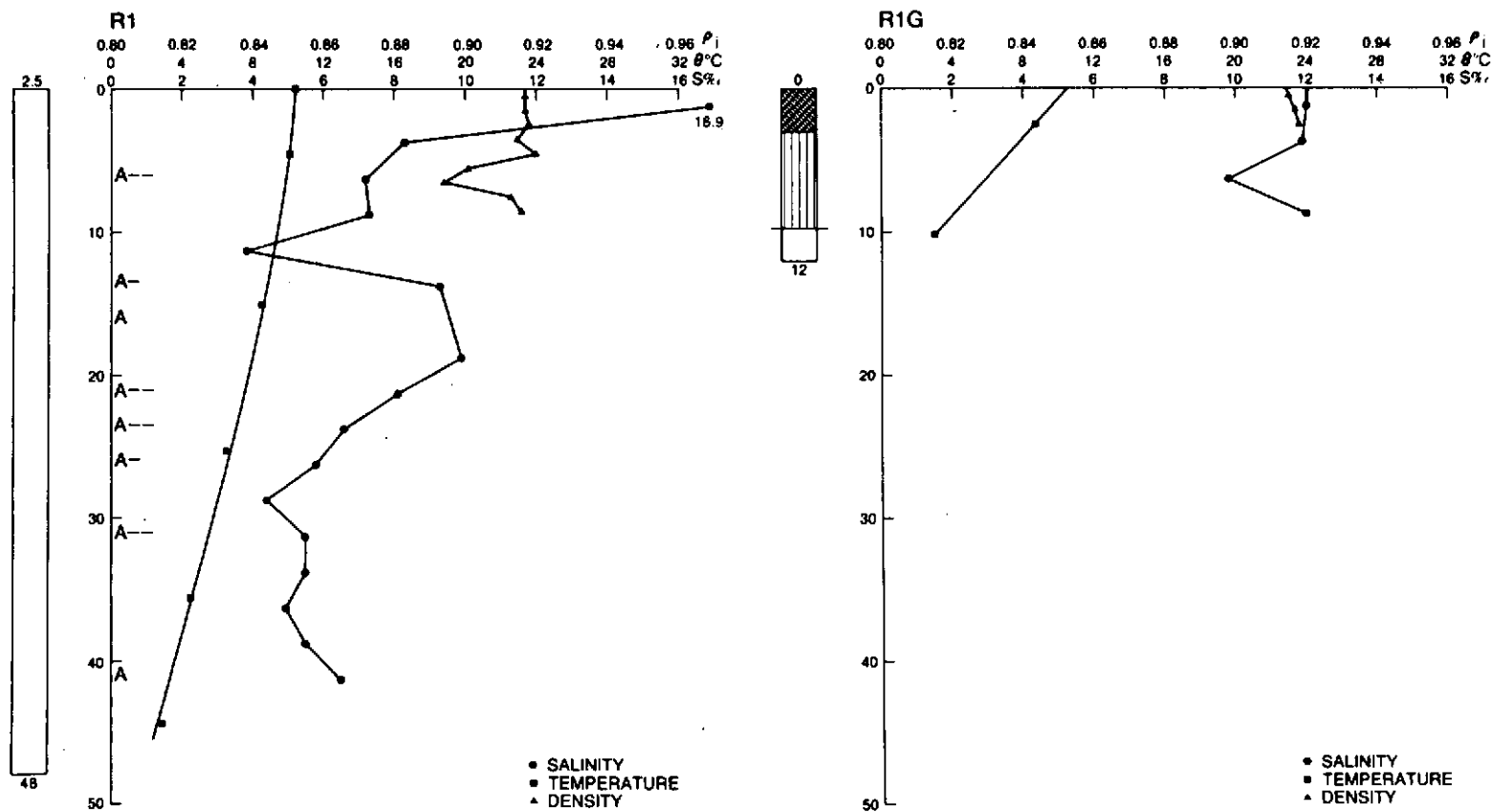
Figure 2.12.   Surface Truth Data for Stations R1 and R1G
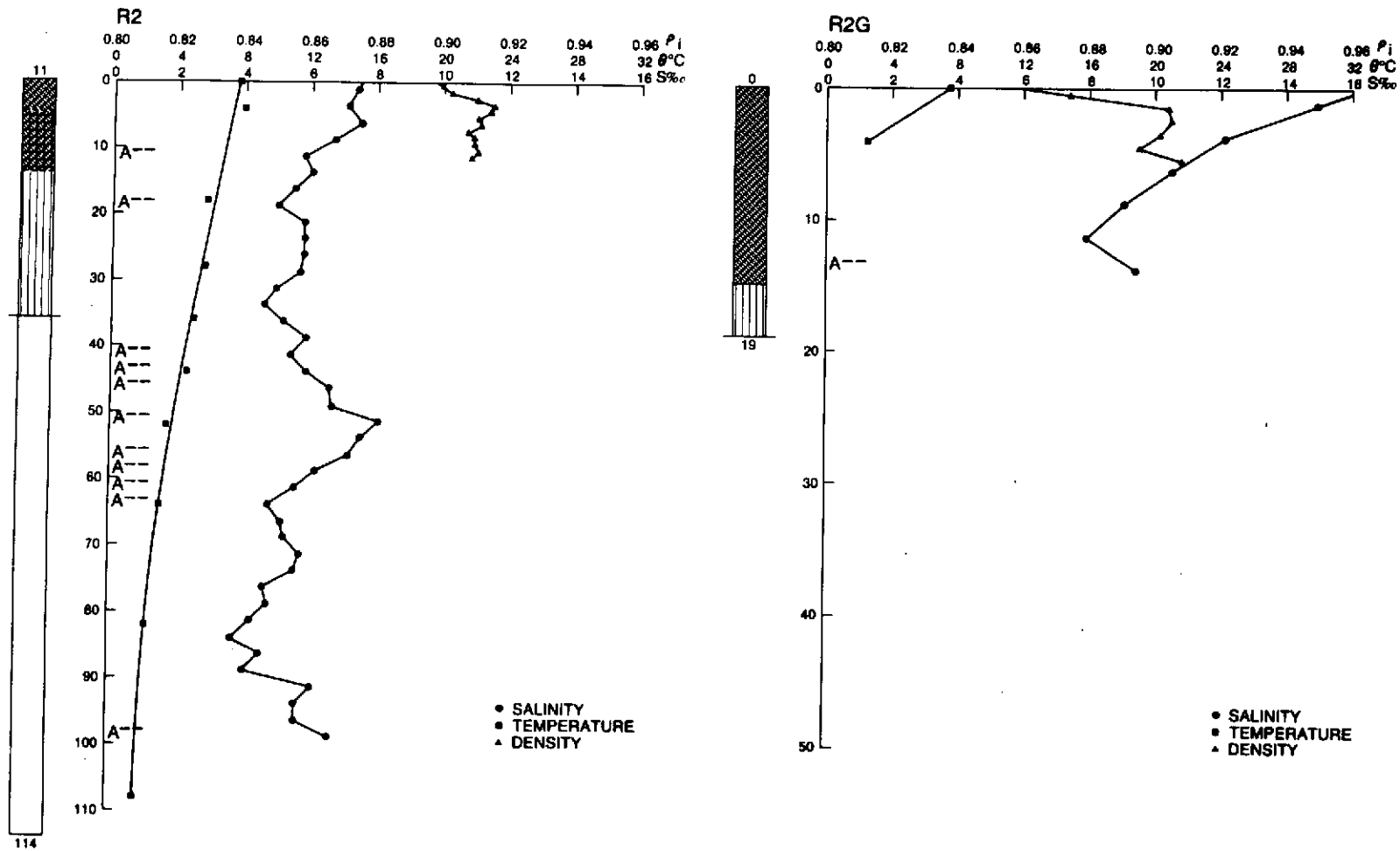
Figure 2.13. Surface Truth Data for Stations R2 and R2G

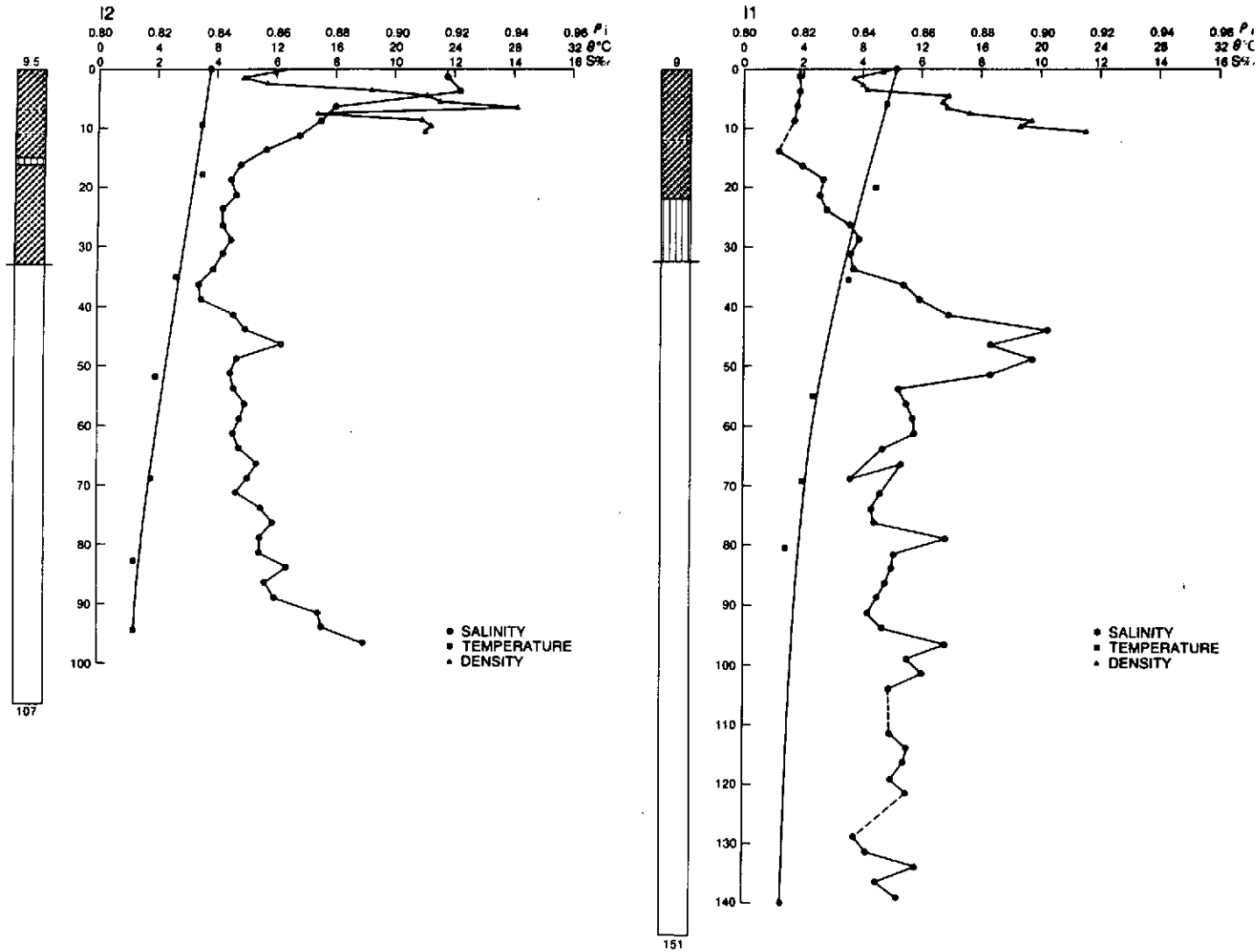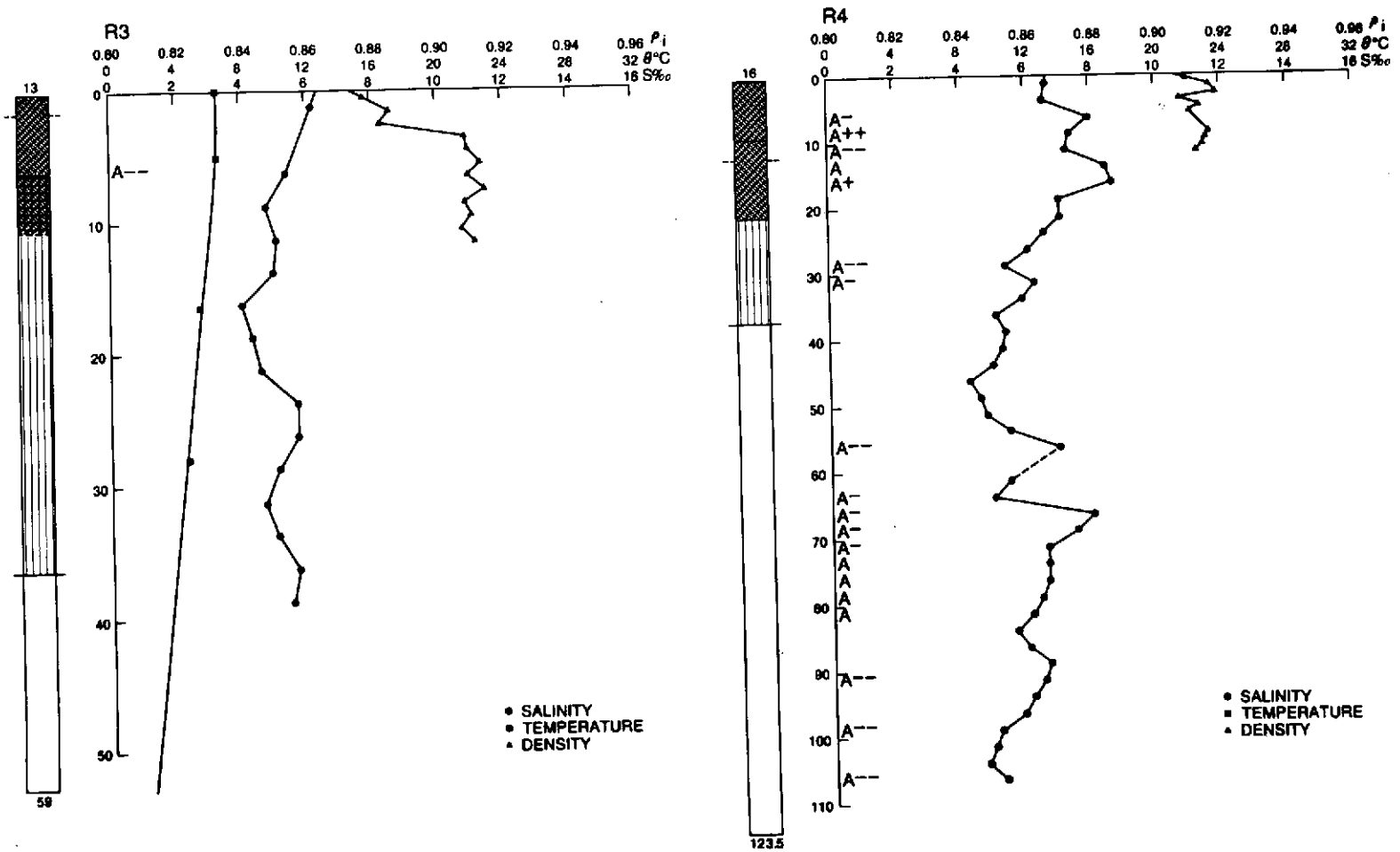Figure 2.14. Surface Truth Data for Station R3 and R4
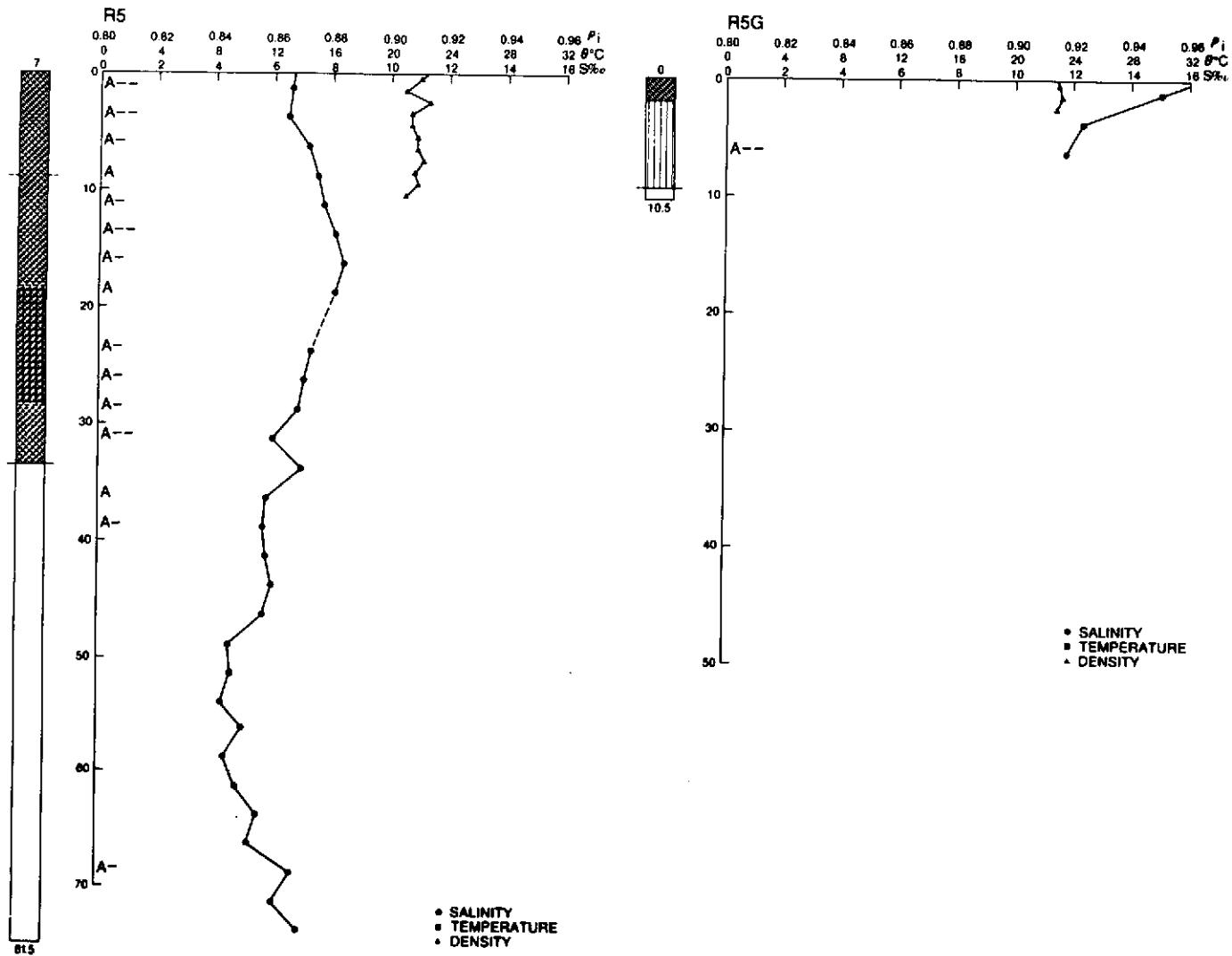
Figure 2.15.   Surface Truth Data for Stations R5 and R5G
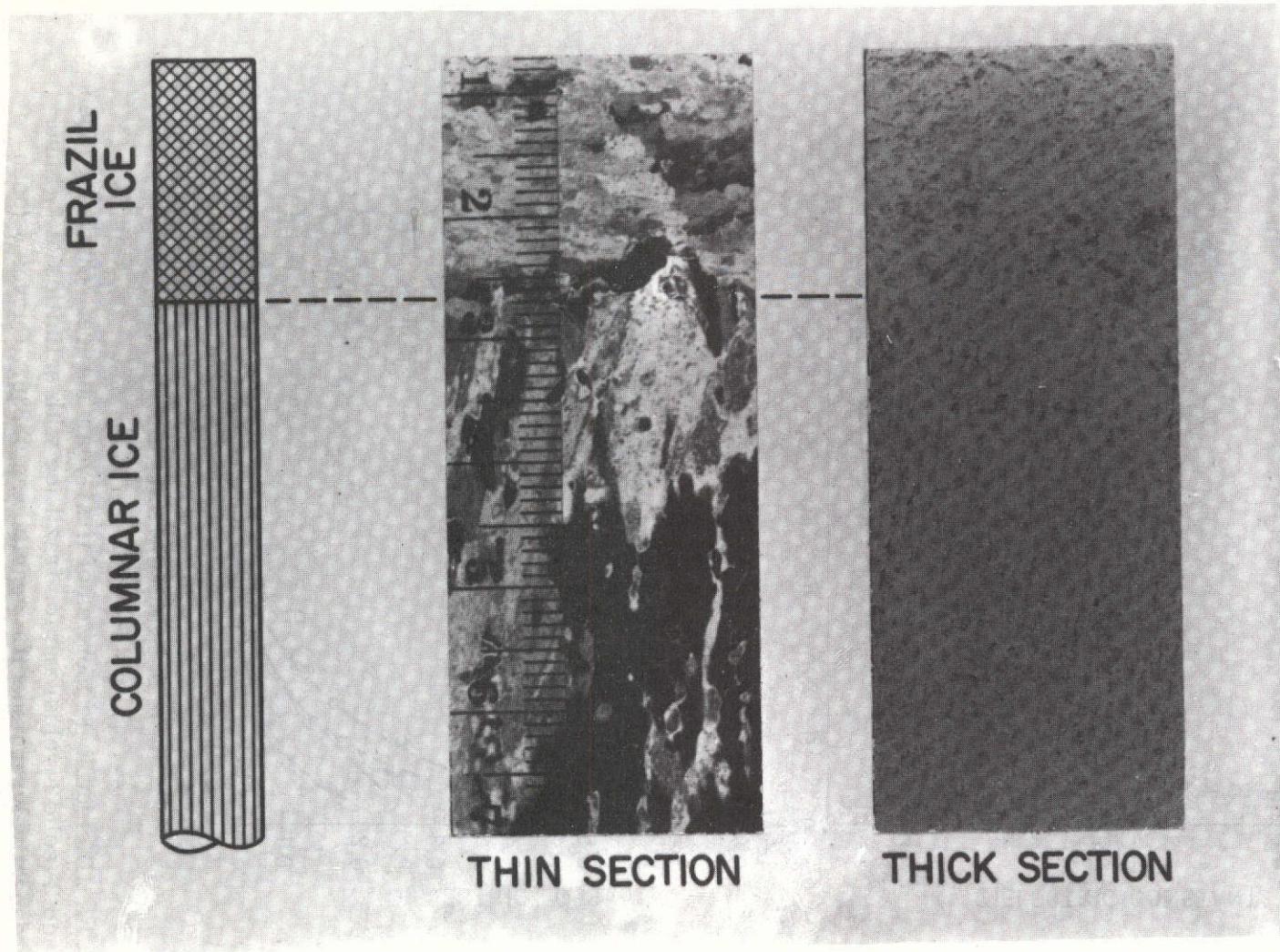
Figure 2.16. Structure, texture and brine pocket distribution for representative Bering Sea ice: a) thin ice section photographed between crossed polaroids revealing structure and texture; b) thick section photographed from transmitted light revealing structure and brine inclusions.
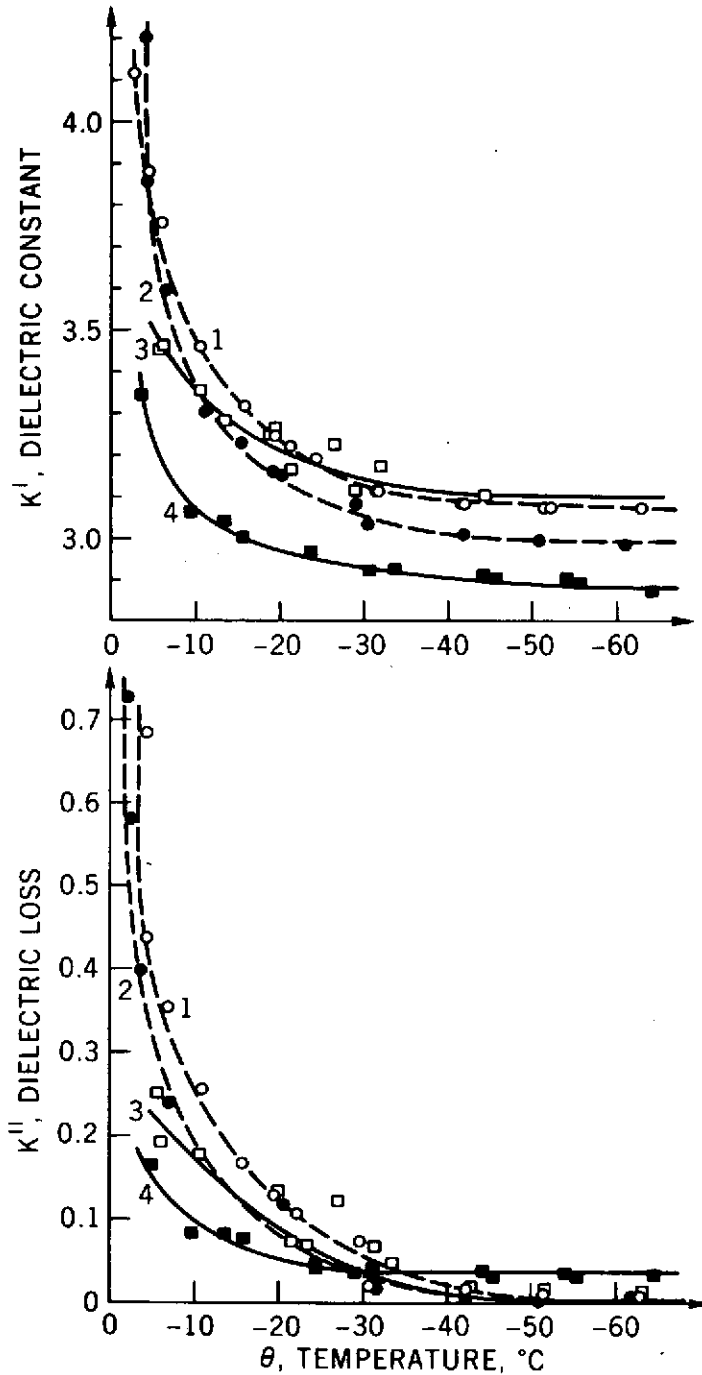
Figure 2.17. Dielectric Properties of first-year sea ice. Curves 1 (open circles) and 2 (solid circles) are for frazil ice with salinities of 4.4 and 3.2 ppt, respectively; the specific gravity was 0.836. Curves 3 (open squares) and 4 (solid squares) are for columnar ice with salinities of 3.2 and 4.6 ppt and specific gravities of 0.878 and 0.896, respectively.

5 MARCH 1973
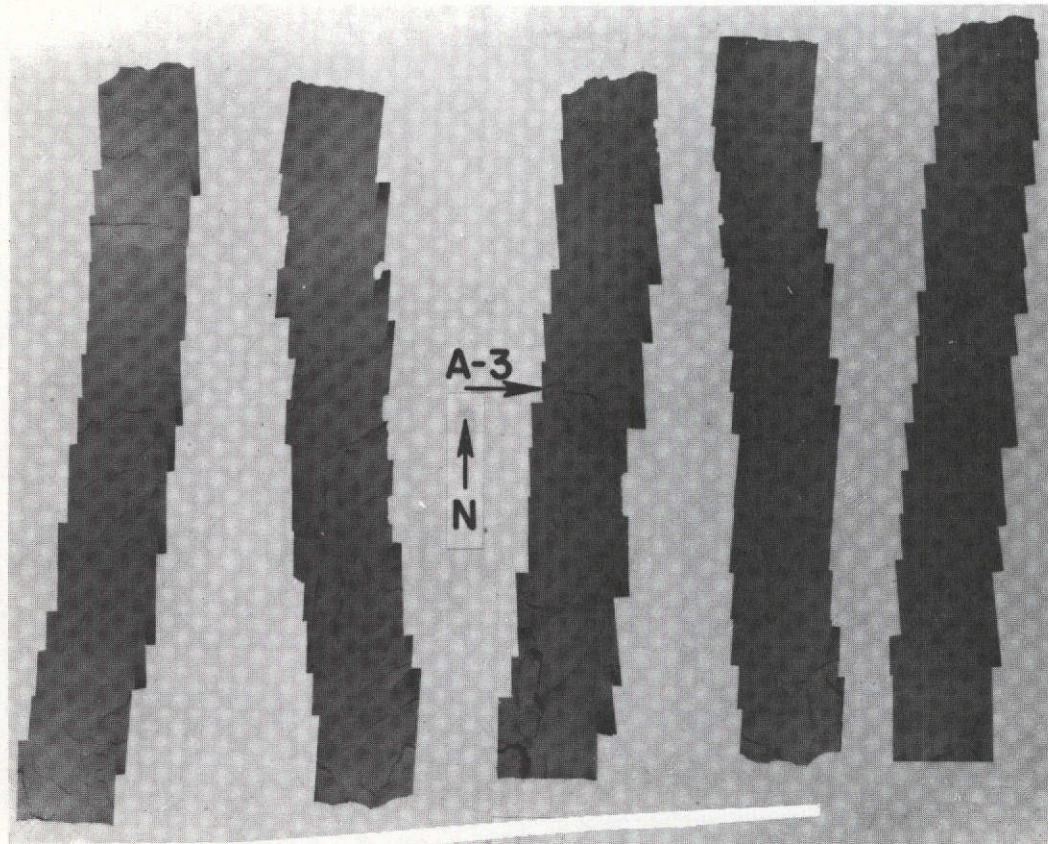
AREA: 100 Km x 100 Km
CENTER NEAR 61.8°N, 175.9°W

Figure 2.18.   Photomosaic of U.S.A. Test and Overlap Test Areas with Surface
Truth Station A3 Indicated
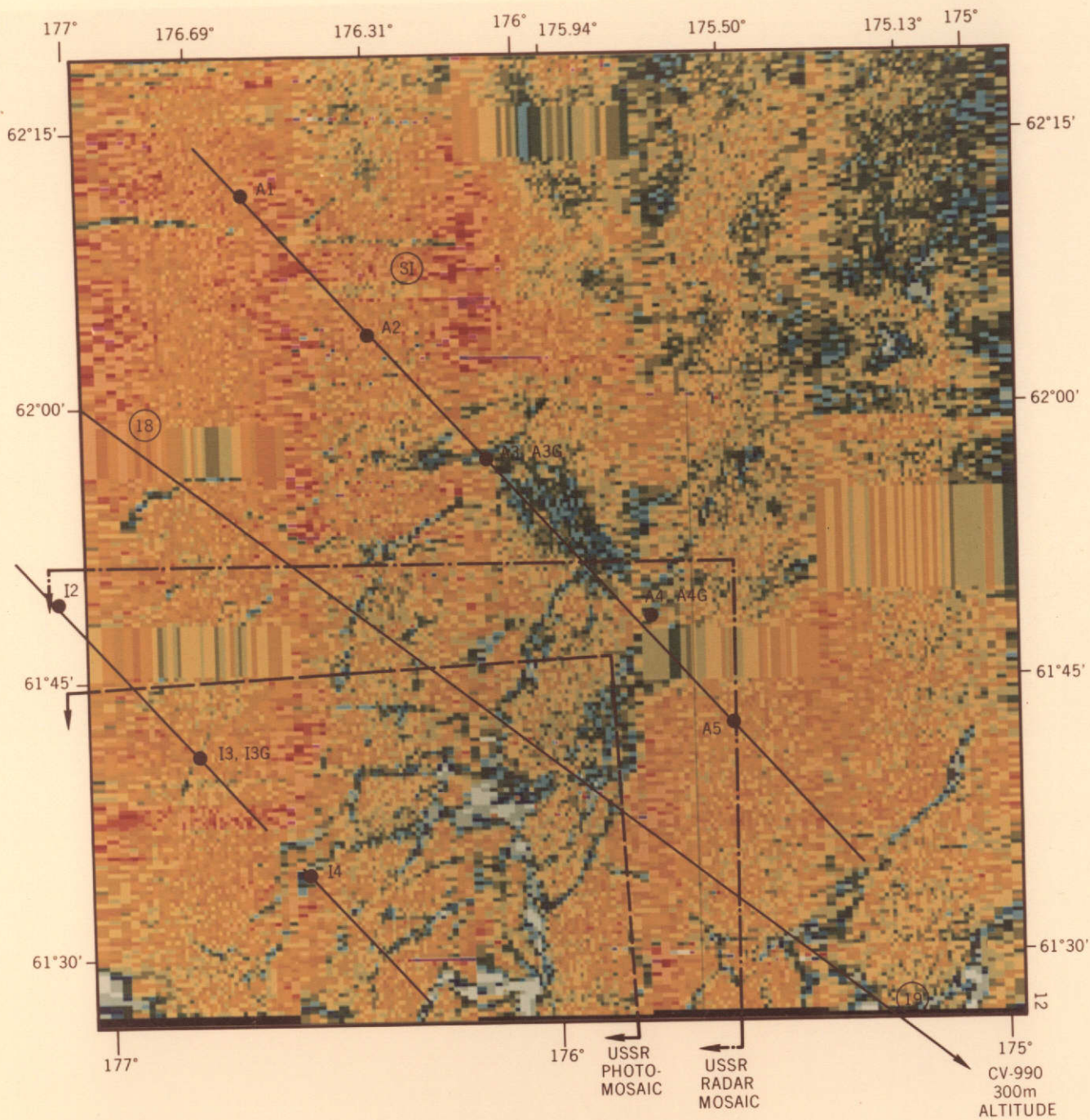
BERING SEA EXPERIMENT
5 MARCH 1973
1.55 cm IMAGE
064 22 16 ⟶ 064 23 15 GMT

LEGEND:

A1, 2, 3, 3G, 4, 4G, 5: SURFACE MEASUREMENT POINTS, U.S. STUDY AREA (DATA OBTAINED 5 MAR 73)

I2, 3, 3G, 4: SURFACE MEASUREMENT POINTS, OVERLAP STUDY AREA (DATA OBTAINED 5 MAR 73)

(SI) : POSITION OF STATEN ISLAND, 2300-2359 GMT 5 MAR 73

| 7-262 K | 262-253 K | 252-251 K | 250-249 K | 248-247 K | 246-245 K | 244-243 K | 242-241 K | 240-239 K | 238-237 K |

| 236-235 K | 234-233 K | 232-231 K | 230-229 K | 229-227 K | 226-225 K | 224-223 K | 222-221 K | 220-211 K | <210 K |
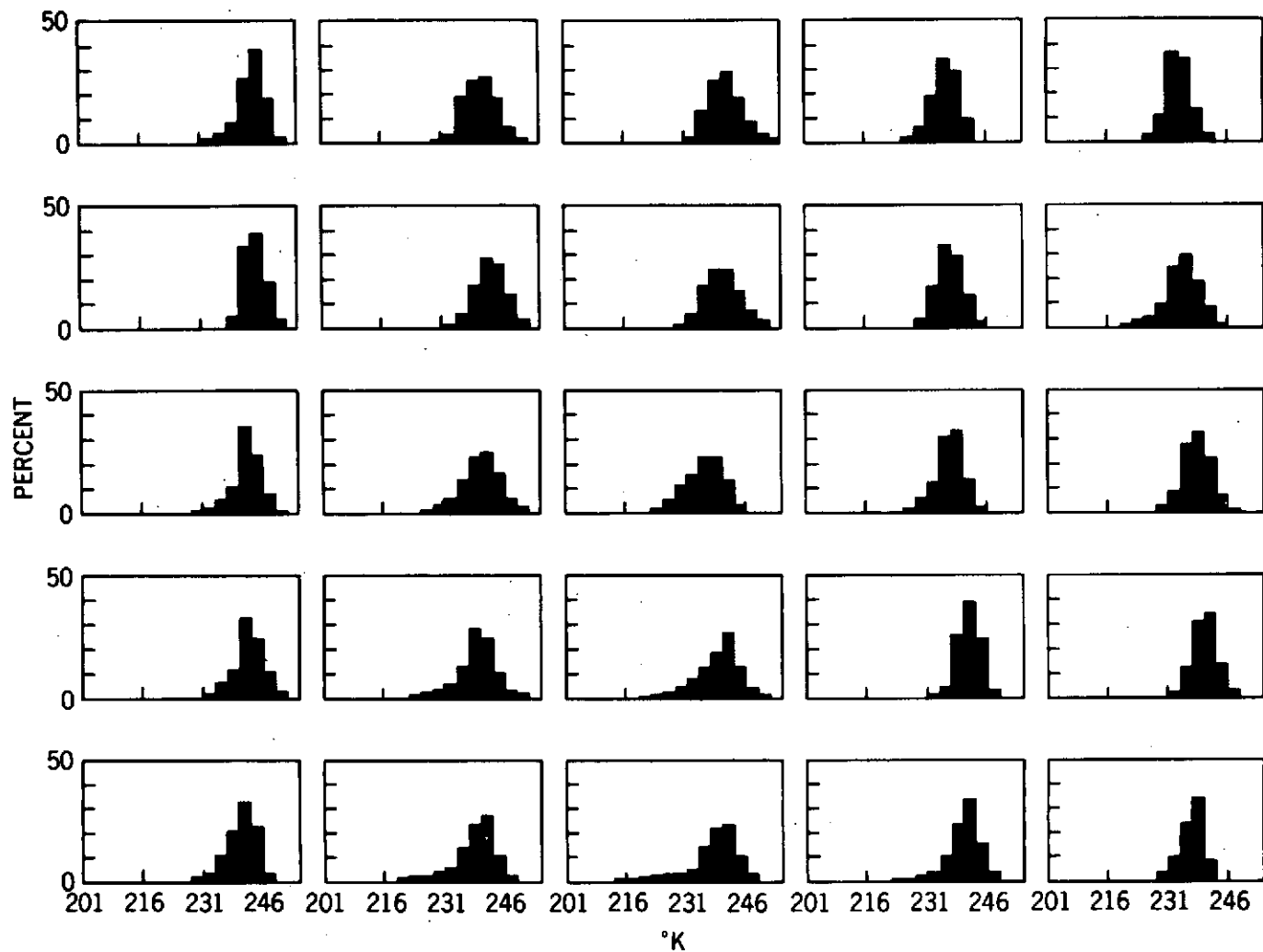
Figure 2.20. Histogram of 1.55 cm radiation emanating from U.S.A. and overlap test areas. 5 March 1973. The area shown in Figure 2.19 has been divided into 25 approximately equal areas; these are located in this Figure in approximately the correct geographical position.
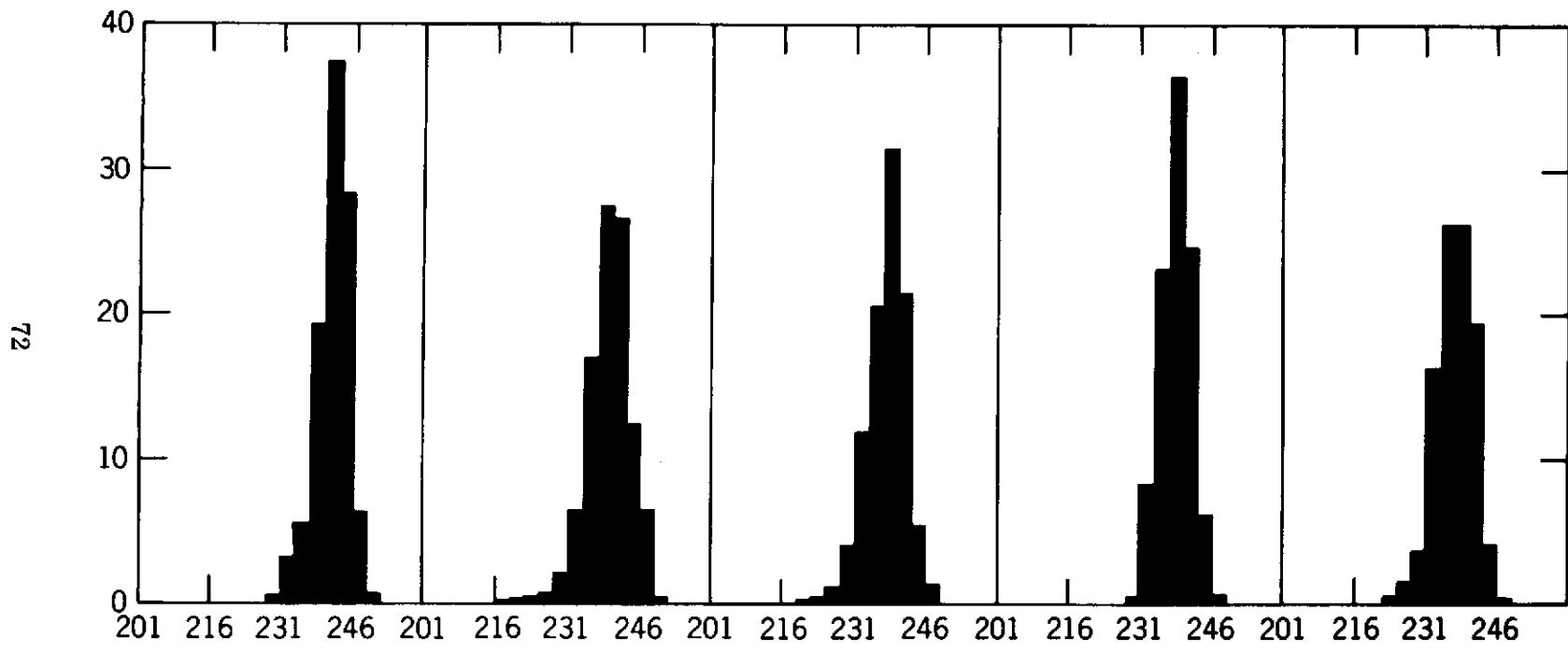
Figure 2.21. 1.55 cm histogram of U.S.A. area representing the five flight lines.
5 March 1973.

GREY ICE   THICK FIRST YEAR ICE

0.8 cm
H or V

1.55 cm

2.8 cm
H

2.8 cm
V

21 cm

201 216 231 246   201 216 231 246
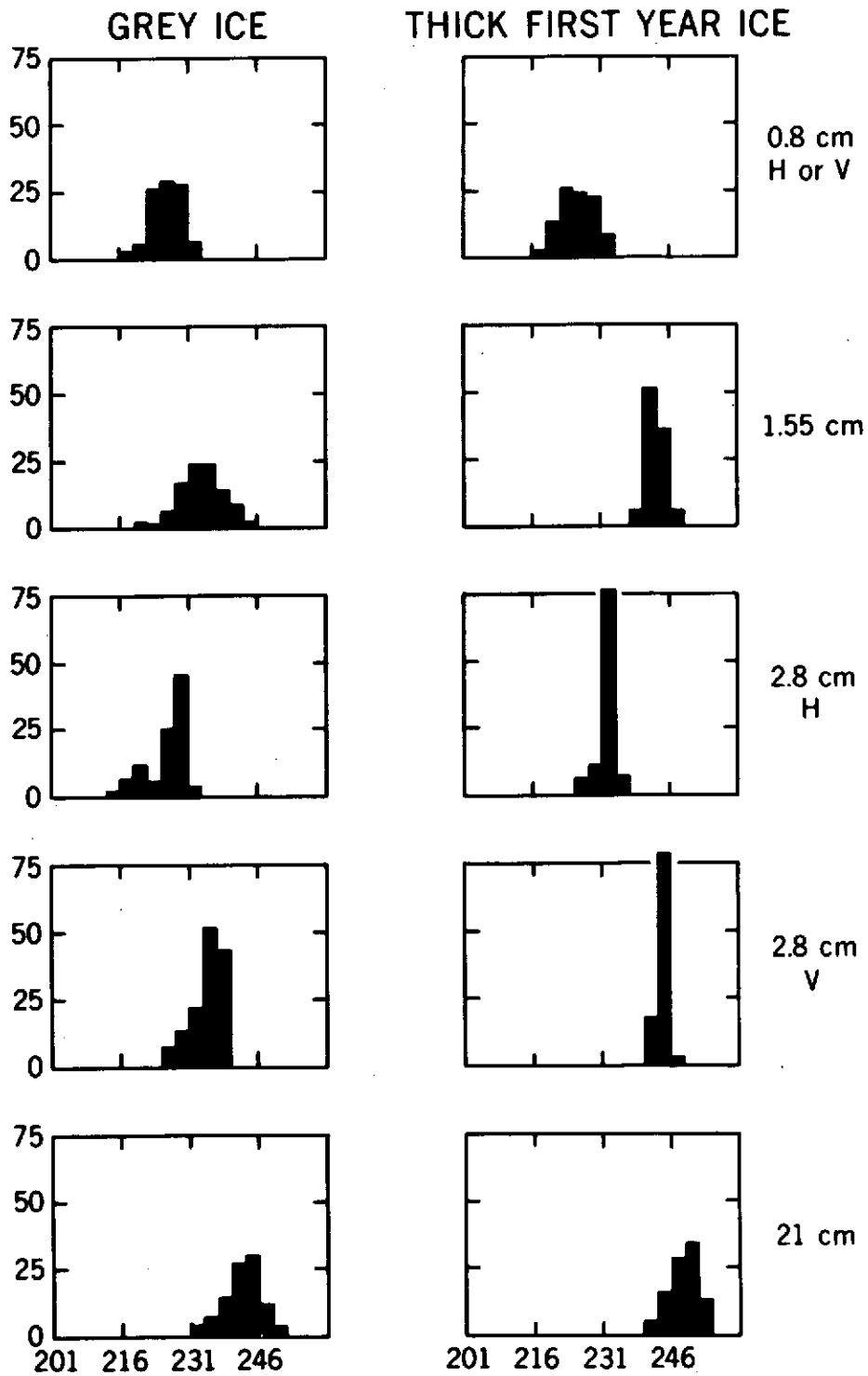
Figure 2. 22.   Histograms for different frequencies, polarizations, and ice types.   5 March 1973.

73

PAPER NO. 3

VARIATION OF ICE MORPHOLOGY OF SELECTED MESOSCALE TEST AREAS DURING THE BERING SEA EXPERIMENT

P. Gloersen*

R. Ramseier[†]

W. J. Campbell[‡]

T. C. Chang**

T. T. Wilheit*

*National Aeronautics & Space Administration, Goddard Space Flight Center, Greenbelt, Maryland 20771

[†]Department of the Environment, 562 Booth Street, Ottowa, Ontario, K1A OE7, Canada

[‡]U.S. Geological Survey, Ice Dynamics Project, Tacoma, Washington 98416

**NAS – NRC Resident Research Associate

Paper No. 3

VARIATION OF ICE MORPHOLOGY OF SELECTED MESOSCALE
TEST AREAS DURING THE BERING SEA EXPERIMENT

P. Gloersen

R. O. Ramseier

W. J. Campbell

T. C. Chang

T. T. Wilheit

ABSTRACT

In this paper, the surface and remotely obtained data for the Bering Sea Experiment sea ice missions on 15, 20, and 28 February 1973 are described. The major findings are that the sea ice consisted entirely of the first-year and younger variety and that the ice concentration varied from 74% to 90% during this period within a roughly constant geographical area, 100 km on a side.

VARIATION OF ICE MORPHOLOGY OF SELECTED MESOSCALE
TEST AREAS DURING THE BERING SEA EXPERIMENT

3.1 INTRODUCTION

In this paper, a brief summary is given of the sea ice data obtained on all four sea ice missions performed during the Bering Sea Experiment. The emphasis is on morphological changes that occurred during the period of the Experiment. The ice edge during the Bering Sea Experiment was considerably further north on the average than expected on the basis of seasonal averages. This, combined with the joint US/USSR agreement which specified the boundaries of the experimental areas based on these averages, served to restrict the geographical area covered by the sea ice missions. In fact, as is illustrated in Figure 3.1, there is considerable overlap in the four test areas in terms of geographical location. As was shown in Paper No. 1, the pack ice was extremely active during the Bering Sea Experiment with such a rapid advection of ice through the test areas that the same ice was never viewed twice in succession during the four sea ice option observations. Any morphological change that might be observed at a given geographical location, then, is not likely to pertain to a given ice sample. The data discussed here are those obtained on the surface for 15, 20, and 28 February 1973, the photomosaics obtained on 15 and 28 February 1973, and the high-altitude 1.55 cm scanning radiometer data obtained during the high altitude portion of the flights.

3.2 SURFACE-BASED MEASUREMENTS

The stations occupied during the period of 16 February to 5 March are shown in Figure 1, including the US test areas overflown on 15, 20, and 28 February and 5 March.

77

The first surface measurements for the 15 February test area were made between 0100 and 0315 GMT on 17 February. The overflight of the Convair 990 occurred between 0017 and 0147 GMT on 16 February. This is a delay of 24 hours. During this period, the stations N2 to N4 moved on the average 1 km h^{-1} southward for a total of 24 km.

The second group of surface measurements associated with the 20 February overflights consisted of stations M2, M0, M1 measured between 0135 and 0300 GMT on 21 February. The Convair 990 overflight took place between 2208 and 2339 GMT on 20 February.

The third group of stations were occupied between 2240 GMT on 27 February and 0305 GMT on 1 March. A total of 15 measurements were made as shown in Table 3.1. These measurements were made in association with the Convair 990 overflight which took place between 0018 and 0151 GMT on 1 March. For the experimental methodology the reader is referred to Paper No. 2.

3.2.1 General Station Ice Conditions

Aerial photographs and surface views were taken of a representative number of stations as shown in Figures 3.2 to 3.5. Figure 3.2 shows the stations for the test area of 15 February, in Figure 3.3 station M1 for the 20 February area is shown, and the remaining are for the 28 February mission.

Based on the general ice conditions, four groups representing similar features have been identified. The first group consisting of stations SE5 and SE6 represent a highly consolidated floe matrix. The average floe size is 25 m^2. The surface photograph of station SE5 also reveals the general morphology of individual ice floes. The small ridges represent edges of smaller ice floes which have frozen together. The amount of snow varied from 0.05 to 0.15 m.

78

The amount of grey ice between the floes is about 10%, the rest being white ice.

The second group consisting of stations SE1 to SE4, NW2, NW4, and NW5 were taken from an altitude of 300 m. The individual white ice floes are better defined and throughout the general station area grey ice patches are visible. Based on station NW4 in Figure 3.3, the average floe size is about 100 m^2. The amount of grey ice is estimated at 40%. The grey ice patches appearing in stations NW2 and NW1 in Figure 3.3, SE3 in Figure 3.4, and SE4, in Figure 3.5 comprise about 20% of the total area. The surface of the floes appears to be rough due to the consolidation of smaller floes and rafting, as seen in station SE3, Figure 3.4. Rafting as seen in station NW5 was rather extensive. It is interesting to note the faint linear structure in the grey ice on the left-hand side of the photograph as compared to the younger grey ice on the right-hand side. Much more rafting took place on the left-hand side, giving rise to miniature ridges.

The third group representing the stations of 15 February, N2 to N4, in Figure 3.2 show a highly consolidated floe structure with leads. The ice in the areas of measurement was rather uniform in appearance. The snow thickness was 0.05 m. Some grey ice is visible in the leads.

The final group consists of stations M0, M1, and M2, where M1 is shown in Figure 3.3. Only a small sector of the test area of 20 February was sampled, concentrating on the diagonal in the SE corner of the area. The floes were again highly concentrated, with a few grey ice areas visible on station M1, Figure 3.3. The white ice appeared uniform, with a 0.05 m thick snow cover on top of it. Open water was present in the form of large leads.

Overall, the ice conditions varied in terms of the amount of open water present. Grey ice areas were not as extensive, except for 28 February. The snow thickness was minimal. Ridging was very seldom encountered. One of the few examples is shown on station N4 in Figure 3.2. The ridge height is of the order of 0.80 m.

The floes, no matter how large they become, have a very interesting growth history. The first generation of floes are pancakes which form during transition from grease to thin grey ice. The size varies from 0.30 to 0.60 m in diameter. Several pancakes will then freeze together forming the first floe, which may attain dimensions of the order of 1 to 3 cm. Then floes combine further to form bigger floes varying in size up to 900 m^2. Finally, large fields of floes will form, as for example, on station N2, Figure 3.2 and SE6, Figure 3.5, but still having the basic small floe as a characteristic. The ice along and near the ice edge very often breaks up into smaller pieces, due to large swells in the sea.

3.2.2 Structural and Textural Properties

The data for representative station measurements are presented in Figures 3.6 to 3.9. The station position, dates, and other relevant data are given in Table 3.1. The explanation of how the data are presented and the meaning of the various symbols and numbers were discussed in Paper 2.

As for 5 March, three distinct ice categories emerge, with frazil ice representing the top layer. This is followed by columnar ice and in a few instances with a layer of mixed frazil and columnar ice. By examining all the core data for the cases in which a thick section was prepared, it was found that the ice at the surface always consists of frazil ice. Its thickness varies from 0.03 m to greater than 0.33 m, with an average thickness of 0.18 m. The second and most

predominant category is columnar ice. The texture and brine pocket shape have already been discussed and shown in Figure 2.16 of Paper 2.

The ice has undergone extensive rafting, as evidenced from the shape of salinity curves (Figures 3.6 to 3.9) and previously shown in Figures 3.2 to 3.5. The thinner white ice had a thickness range between 0.41 m and 0.76 m, with an average thickness of 0.62. The thick white ice varied from 0.80 m to <2 m, with an average thickness of 1.23 m, and finally the grey ice varied between 0.025 m and 0.30 m, having an average thickness of 0.18 m. This is very interesting indeed when one compares, as shown in Table 3.2, the average thickness of the three ice types for the current three areas and for the area of 5 March. Since for all practical purposes the average thicknesses are the same, in situ growth is not the primary cause for the thickening of the ice. As illustrated in Figure 3.1, the areas overlap extensively and the ice which appears in the test area is new. In other words the ice forms continuously further north, moves through the test area undergoing very heavy rafting in the process.

The amount of snow varied from 0.02 to 0.15 m in thickness, the average being 0.06 m. This is somewhat less than the amount given for 5 March. From Table 3.1 it can be seen that some slight snowfall or snow drifting must have occurred between 21 and 27 February. Because of the lack of solid precipitation, most of the snow accumulation must have come from drift snow due to the prevailing NE winds.

3.2.3 Physical and Chemical Properties

The surface salinities varied between 4.0 and 13.4 ppt. The average is 8.3 ppt. This is appreciably lower than the average of 5 March, which was 12.4 ppt. One cause of this difference is the lack of extensive hoarfrost on the grey

ice. This in itself is not surprising, due to the near freezing point temperatures which did occur on 28 February, as shown in Figure 1.12. This is also reflected by the average of the surface temperature of -6.5°C, which is 3°C higher than on 5 March. The average density for grey ice is 0.911 and for white ice 0.895 g.cm^{-3}. This compares well with the densities of 5 March.

3.3 MORPHOLOGY IN THE MESOSCALE TEST AREAS

In Figure 3.10, the 1.55 cm images obtained on 15 and 20 February over similar geographical areas are compared. The most striking contrast between the two is the distinct change in lead orientation that occurs in the central portion of each test area on those two days. The leads have a definite east-west orientation on 15 February, whereas there is more of a north-south orientation on 20 February. The ice concentration is 74% and 84% for the 15 and 20 February respectively.

It is evident that the fully consolidated sea ice has a uniform signature at a wavelength of 1.55 cm as long as the field of view of the radiometer is filled with first-year ice. No lower brightness temperature patterns appear on either day that would definitely indicate the presence of multiyear sea ice. The rationale for these determinations has been discussed in Paper No. 2 and will not be repeated here.

The photomosaic for 15 February is shown in Figure 3.11. The cloud cover on 20 February was too great to permit obtaining a similar photomosaic for that day. As in the case for the 5 March photomosaic described in Paper No. 2, the one shown here gives essentially the same information as the microwave image. Part of this photomosaic is obscured by clouds, especially over almost all of the entire second strip from the west. Because of the haze, it is difficult to tell

whether the polynyas appearing in the northern half of the westernmost strip are open or refrozen. The fact that they were open is confirmed upon examination of the digital data from the 1.55 cm radiometer.

The 1.55 cm microwave mosaic from 28 February and 5 March are shown in Figure 3.12. The mosaic for 28 February was prepared from individual strip records of the 1.55 cm data, since the computer-processed mosaic was not available at the time of this writing. In this representation of the data, no limb darkening correction has been applied to the data to remove the angular dependence of the surface emissivity, as was done for the computer-processed mosaics. As a result, the edges of the aircraft track tend to be at lower temperatures than the center for the 28 February mosaic. It is immediately evident that the sea ice was much more compact in the test area on 28 February than on any of the other three ice option days. The large grey ice feature discussed in the previous paper, which appears in the center of the image for 5 March, is not present in any of the earlier images. This was because the ice advected into the observation area was not imaged earlier, as was shown in the first paper. Again, there is no evidence of multiyear ice on these two test days.

For the sake of completeness, the photomosaic for 28 February is presented in Figure 3.13. Note again the similarity between the microwave and photographic images for that date.

In order to test their utility in analyses of ice morphology on a mesoscale basis, histograms of the observed 1.55 cm brightness temperatures for the sea ice missions were prepared and are illustrated in Figure 3.14. In each case, all of the 1.55 cm data, with limb darkening correction applied, were tabulated for the entire test area. As in the case for the various sectors of the 5 March test

area discussed in Paper No. 2, the distributions tend to be sharper with a peak at higher brightness temperatures when the ice is more concentrated. An estimate of the average concentration of the ice for each of the four sea ice missions is given in Table 3.3. The estimates are based on a linear interpolation between 130°K for the brightness temperature of completely open water and 260°K for the brightness temperature of 100% ice concentration. The temperature at the peak of each histogram was used for the determination. In this determination, grey ice features, the largest of which occurred in the center of the 5 March US test zone, appear to comprise less than 5% of the total test areas, and so should have only a small effect on the accuracy of the inferred ice concentration.

3.4 SUMMARY

The sea ice encountered during the Bering Sea Experiment was found to consist entirely of first-year and younger ice. The 5 March test area was the only one in which large areas of grey ice with a wet film on the surface was encountered. Considerable variation of the ice concentration in the geographical area of the experiments was found to occur.

ACKNOWLEDGMENT

Table 3.1

	Date	Time	Latitude	Longitude	Ice Thickness h_I, m	Frazil Ice Thickness h_F, m	Snow Depth h_s, m	Surface Salinity S, o/oo	Surface Temperature θ, -°C	Surface Density ρ_i, g.cm^{-3}
Option Sea Ice 15 February										
N2	17 Feb	0100	61°31' N	176°06' W	0.58	<0.33	0.05	9.8	—	—
N2G		0100	61°31' N	176°06' W	0.30	0.30	0.025	10.1	—	0.920
N3		0235	61°50.3'N	176°05' W	0.76	0.03	0.06	10.0	8.6	0.900
N4		0315	62°10' N	176°05' W	0.49	<0.32	0.04	7.8	7.7	0.895
Option Sea Ice 20 February										
M2G	21 Feb	0135	61°20.5'N	176°15' W	0.14	—	0	—	8.0	—
M0		0210	60°58' N	175°37' W	1.05	—	0.05	7.2	10.4	0.874
M1		0300	61°10.5'N	175°58' W	0.99	0.03	0.045	6.0	10.6	0.918
M1G		0300	61°10.5'N	175°58' W	0.30	0.10	0.01	10.3	10.3	0.904
Option Sea Ice 28 February										
NW2	27 Feb	2240	61°29.5'N	174°58' W	0.41	0.36	0.02	11.2	4.4	0.877
NW5	28 Feb	0320	62°14.8'N	176°25.5'W	0.65	0.18	0	5.1	4.3	0.891
NW5G		0320	62°14.8'N	176°25.5'W	0.08	—	0	13.4	5.2	—
NW4		0415	61°59' N	175°56.2'W	0.69	—	0.065	9.3	4.6	0.903
SE0		1850	62°13.1'N	176°29' W	0.87	0.03	0.07	7.0	6.1	—
SE1		2035	62°06' N	176°15.5'W	0.74	0.18	0.06	9.2	6.4	0.891
SE1G		2035	62°06' N	176°15.5'W	0.14	0.14	0	12.8	8.0	0.916
SE2		2110	61°59' N	175°58.8'W	0.80	0.09	0.08	4.2	5.1	0.890
SE2G		2110	61°59' N	175°58.8'W	0.18	0.08	0	9.2	5.8	0.903
SE3		2200	61°52' N	175°44.9'W	1.40	0.37	0.07	6.5	6.0	0.900
SE3G		2200	61°52' N	175°44.9'W	0.025	0.025	0	—	—	—
SE4		2218	61°44.1'N	175°28' W	1.85	0.11	0.08	4.9	5.8	—
SE4G		2218	61°44.1'N	175°28' W	0.19	—	0	9.3	2.2	—
SE5	1 Mar	0235	61°31' N	176°20.2'W	<2	0.15	0.05	4.0	5.5	—
SE6		0305	61°26.1'N	176°09.2'W	0.87	0.07	0.15	7.1	5.8	—

Table 3.2

Average Ice Thickness as Compared to 5 March

	15, 20, 28 February h_I, m	5 March h_I, m
Grey Ice	0.18	0.17
Thin White Ice	0.62	0.59
Thick White Ice	1.23	1.18
Snow Depth	0.06	0.09

Table 3.3

Average Ice Concentration in Mesoscale Test Areas

Date	Concentration (%)
15 February	74
20 February	84
28 February	90
5 March	82
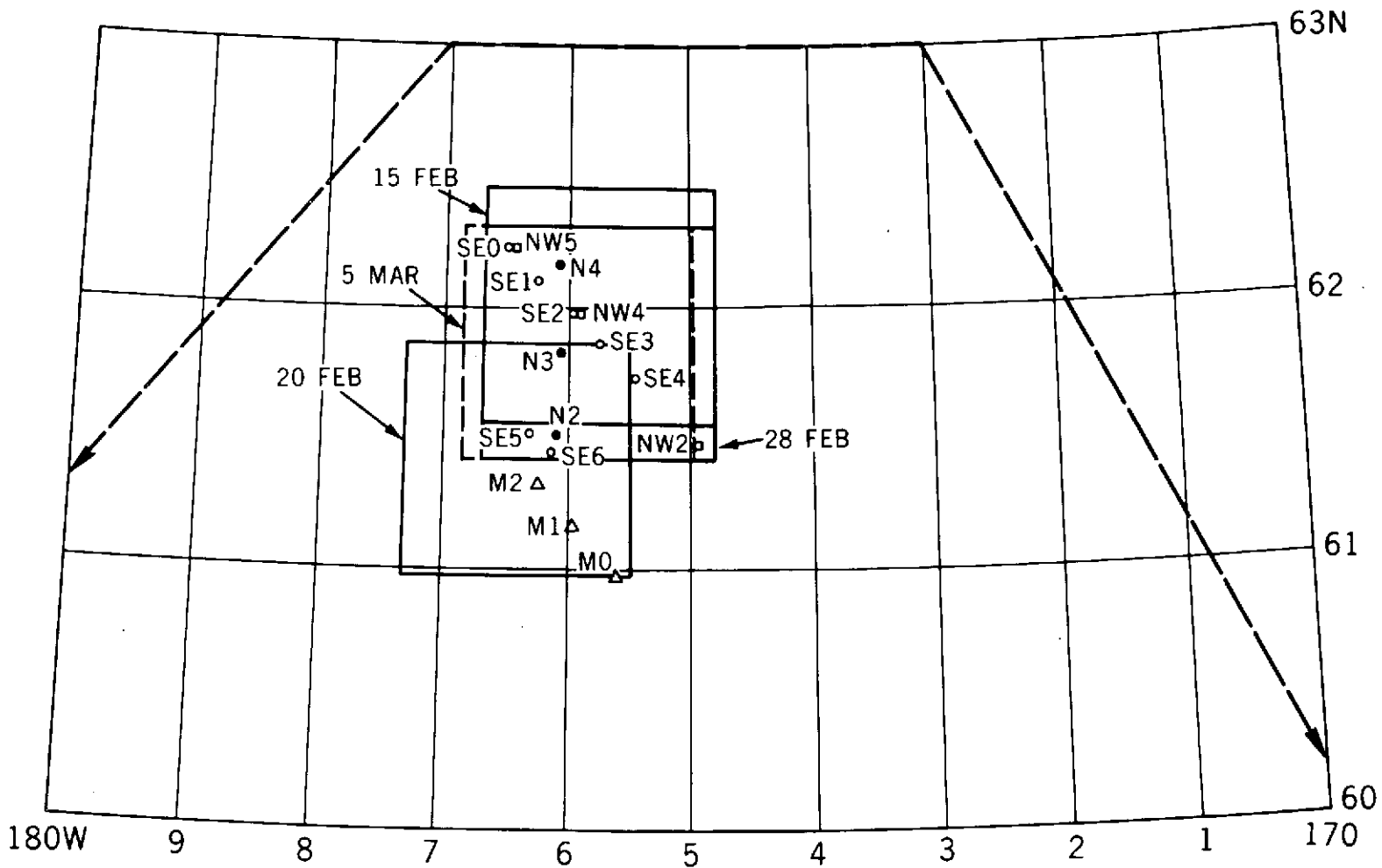
Figure 3.1. Geographical location of the four sea ice mission test areas, showing the location of the surface data test points (see Figures 2.6-2.15, 3.6-3.9, and Tables 2.1 and 3.1).
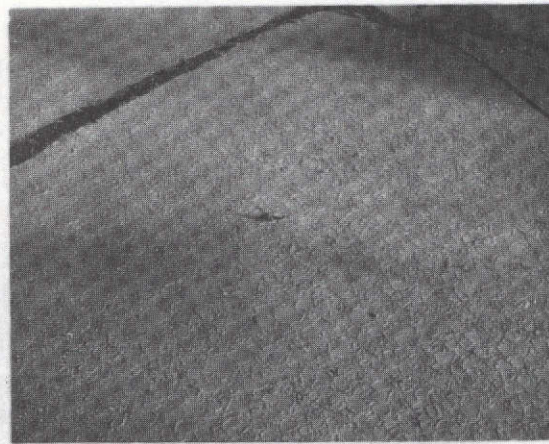
STATION N2
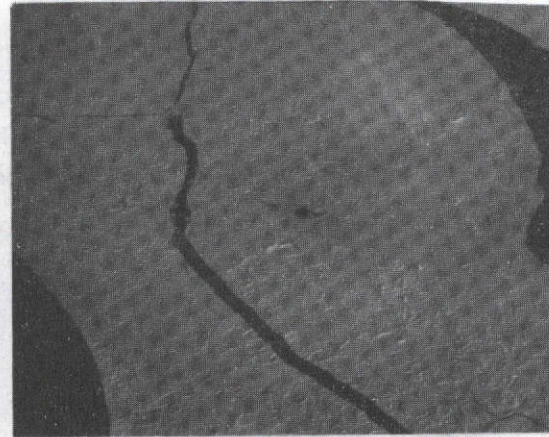
STATION N3

STATION N3 (IN SITU)
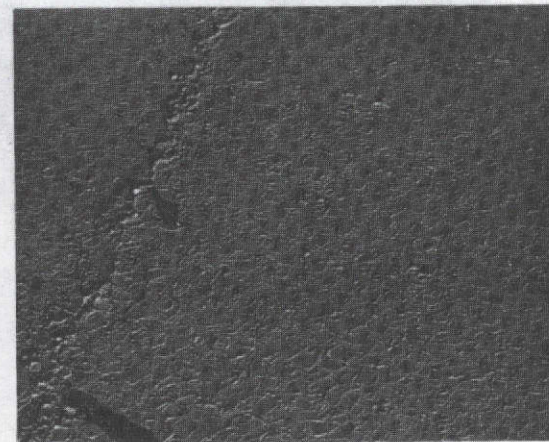
STATION N4

Figure 3.2. Aerial and in situ views of surface test points N2, 3, and 4. The aerial views were taken from the primary service helicopter. The comparison helicopter can be seen near the locations at which the surface measurements were made.
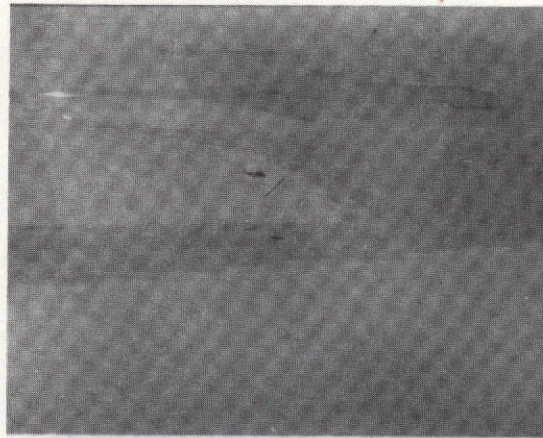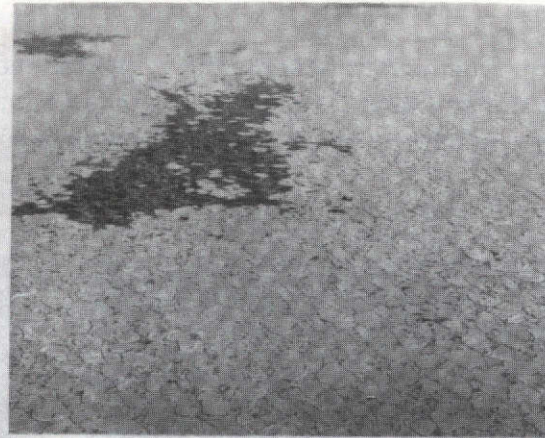
STATION M1 **STATION NW2**
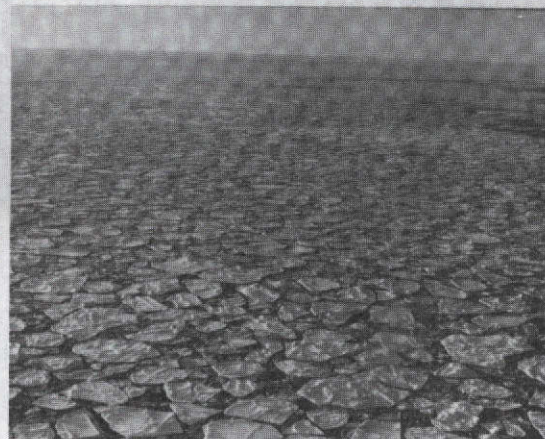
STATION NW5 **STATION NW4**

Figure 3.3. Aerial and in situ views of surface test points M1, NW2, 4, and 5. The aerial views were taken from the primary service helicopter. The companion helicopter can be seen near the locations at which the surface measurements were made.
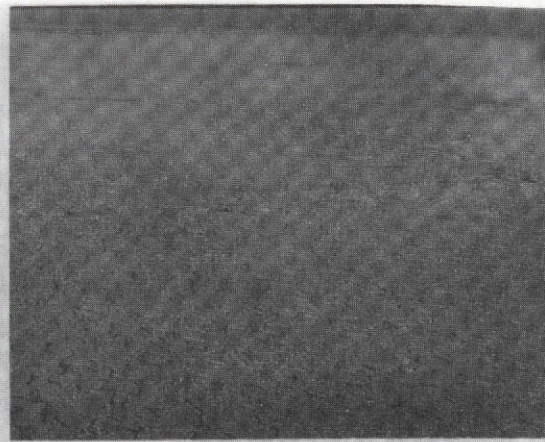
STATION SEI
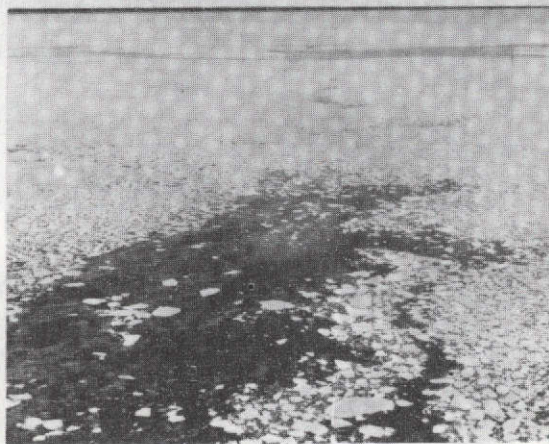
STATION SE2

STATION SE3
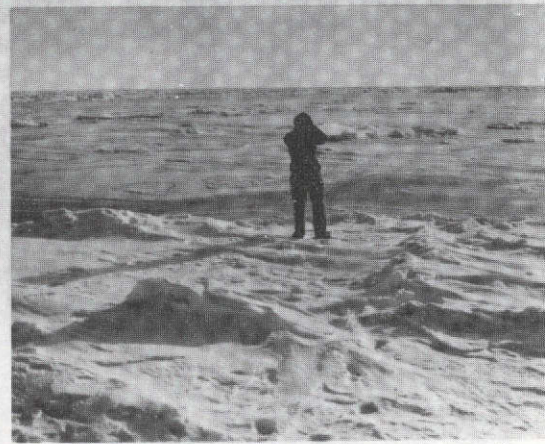
STATION SE3 (IN SITU)

Figure 3.4. Aerial and in situ views of surface test points SE1, SE2, and SE3. The aerial views were taken from the primary service helicopter. The companion helicopter can be seen near the locations at which the surface measurements were made.
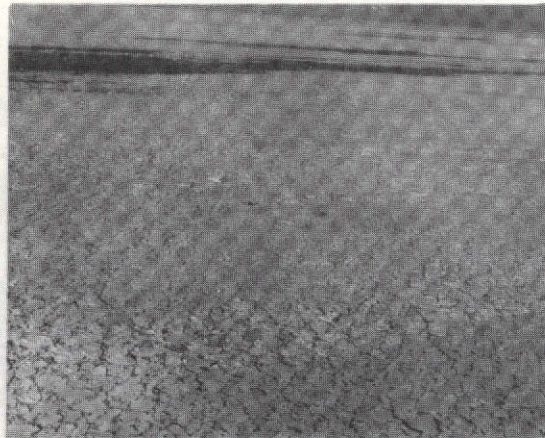
STATION SE4

STATION SE5 (IN SITU)
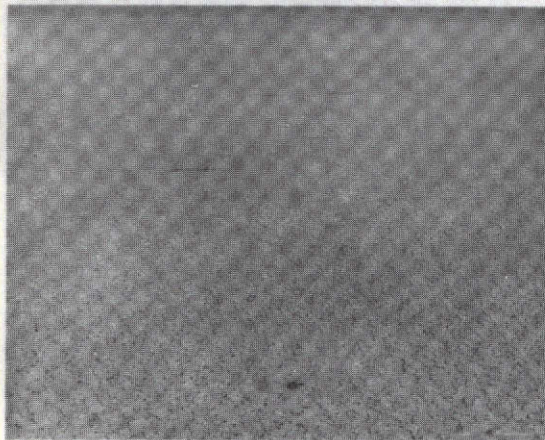
STATION SE6

STATION SE6 (IN SITU)

Figure 3.5. Aerial and in situ views of surface test points SE4, SE5, and SE6. The aerial views were taken from the primary service helicopter. The companion helicopter can be seen near the locations at which the surface measurements were made.
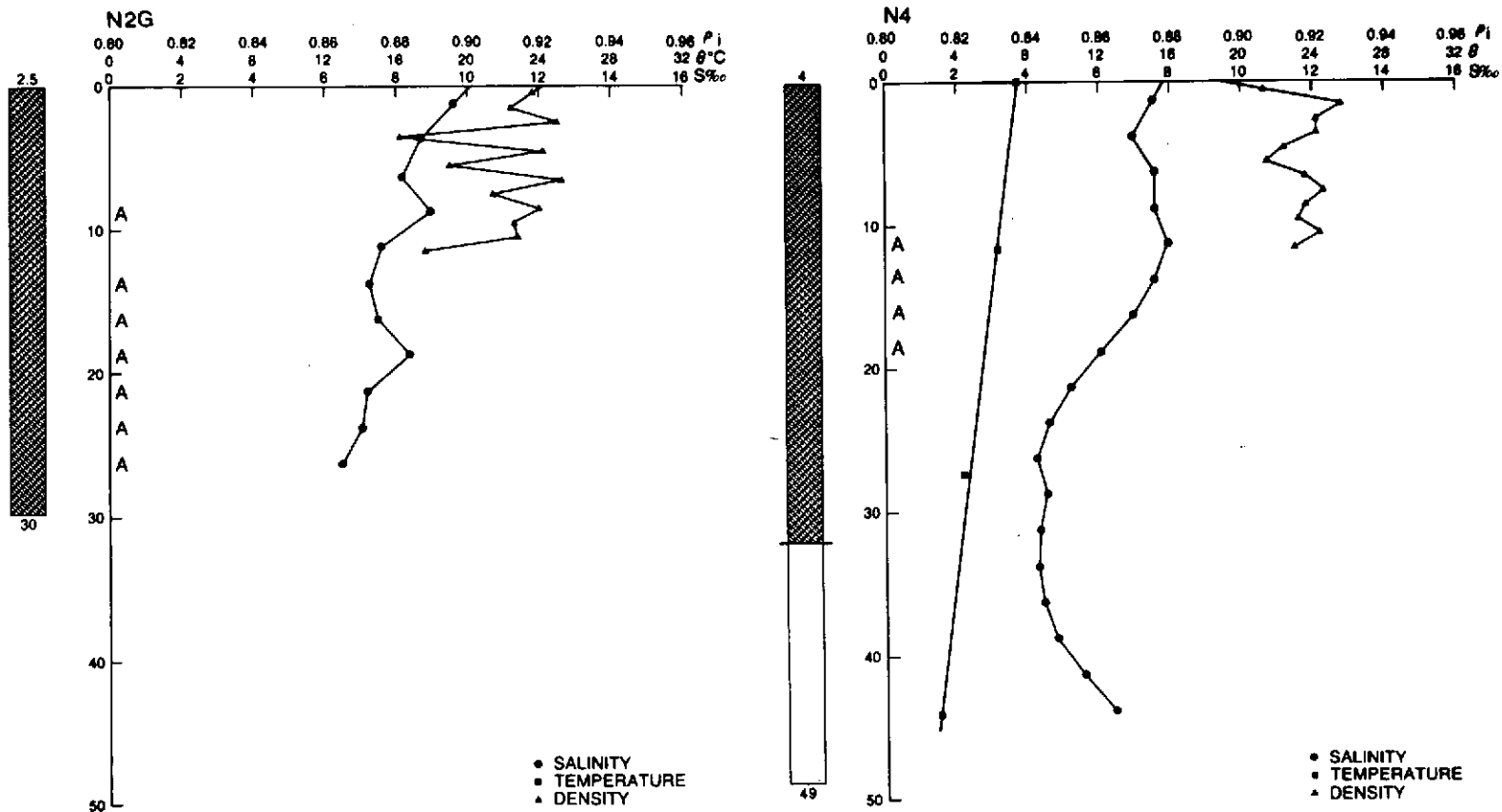
SURFACE TRUTH DATA FOR USA "C" OPTION AREA STATIONS N2G AND N4 (15 FEB.)

Figure 3.6. Salinity, temperature, and density profiles for surface test points N2G and N4. The types of ice are indicated by various cross-hatchings, explained in Paper 2.
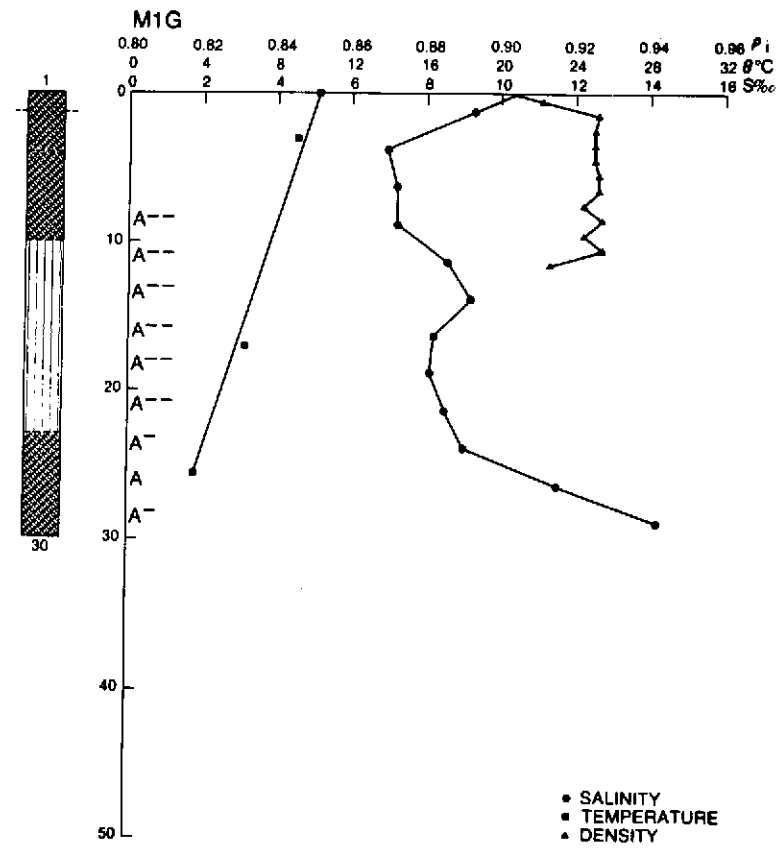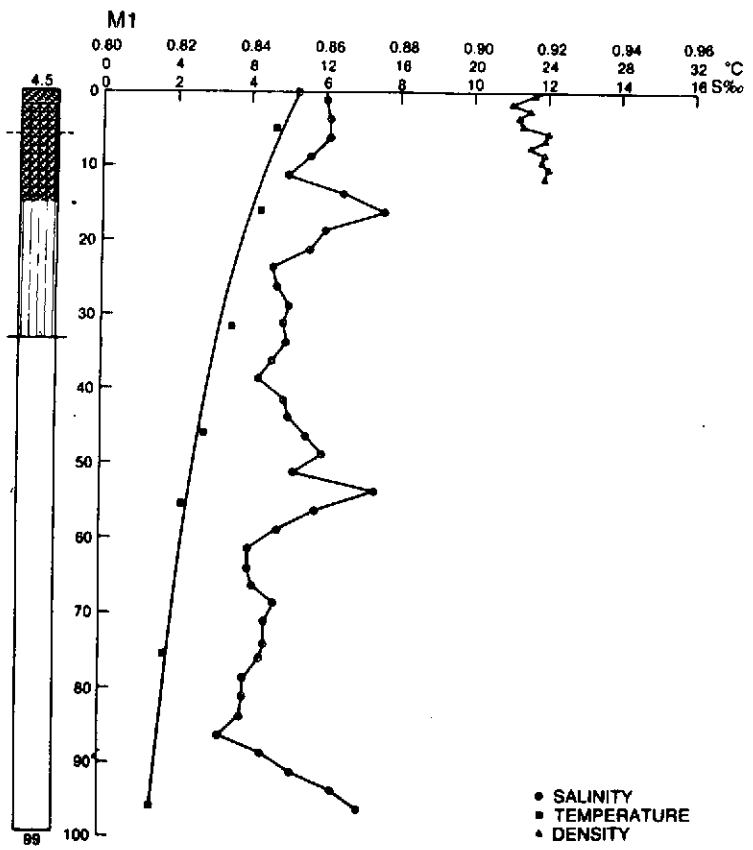
SURFACE TRUTH DATA FOR USA "C" OPTION AREA STATIONS M1 AND M1G (20 FEB.)

Figure 3. 7.   Salinity, temperature, and density profiles for surface test points M1 and M1G.
The types of ice are indicated by various cross-hatchings, explained in Paper 2.

SURFACE TRUTH DATA FOR USA "C" OPTION AREA STATIONS NW2 AND NW5 (15 FEB.)

Figure 3.8. Salinity, temperature, and density profiles for surface test points NW2 and NW5. The types of ice are indicated by various cross-hatchings, explained in Paper 2.
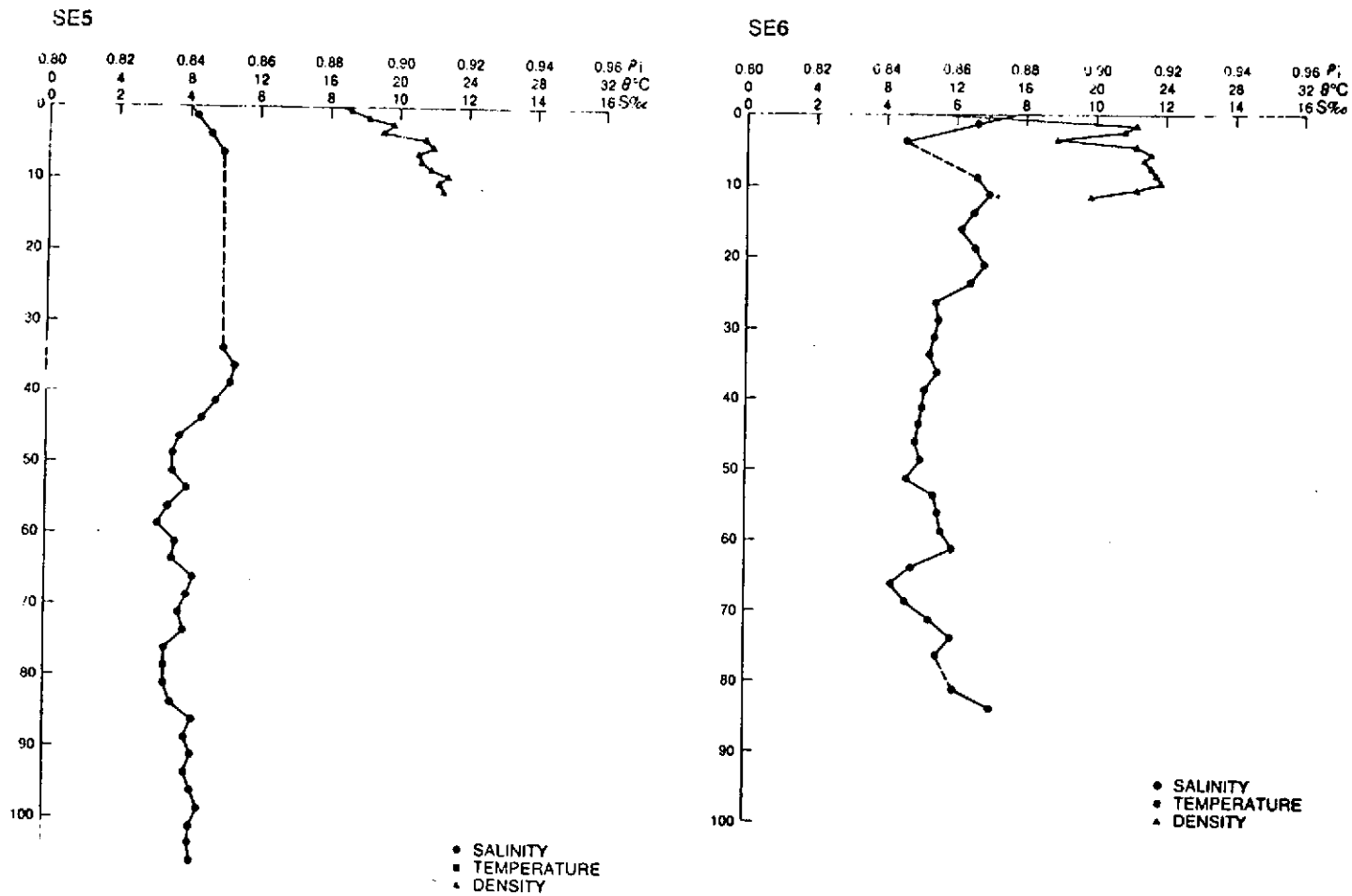
Figure 3.9. Salinity, temperature, and density profiles for surface test points SE5 and SE6. The types of ice are indicated by various cross-hatchings, explained in Paper 2.

1.55 cm MICROWAVE IMAGES
BERING SEA EXPERIMENT

N
↑
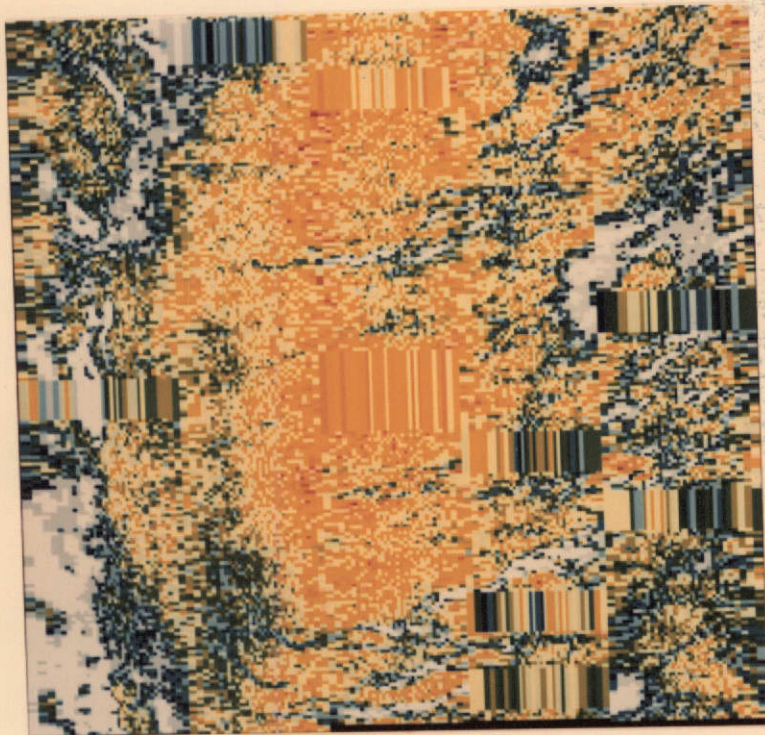
15 FEBRUARY 1973
CENTER NEAR 62.0°N, 175.7°W
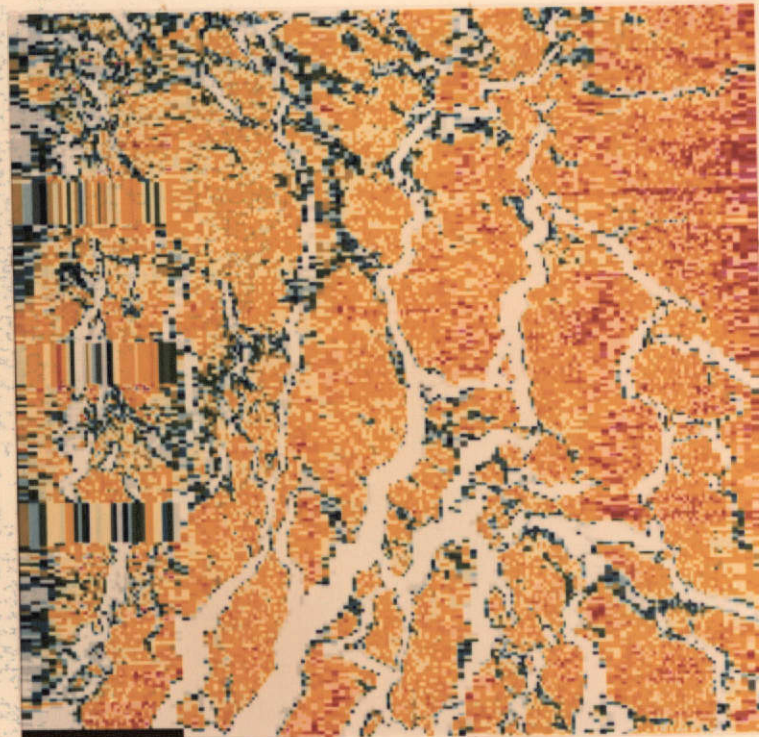
20 FEBRUARY 1973
CENTER NEAR 61.4°N, 176.4°W

AREA: 100 Km x 100 Km

7262K	251	247	243	239	235	231	227	223	211	
253	249	245	241	237	233	229	225	221	<210K	

AREA: 100 Km x 100 Km
CENTER NEAR 61.9°N, 175.7°W

N ←

Figure 3.11. Photomosaic of the 15 February sea ice test area. The gaps between the strips resulted from the differing fields-of-view of the camera and the 1.55 cm imager.

1.55 cm MICROWAVE IMAGES
BERING SEA EXPERIMENT

N
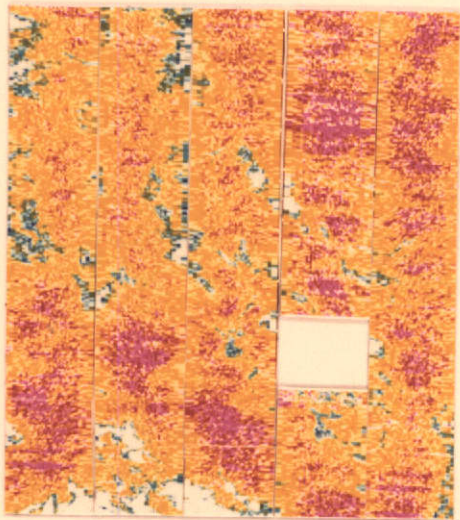
28 FEBRUARY 1973
CENTER NEAR 61.9°N, 175.7°W
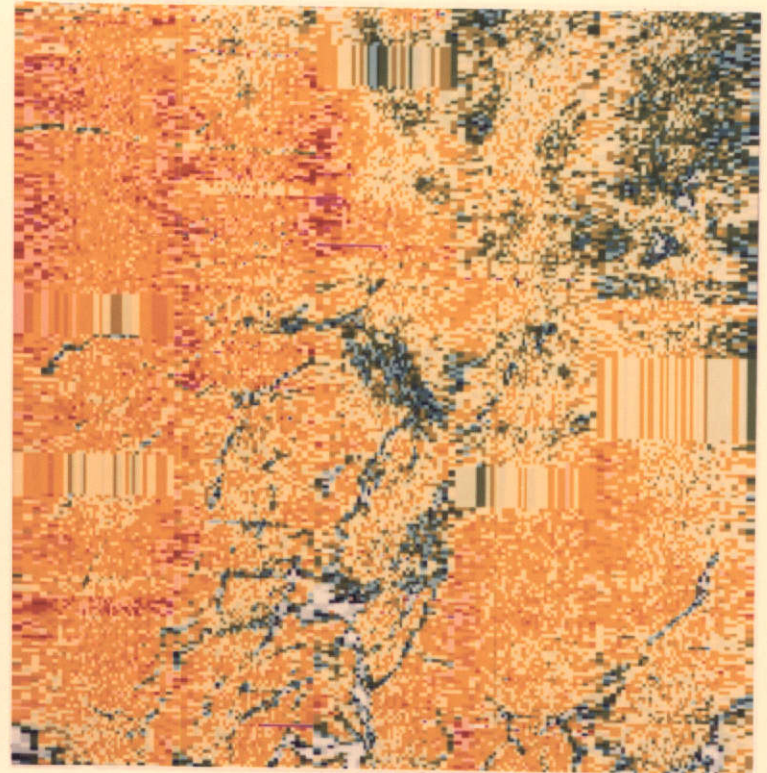
5 MARCH 1973
CENTER NEAR 61.9°N, 175.9°W

AREA: 100 Km × 100 Km

7262K	251	247	243	239	235	231	227	223	211
253	249	245	241	237	233	229	225	221	<210K
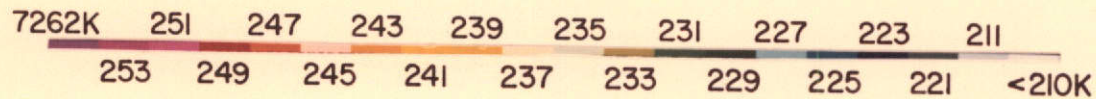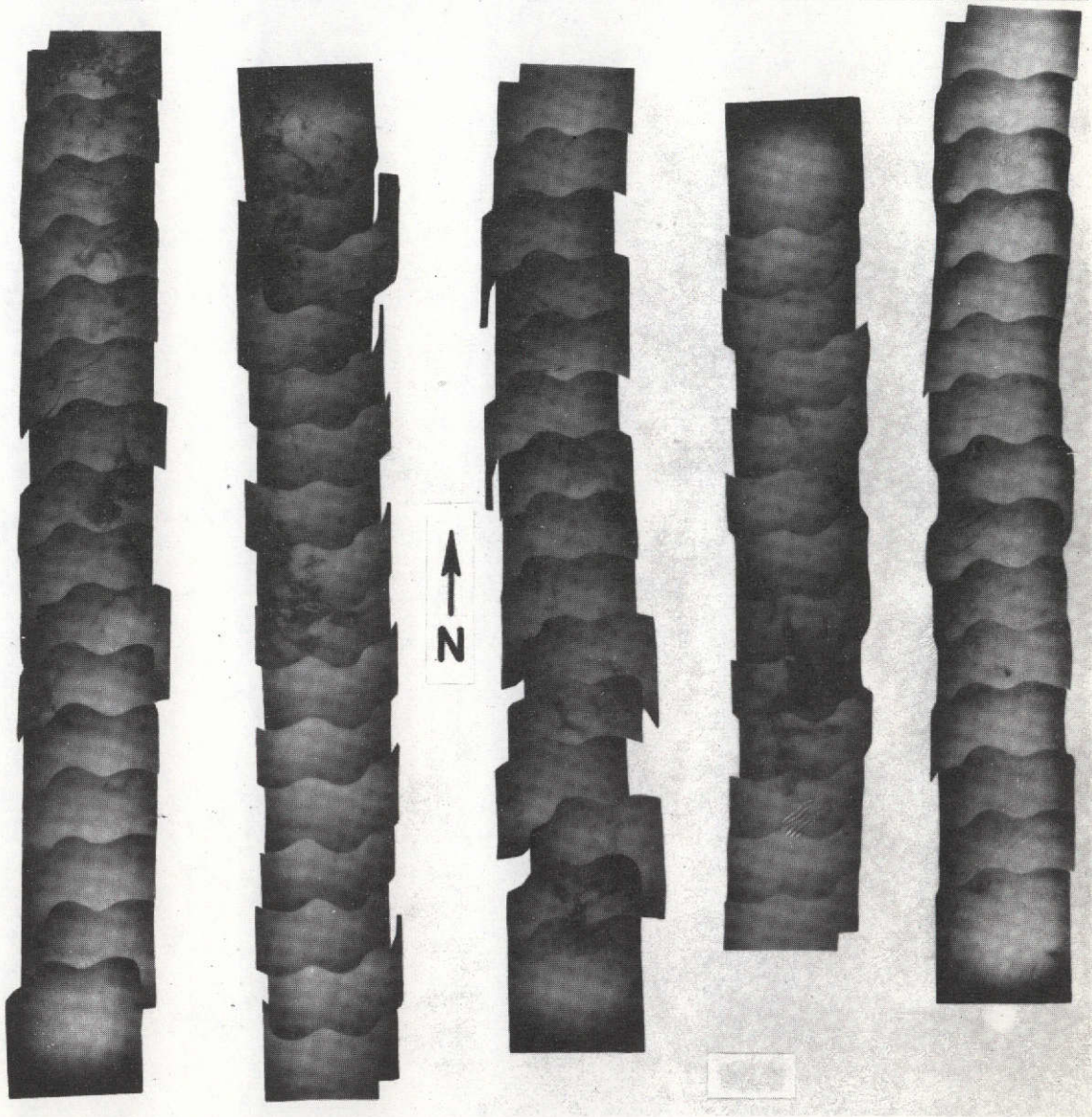
28 FEBRUARY 1973

AREA: 100 Km x 100 Km
CENTER NEAR 61.9°N, 175.7°W

Figure 3.13. Photomosaic of the 28 February Test Area
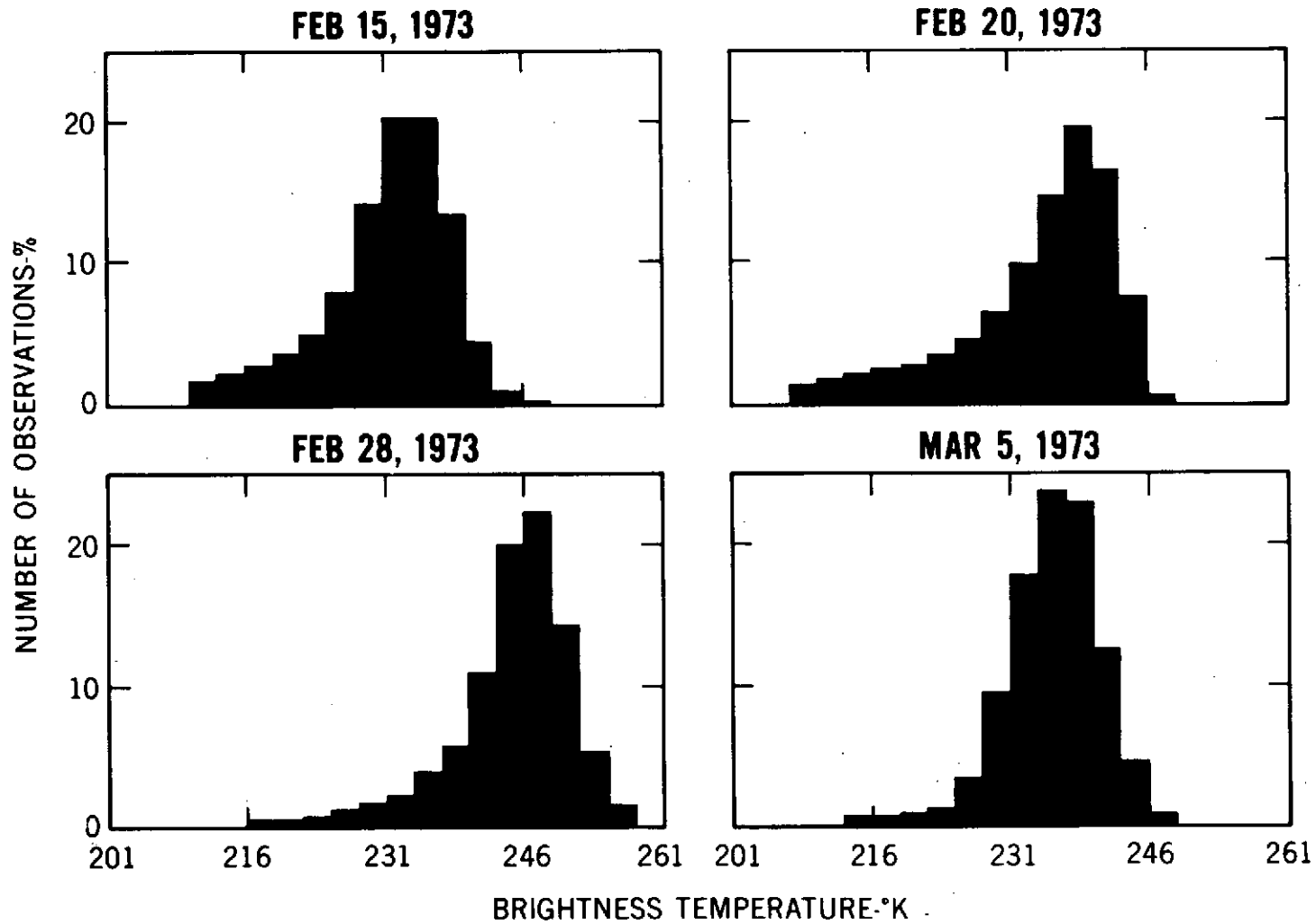
Figure 3.14. Histograms of the 1.55 cm Brightness Temperatures Observed Over the Entire U.S. Test Areas During the Four Sea Ice Missions

PAPER NO. 4

ICE THICKNESS DISTRIBUTION AS INFERRED FROM

INFRARED AND MICROWAVE REMOTE SENSING DURING

THE BERING SEA EXPERIMENT

P. Gloersen[*]

R. Ramseier[†]

W. J. Campbell[‡]

P. M. Kuhn[**]

W. J. Webster, Jr.[*]

[*]National Aeronautics & Space Administration, Goddard Space Flight
Center, Greenbelt, Maryland 20771

[†]Department of the Environment, 562 Booth Street, Ottawa, Ontario,
K1A OE7, Canada

[‡]U.S. Geological Survey, Ice Dynamics Project, Tacoma, Washington
98416

[**]U.S. Department of Commerce, National Oceanic and Atmospheric
Administration, Environmental Research Laboratories, Boulder,
Colorado 80302

Paper No. 4

ICE THICKNESS DISTRIBUTION AS INFERRED FROM INFRARED AND MICROWAVE REMOTE SENSING DURING THE BERING SEA EXPERIMENT

P. Gloersen

R. O. Ramseier

W. J. Campbell

P. M. Kuhn

W. J. Webster, Jr.

ABSTRACT

Remote sensing of the sea ice surface at wavelengths of 10 micrometers and 21 cm is investigated for the purpose of determining the feasibility of obtaining ice thickness from the radiometric measurements. Distinguishable radiometric signatures were obtained for thin ice at 21 cm, but the signatures do not follow a simple model consisting of a thin sheet of sea ice with parallel faces separating the ocean from the atmosphere. In fact, the signatures are distinguishable for ice thicknesses an order of magnitude larger than predicted on the basis of this simple model. It is speculated that the microwave signature pertains only to either the freeboard portion of the sea ice or the frazil layer. At 10 micrometers, the observations appear to fit the theoretical predictions rather well. The model consists of heat transfer from the ocean to the turbulent portion of the atmosphere through two layers, a slab of ice in which the heat transfer rate varies with temperature and the temperature varies with vertical position in the slab, and a

nonturbulent boundary layer in the atmosphere directly above the ice in which the major heat transport is convective. Major difficulties in using infrared remote sensing for sea ice thickness determinations are found to be obscuration of the sea ice surface by ground haze and obtaining reliable values for the air temperature at the bottom of the turbulent atmosphere.

ICE THICKNESS DISTRIBUTION AS INFERRED FROM INFRARED AND MICROWAVE REMOTE SENSING DURING THE BERING SEA EXPERIMENT

4.1 INTRODUCTION

One of the most tantalizing of all objectives in remote sensing of sea ice is the possibility of determining the thickness of the ice. A number of investigators (Adey, 1971; Gloersen, et al. 1972) have observed microwave signatures of sea ice at long wavelengths that seemingly could be explained no other way than by assuming that the microwave radiometer was able to discern the sea surface through the sea ice. Unfortunately, no concurrent surface measurements were available to establish the actual sea ice thicknesses. Laboratory measurements of the complex dielectric constant (Hoekstra, 1971) and a simple layered dielectric model set the sensitivity of such determinations of sea ice thickness at about 1/10 of a wavelength of the microwave radiation.

Another method for determining sea ice thickness that has been suggested (Ketchum, 1968) is based on measuring the surface temperature remotely by means of an infrared radiometer. The basis for this determination is that the sea ice layer is the main limitation for the transfer of thermal energy from the sea to the atmosphere in the Arctic environment. The rate of this transfer, then, depends on the thickness of the sea ice layer, and the surface temperature will vary accordingly. There are many difficulties associated with this sort of sea ice thickness determination, such as the variability with local weather conditions (ground haze, cloud cover, and surface winds) and the structure of the sea ice cover (snow cover, thickness, and ice concentration).

106

During the Bering Sea Experiment, we encountered a number of samples
of thin sea ice with the infrared and 21 cm microwave radiometers which were
also measured by the surface observations team. The results of those observa-
tions are reported here.

4.2 THE MICROWAVE MODEL FOR ICE THICKNESS DETERMINATIONS

A simple three-layer dielectric model has been used to demonstrate the
sensitivity of microwave radiometry for the determination of sea ice thickness.
The microwave wavelength chosen for this study was 15 cm, but the results are
not very sensitive to wavelength and have therefore been represented in dimen-
sionless terms. The following values (Table 4.1) have been assumed for dielec-
tric constants of the three layers (Hoekstra, 1971). The computed emissivity
of these three layers is shown in Figure 4.1. It can be seen that the results are
remarkably uniform for the cases considered. The higher the imaginary part
of the dielectric constant, the higher the surface reflectivity becomes, resulting
in a decrease in the peak emissivity as the ice layer thickness increases. The
oscillations in the emissivity (due to interference between the top and bottom of
the ice) become more pronounced as the imaginary part of the dielectric constant
becomes smaller, as one might expect. These results can now be qualitatively
extended to sea ice with other values of salinity, keeping in mind that the imagi-
nary part of the dielectric constant varies directly with salinity. In all cases
(Figure 4.1) the maximum emissivity is first reached at an ice thickness of
about 0.17 wavelengths in air (or 1/4 wavelength in the medium). This model
implies that the limit of sensitivity of determination of ice thickness from
microwave brightness temperature is not much more than 1/6 of a wavelength
(in air) of ice thickness for a wide variety of salinities and sea ice temperatures.

4.3 THE INFRARED MODEL FOR SEA ICE THICKNESS DETERMINATION

A two-layer model is used here to predict the surface temperature of thin sea ice. The heat transfer is assumed to take place between the ocean at 271°K and the turbulent atmosphere through a layer of sea ice in which: 1) the ice conductivity varies with temperature, 2) the ice temperature varies vertically within the slab, and through a non-turbulent atmospheric boundary layer above the slab in which the major heat transport is convective. Heat transfer through such layers has been treated in textbooks (e.g. Jakob, 1949) and will not be repeated here. The heat transfer through sea ice has been measured (Schwerdtfeger, 1963) and found to vary inversely with the temperature in the medium. The constants measured for a salinity of 8 ppt have been incorporated in the following expression for the sea ice thickness:

$$\Delta Z_{ice} = \frac{k_{air} \left[4.54 \times 10^{-3} (271.5 - T_{ice}) - 1.89 \times 10^{-4} \ln (272.5 - T_{ice}) \right] T_{air}^{1/4}}{(T_{ice} - T_{air})^{5/4}}$$

$$(4.1)$$

where k_{air} is a constant containing such factors as the thickness of the convective boundary layer, the constant term in the thermal conductivity of the air, and the viscosity of air; T_{ice} is the surface temperature (measured with the infrared radiometer); and T_{air} is the temperature at the top of the convective boundary layer. The objective of this analysis was to provide a reasonable functional form for ΔZ_{ice}, rather than attempt to obtain a quantitative prediction. Thus k_{air} was determined by curve-fitting to the experimental points.

4.4 OBSERVATIONS

As a result of the aircraft navigational system malfunction on the 5 March flight and the corresponding lack of coincidence of the low pass aircraft track

and the test points along the diagonal crossing the US test area, it is necessary to assume that the properties of the grey ice actually transversed by the aircraft are essentially the same as those for surface test point A3G on that date. This assumption is reasonable, since the grey leads were probably opened at about the same time, and the freezing rates are quite comparable over a large area. The data from the 20 and 28 February flights are in better coincidence, but the processing on the 28 February flight has not been completed since it was not included in the initially agreed exchange. The salinity and density profiles obtained on 5 March for the grey ice at A3G are typical of similar data taken on grey ice on other dates.

The surface data for A3G taken on 5 March are shown in Figure 4.2, illustrating both the aerial view of the test site and the physical data from the surface measurements of the grey ice. From this Figure, it can be seen that the salinity is approximately 8 ppt through most of the grey ice sample, which is the value used to develop Equation 4.1. This was also the case for the samples taken at test points M2G on 20 February and SE2G on 28 February. For reasons discussed in Paper 2, the salinity in the top few centimeters of the ice becomes very high; the thermal conductivity should drop correspondingly, but this has been neglected in this analysis since this layer is a small part of the total ice cover.

The infrared and microwave radiometer data acquired on the low-level passes on 20 February and 5 March are shown in Figures 4.3 and 4.4, where some of the points selected for this study are indicated. For the most part, the sharp spikes that occur result from open water in the leads. Some notable exceptions to this appear to occur early in the low altitude pass. The double spikes that occur at about 23h 28m 57s (Figure 4.4) decrease in amplitude as wavelength

decreases, indicative of a thin ice signature. The fact that the spikes do not disappear at the shorter wavelengths may be attributable to the wet surface phenomenon described in Paper 2. The next sharp spike, appearing at about 23h 30m 00s, does decrease in amplitude more rapidly with wavelength, perhaps indicating a drier surface condition. It is interesting to note that the 10 micrometer infrared data (top of Figure 4.4) do not indicate open water in these leads, since the temperature recorded was less than 271°K. An example of a fully-resolved open lead feature occurs near 23h 32m 22s (Lead 2, Figure 4.4), where the spike occurs at all wavelengths, and the infrared radiometer reads 271°K. An example of the wet-surface grey ice feature described earlier appears near 23h 40m 44s. Since this relatively wide feature seems to increase with a decrease in wavelength and does not appear at all at long wavelengths, one might infer that this particular grey ice area is relatively thick.

Two of the features observed on 5 March (Leads 2 & 3, Figure 4.4 and Table 4.2) are depicted as 10 micrometer infrared images in Figure 4.5 The temperatures indicated in Figure 4.5 are generally close to the actual values since the atmospheric contributions are small from that altitude, except when ground haze is encountered. Open water can be seen in part of Lead 2, but most of the ice in the lead appears to be uniform in thickness, as evidenced by the uniform surface temperature.

The 21 cm radiometer signal for the entire low-level passes on 20 February and 5 March, illustrated in Figures 4.3 and 4.4, were also recorded digitally and integrated for one second, so that two to three readings were obtained for each grey ice feature. Of course, there were many more readings for thick

white ice. The averages of the digital data for each test point are listed in Table 4.2.

On 20 February an interesting feature was encountered with the aircraft on which surface measurements were also taken, corresponding to M2G (see Figure 3.1 and Table 3.1). In this case, the drop in brightness temperature decrease: with wavelength. The data are listed in Table 4.2, and entered also in Figure 4.1 for comparison with the analysis.

4.5 DISCUSSION

The data for point SE1 were used to determine the constant k_{air} in Equation 4.1. T_{ice} for this point was obtained while at low-level from the non-scanning 10 micrometer radiometer. T_{air} for all points was obtained from Staten Island records and verified by measurements from the helicopters. The equation is plotted in Figure 4.6 using this value of k_{air} and several values of T_{air}, along with other experimental data obtained during the low-level data flight. The proximity of the points to the appropriate air temperature curves is remarkably good particularly at lower values of ice thickness, ΔZ, when varying weather and surface conditions are taken into account. Some of the scatter of the experimental points might be accounted for by variation in the intervening ground haze, which would tend to lower the infrared radiometer reading. As a matter of fact, the haze on 20 February was sufficient to preclude producing a photomosaic from the high altitude photography. It is interesting that the points on Figure 4.6 (labeled 260) corresponding to data taken on 20 February show the poorest agreement with the curves.

The 21 cm emissivities determined from the data taken near test points M2G and SE1G, listed in Table 4.2, are plotted in Figure 4.1 as a function of the

111

ice thickness/wavelength ratio also determined from the Table 4.2 data. It is immediately apparent that our model for predicting the brightness temperature at 21 cm of sea ice for various thickness is grossly incorrect. We are led to conclude that something other than the semitransparency of thin ice to microwave radiation, as expressed in the curves of Figure 4.1, must be responsible for the observed variation in brightness temperature. The wet-surface phenomenon discussed in Paper 2 for 1.55 cm radiation also does not appear to fit the 21 cm observations in a consistent way. We are left, for the present time, with the unexplained observation that thin first-year ice (less than 0.20 m) tends to have lower brightness temperatures than thicker first-year ice, but the thickness scale involved does not fit any model at hand. Possibly the signatures are related to only the freeboard portion or the frazil ice portion of the thin sea ice; the thicknesses of these layers more closely fit the 1/6 wave thickness requirement of the simple model discussed earlier.

The data from 5 March (Leads 2 and 3) were not plotted on Figure 4.1 since they apparently do display the wet-surface phenomenon discussed in Paper 2.

REFERENCES

Adey, A. W., "Theory and field tests of a microwave radiometer for determining sea ice thickness," Proc. #90, NATO Advisory Group for Aerospace Research & Development Conference, Colorado Springs (Technical Edition and Reproduction Limited, London 1971).

Gloersen, P., T. Wilheit and T. Schmugge, "Microwave emission measurements of sea surface roughness, soil moisture, and sea ice structure," 4th Annual Earth Resources Program Review $\underline{1}$, 8-1 (1972) (NASA/JSC Document MSC-05937).

Hoekstra, P. and P. Cappillino, "Dielectric properties of sea and sodium chloride ice at UHF and microwave frequencies," J. Geophys. Res. $\underline{76}$, 4922 (1971).

Jakob, Max, "Heat transfer," $\underline{1}$, 449 (Wiley, 1949).

Ketchum, R. D. and W. I. Wittmann, "Infrared scanning the Arctic pack ice," USN Internal Report 68-115 (1968).

Lane, J. A., and J. A. Saxton, "Dielectric dispersion in pure polar liquids at very high radio-frequencies," Proc. Roy. Soc. $\underline{A214}$, 400 (1952).

Table 4.1

K_{air} = 1.00		
$K_{sea\ water}$ = 70.5 - i 36.0	Salinity = 35 o/oo
$K_{sea\ ice}$ = 4.0 - i 5.2 at 263°K	Salinity = 14 o/oo
4.0 - i 2.7 at 253°K	
4.0 - i 1.7 at 243°K	

Table 4.2

Date	Station	T_{ice}	T_{air}	ΔZ_{meas}	$T_{21\,cm}$	$\epsilon_{21\,cm}$	$\Delta Z/\lambda$
2-20-73	M0/M1	261°K	260.2°K	100 cm	—	—	—
2-20-73	M2G	263.2°K	260.2°K	14 cm	195°K	0.74	0.67
2-20-73	M2	261°K	260.2°K	40 cm	258°K	0.99	1.95
2-28-73	NW2	265.7°K	265.2°K	42 cm	—	—	—
2-28-73	NW5	—	265.2°K	65 cm	—	—	—
2-28-73	NW5G	269.2°K	265.2°K	8 cm	—	—	—
2-28-73	SE4G	269.2°K	264.2°K	19 cm	—	—	—
2-28-73	SE0	266.2°K	264.2°K	87 cm	—	—	—
2-28-73	SE1	266.2°K	263.7°K	74 cm	—	—	—
2-28-73	SE1G	269.2°K	263.7°K	14 cm	185°K	0.69	0.67
3-5-73	A5	261.2°K	256.2°K	71 cm	—	—	—
3-5-73	A1	263.6°K	257.2°K	65 cm	—	—	—
3-5-73	A3G	266.2°K	258.2°K	25.5 cm	—	—	—
3-5-73	Lead 2	269°K	253°K	—	169°K	—	—
3-5-72	Lead 3	265°K	253°K	—	215°K	—	—
3-5-73	(18)Thick	261.7°K	253°K	—	250°K	—	—
3-5-73	(18)Thin	265.9°K	253°K	) —	182°K	—	—
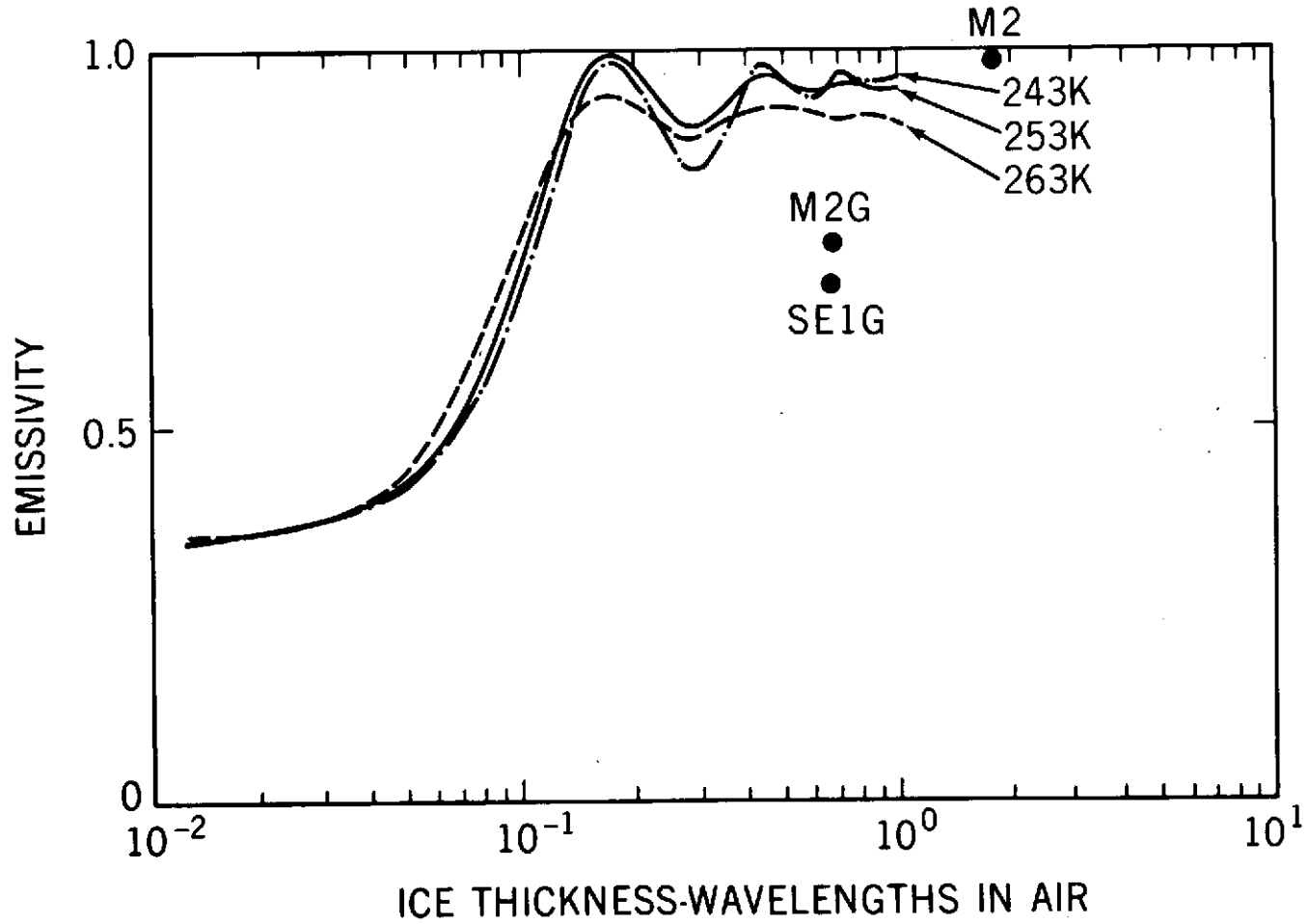
Figure 4.1. Microwave emissivity of sea ice as a function of ice thickness in units of microwave wavelengths in air, based on a simple three-layer theory (see text). Experimental points have been added for the sake of comparison.
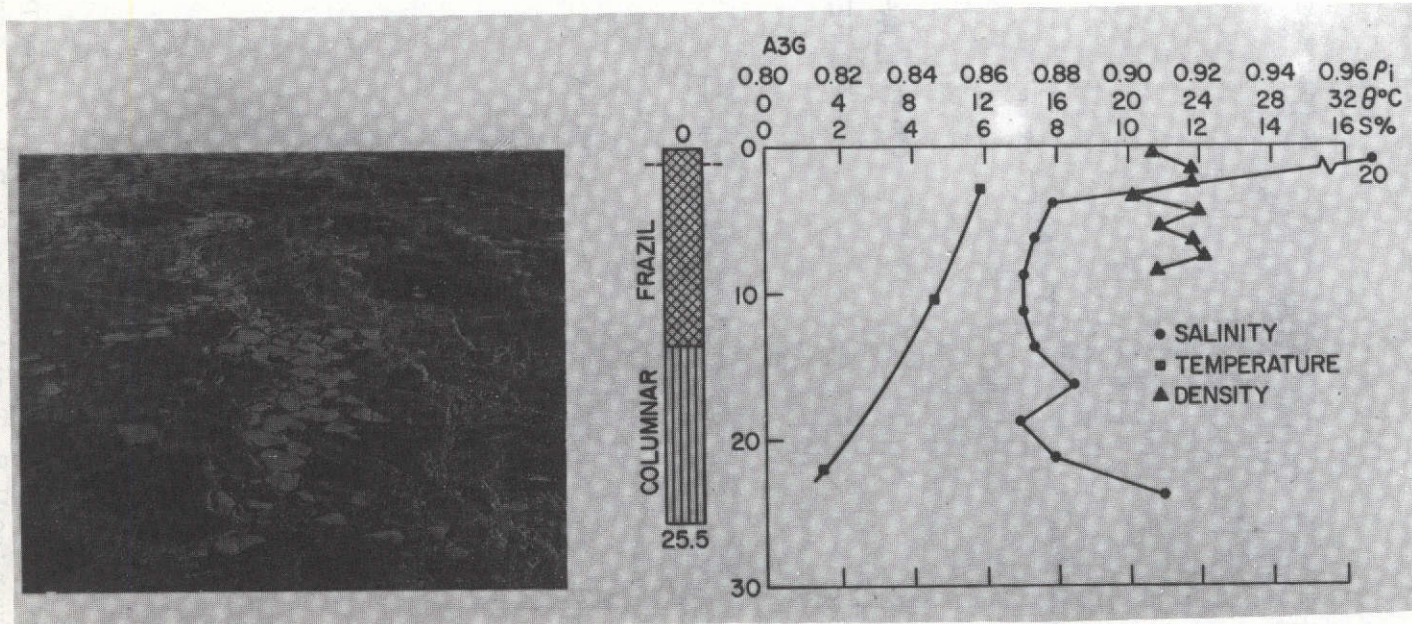
Figure 4. 2.   Aerial View and Surface Test Data for Test Point A3G
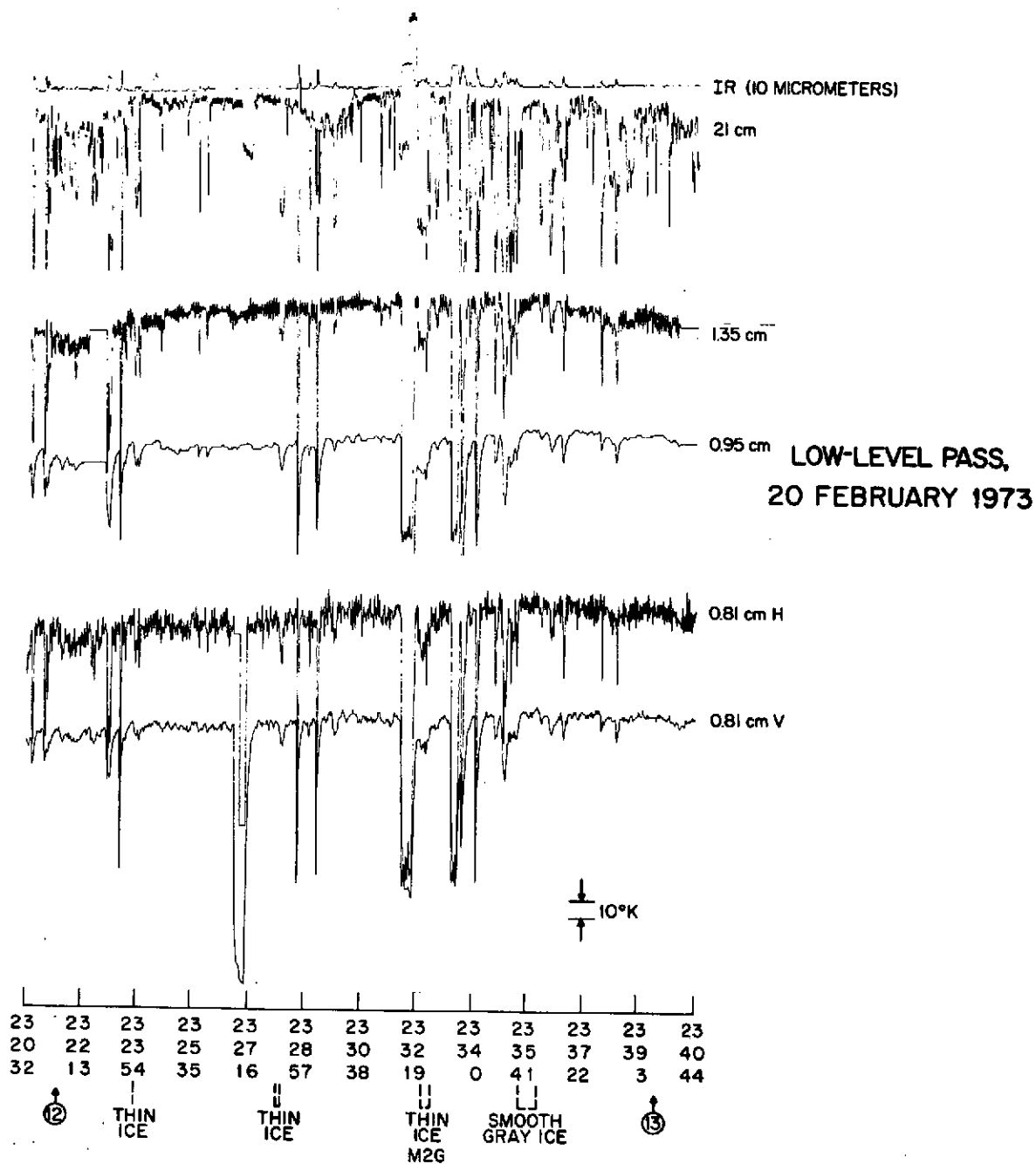
Figure 4.3. Multiwavelength Data Obtained During the Low Pass of the
Aircraft Over the U. S. Test Area on 20 February 1973

IR (IO MICROMETERS)

21 cm

2.81 cm H

2.81 cm V

1.35 cm

LOW-LEVEL PASS,
5 MARCH 1973

0.95 cm

0.81 cm H

0.81 cm V

23	23	23	23	23	23	23	23	23	23	23
27	28	30	32	34	35	37	39	40	42	44
16	57	38	19	0	41	22	3	44	25	6

*⑱
THIN ICE

LEAD
2

LEAD
3

⑲
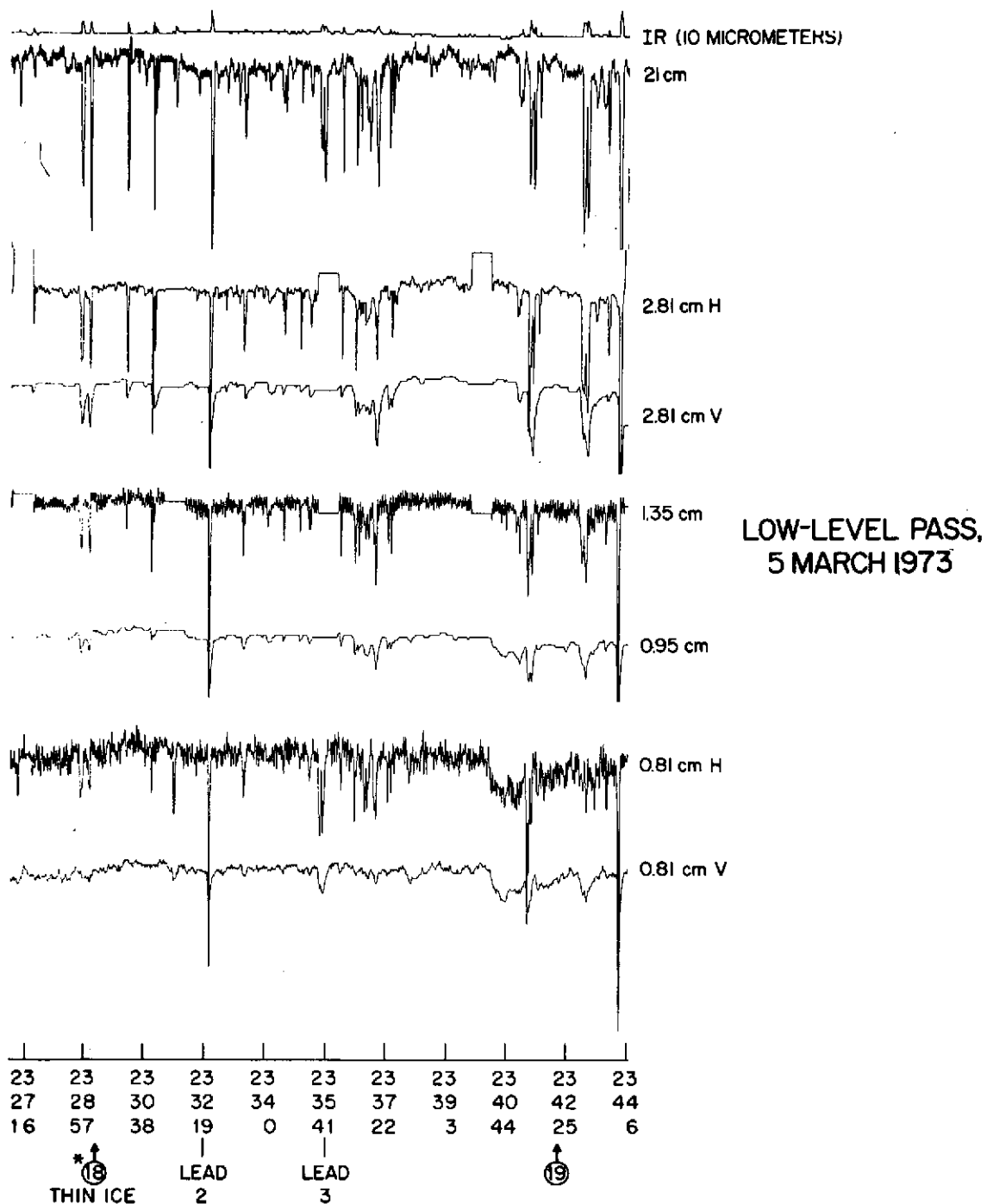
Figure 4.4.   Multiwavelength Data Obtained During the Low Pass of the
Aircraft Over the U.S. Test Area on 5 March 1973

119

BERING SEA EXPERIMENT
5 MARCH 1973
10 MICROMETER IMAGE
300 METER ALTITUDE
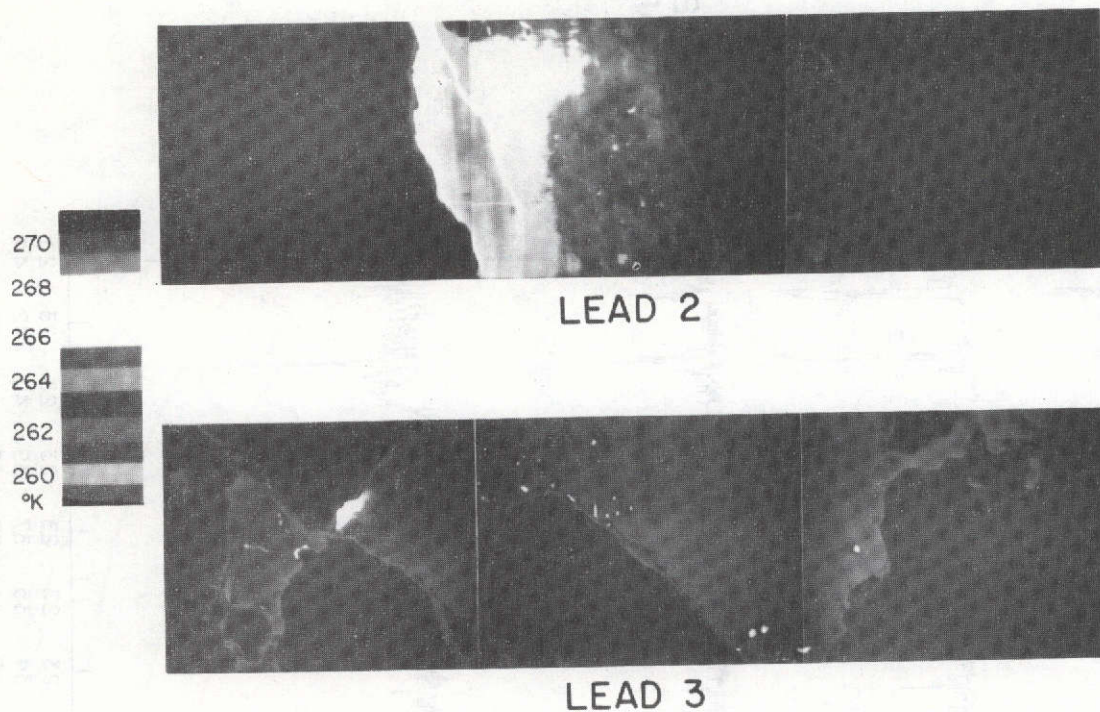
Figure 4.5. Infrared images obtained during the low altitude aircraft pass over the U.S. test area on 5 March 1973. Leads 2 and 3 are indicated also on Figure 4.4.
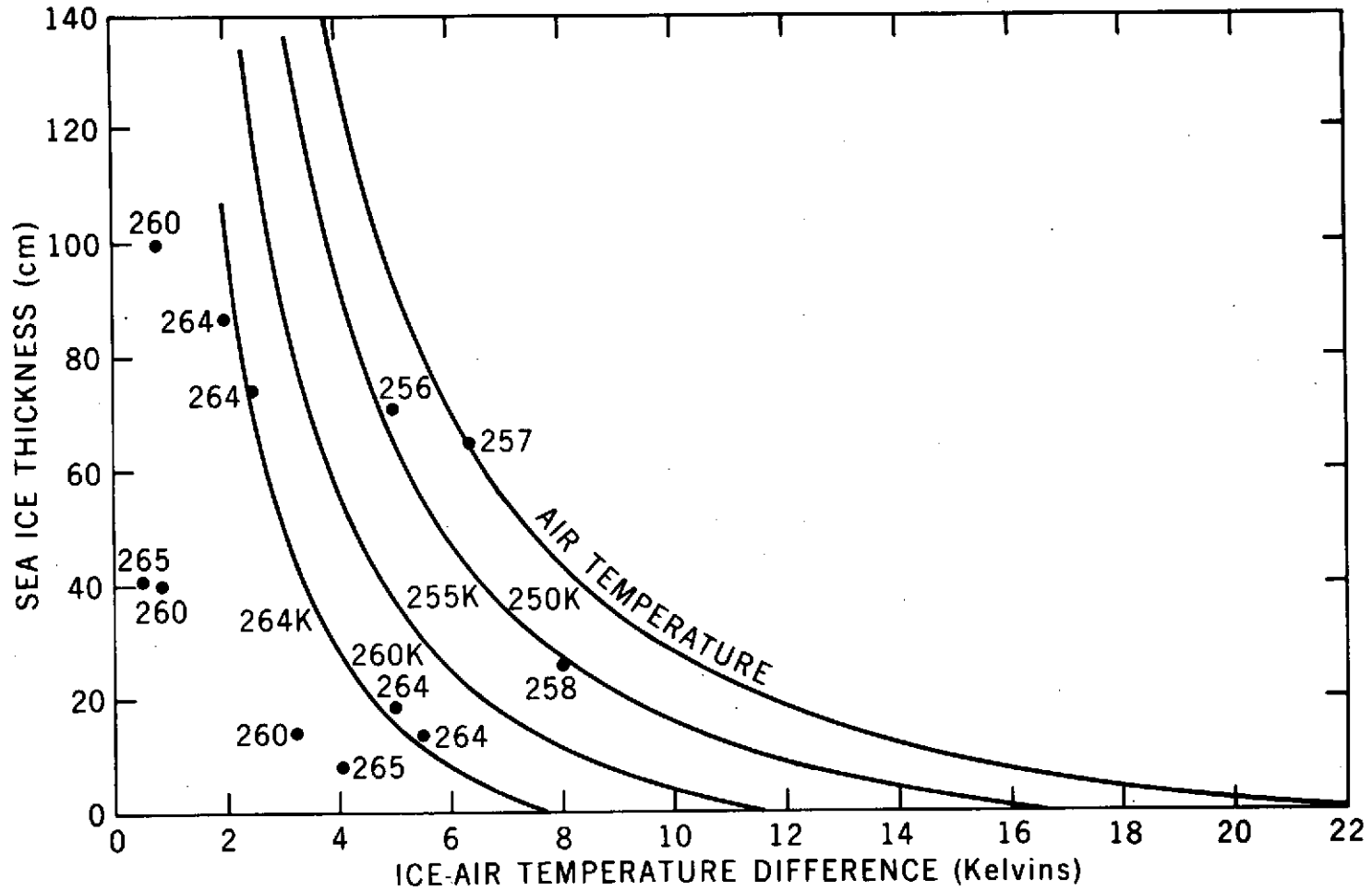
Figure 4.6. Plot of Equation 4.1, with experimental data also plotted for comparison. The numbers above the points refer to the air temperatures at which the observations were made.

MICROWAVE RADIOMETRIC DETERMINATION OF ATMOSPHERIC PARAMETERS DURING THE BERING SEA EXPERIMENT

T. T. Wilheit*

M. G. Fowler[†]

G. Stambach*

P. Gloersen*

*Applications Directorate, Goddard Space Flight Center, Greenbelt, Maryland 20771

[†]Environmental Research and Technology, Inc., Lexington, Massachusetts

Paper No. 5

MICROWAVE RADIOMETRIC DETERMINATION OF ATMOSPHERIC PARAMETERS DURING THE BERING SEA EXPERIMENT

T. T. Wilheit

M. G. Fowler

G. Stambach

P. Gloersen

ABSTRACT

The necessary theory is developed for relating measured microwave brightness temperatures at wavelengths varying from 0.8 to 2.8 cm to linear functions of the atmospheric water vapor, cloud liquid water content and surface wind speed. These linear relationships are inverted to yield meteorological parameters in terms of microwave measurements. These relationships are then applied to the microwave radiometer data taken from the Convair 990 on March 2, 1973 to infer the meteorological conditions along a 300 km track. The results are shown to be consistent with independent estimates based on meteorological observations and in situ measurements.

MICROWAVE RADIOMETRIC DETERMINATION OF ATMOSPHERIC PARAMETERS DURING THE BERING SEA EXPERIMENT

5.1 INTRODUCTION

Two of the Bering Sea Missions (February 26, 1973 and March 2, 1973) were designed to investigate the upwelling microwave radiation in precipitating frontal clouds. The data from these flights were exchanged and it was concluded that the March 2 flight was most suitable for further analysis. This paper presents the results of analysis of the microwave data taken on the CV-990. The aim of this analysis will be to use the measured brightness temperatures to infer the integrated atmospheric water vapor and liquid water content and the wind speed at the surface of the sea. These inferred meteorological parameters will be compared with independent measurements and inferences of their values.

5.2 INSTRUMENTATION

The data discussed here are from six different instruments, five radiometers and a cloud particle spectrometer. The radiometers operated at wavelengths of 2.8 cm, 1.55 cm, 1.35 cm, 0.95 cm, and 0.81 cm. The properties of the microwave radiometers are summarized in Table 5.1.

The 2.8 cm radiometer, which viewed 38° to the rear of the aircraft, was cycled between horizontal and vertical polarization with a four second period. It was calibrated for 32 seconds at 256 second intervals in synchronism with identical cycles by the 1.35 and 0.95 cm radiometers. The signal from each of these radiometers was averaged for 1 minute intervals; a time shift appropriate to the aircraft altitude and speed was introduced into the 2.8 cm data to align the data with that from the nadir-viewing radiometers, at least for surface features.

The 1.55 cm radiometer was scanned electrically from 50° to the left, through nadir to 50° to the right in 39 steps every 2 seconds. At the end of each scan the instrument viewed alternately either a warm (320°K) or cold (77°K) load for calibration purposes. The data were averaged for this analysis through the 5 beam positions near nadir and for periods of one minute.

The upward viewing 0.81 cm radiometer cycled through a warm calibration load (320°K) a cold calibration load (77°F) and the antenna at a 30 second rate spending equal time on each. The first half of the data for each of these 10 second intervals must be discarded because of the transient response of the integrator. Thus for only 5 seconds out of every 30 were useful radiometric data being taken; only the useful portion of the data were included in the average. Because there is very little atmospheric radiation coming from above 10 km altitude at this wavelength, the high altitude portion of each flight served to confirm the calibration of this instrument which was found to be stable to within 1°K.

For each of the radiometers, a calibration offset was assumed in order to bring the values of the inferred parameters into agreement with the meteorological observations. These offsets are given in Table 5.1. The large biases needed for the 2.8, 1.35 and 0.95 cm radiometers would seem to be caused by a mismatch in the external calibration target which was used to calibrate all of them. The bias observed in the 1.55 cm radiometer is consistent with a smaller, but significant, mismatch. The external standard used for the 0.81 cm upward-viewing radiometer, the 3°K cosmic background, is the same as the assumed background for the calculations, so no offset is possible.

The design of the cloud particle spectrometer has been discussed in detail by Blau et al (1970), and Ryan et al (1972). Basically, an optical cell was located

in the free air flow outside of the aircraft where the coincidence of a laser beam and a detector field of view defined a sample volume small enough to contain only one cloud particle at a time. As this volume was swept through space by the motion of the aircraft, droplet concentrations were determined from individual scattered light pulse count rates, and size distributions were derived from the distribution of pulse amplitudes. To record the droplets encountered, twelve channels of droplet diameter size were established. Eleven of these covered a range from 4.4 to 110 μm; since most cloud droplets have diameters within this range, the cloud droplet population was well represented by counts within these channels. The twelfth channel was included to count all droplets with diameters greater than 110 μm; these would be intermediate size drops, precipitation size drops, or ice crystals. The detailed discussion of data from this instrument for this flight is given by Fowler et al (1974).

5.3 METEOROLOGICAL CONDITIONS DURING THE MARCH 2, 1974 MISSION

The experiment performed on March 2, 1974 sampled an extensive cloud system associated with a dissipating warm occlusion and a developing secondary cyclone (Figure 1). The measurements were made at altitudes of 0.16, 2, 4, and 11 km along a narrow strip from 55°N, 171°W (point A, Figure 5.1) to 58.3°N, 172.5°W (point B, Figure 5.1), a flight path almost perpendicular to the primary frontal system and intersecting the secondary low centered at 55°N and 170°W.

On the day prior to this flight the primary low had been located near 49°N, 173°E with the associated frontal system trailing to the southeast and beginning to occlude. This cyclone moved northwestward to 54°N, 170°E during the twenty-four hours previous to the flight with no change occurring in the central pressure. At the same time, the frontal system swung well to the northeast into the Bering

127

Sea test area and advected a significant amount of warm air ahead of the system. This warm air mass was forced aloft as the system became occluded. At the time of the experiment (2300 GMT, 2 March 1973 – 0230 GMT, 3 March 1973), the front was thoroughly occluded, and no traces of the warm air mass were found at the surface.

Shortly before 0000 GMT, 3 March 1973 vorticity advection behind the front led to the development of a secondary cyclone near 55°N, 170°W. This cyclone effectively cut off most of the warm air advection associated with the primary front, and began feeding warm, moist air into the surface layer beneath with the second cold air mass. The resulting air mass contrasts encountered during the flight are shown in a schematic representation based on that developed by Danielsen (1959) in Figure 5.2. The associated cloud system and the aircraft measurements of wind are shown in a similar format in Figure 5.3.

The observations made from the Convair 990 showed that the clouds were structured into a multilayered stratiform system with maximum cloud heights below 10.5 km. North of 57°N, a cirrus canopy topped the system between altitudes of 8 and 10 km with a thin layer of cirrocumulus forming its base at 7.5 km. Below this canopy was a layered mass of altostratus and altocumulus which stretched as far south as 56.5°N and formed the top of the cloud mass throughout most of the warm air sector. Underneath this layer was one of dense altostratus topping at 6 km as far south as 56.5°N, then dropping to 4.5 km as the cloud penetrated the secondary cold front. In the regions where clouds occurred above the altostratus, the layers were frequently separated by a thin strip of clear air.

Below 4 km, the stratiform pattern began to change to a cumuliform situation. Multilayered altocumulus was found between 2 and 4 km from 58°N almost

as far south as 55°N; beneath this stratocumulus, cumulus and stratus fractus were found from 2 km down to below 100 m in altitude. These clouds were quite cellular in structure below 200 m, and the cells often appeared to grow and dissipate during the experiment. The upper cloud levels were far more stable in structure with differences due more to the slow northward motion of the front than to marked internal changes.

The Convair 990 sampled this cloud system at four different levels, 11 km, 4 km, 2 km, and 160 m. The high level pass was above the entire cloud mass, from south to north. Upon its completion at 57.5°N the aircraft descended through cirrus, cirrostratus, and altostratus to four kilometers and the sampling of cloud droplets was begun. The four kilometer pass was made primarily in the altostratus layer, although the stretch between 56.5°N and 56°N occurred in the clear air strip separating the altostratus from stratocumulus, and only clear air was encountered south of 55.6°N. The cloud particle samples of altostratus made at this level indicated that the cloud was at least partially frozen north of 56.5°N, and primarily liquid south of 56°N (Fowler et al, 1974).

Near 55°N the aircraft turned and descended to two kilometers to begin a northward run through the stratocumulus. This leg of the flight was continuously in cloud and was characterized by very limited variability in the cloud parameters along the flight path. The final pass of the experiment was made through the cloud base at 150 m; this started at 57.5°N and terminated at 55°N. The cloud liquid water content varied considerably at this level. Heavy snow, limited visibility, and easterly winds of 35-40 knots were reported north of 56°N. South of this boundary, a change to rain and decreasing winds showed the penetration of the low level warm air mass. This change in air mass was also indicated by the

129

termination of the main cloud system and the occurrence of small cumulus cells.

5.4 THEORY

At microwave wavelengths (0.1 - 30 cm) and at temperatures typical of the Earth and its atmosphere (200 - 300°K), the Rayleigh-Jeans approximation for the intensity of thermal radiation from a blackbody is quite valid; thus the equation of radiative transfer for an isotropic, nonscattering medium may be written

$$\frac{d T_B(\theta, \phi)}{dX} = \gamma \left[T(X) - T_B(\theta, \phi) \right]$$

where $T_B(\theta, \phi)$ is the radiance in the particular direction (θ, ϕ) expressed as equivalent blackbody temperature, $T(X)$ is the thermodynamic temperature of the absorbing medium and γ is the absorption coefficient. Distance along a ray path is denoted by X. The physical meaning of this equation is made clear if we examine the effect on microwave radiation incident at an angle θ, on an absorbing slab of uniform temperature, T_0, absorptivity γ_0, and of thickness δ as shown in Figure 5.4. The radiation coming out the other side consists of the incident radiation as attenuated by the slab $T_B e^{-\gamma_0 \delta sec(\theta)}$ plus a reradiation component $(1 - e^{-\gamma_0 \delta sec(\theta)}) T_0$. If the expression $\gamma_0 \delta \sec \theta$ is quite small or if $T_0 - T_B$ is small, the slab has no effect on the intensity of the radiation; whereas, if the slab is opaque ($\gamma_0 \delta \sec \theta = \infty$) the radiation emerging is characterized by the thermodynamic temperature of the slab independent of the intensity of the incident radiation.

The effect at a reflecting interface such as the ocean surface is similar. The brightness temperature radiating from a surface is given by

$$T_B = \epsilon \, T_{surface} + (1 - \epsilon) \, T_{B\,incident}$$

where ϵ is the emissivity of the surface, a dimensionless number between 0 and 1. $T_{surface}$ is the thermodynamic temperature of the surface and $T_{B\,incident}$ is the incident brightness temperature spatially averaged as appropriate for the surface structure. Since most natural surfaces are quite rough when considered on a scale of centimeters it seems most appropriate to use the Lambertian approximation (Peake et al, 1966) for the angular distribution of the incident radiation which is reflected toward the radiometer

$$T_{B\,incident} = 2 \int T_B(\theta) \, \cos(\theta) \, \sin(\theta) \, d\theta$$

where $T_B(\theta)$ is the downwelling radiation at an angle θ with respect to zenith and is assumed to be azimuthally symmetric. The integral is over the upper hemisphere only. Since the function $T_B(\theta)$ varies smoothly with angle except near the horizon and since the weighting function in the integrand, $\cos(\theta) \sin(\theta)$, has a maximum at $\theta = 45°$, we will approximate T_B incident by $T_B(45°)$ for purposes of computation.

The only constituents of the atmosphere which have any consequential effect on radiation transfer for wavelengths between 3 mm and 30 cm are molecular oxygen, water vapor and liquid water. Molecular oxygen has a series of magnetic dipole resonances near 5 mm wavelength and a single resonance at 2.5 mm wavelength. These resonances are strong enough that even in the far wings of the lines, the effect can amount to several Kelvins. The specific model used for calculation here is that given by Meeks and Lilley (1963) as modified by Wilheit (1969).

Water vapor has a single weak resonance at 1.35 cm and a number of strong

ones at wavelengths shorter than 0.2 cm. The model used here is that given by

Staelin (1966) which includes the 1.35 cm resonance explicitly and has a term

proportional to frequency squared to approximate the sum of the short wavelength

resonances. One of the principal features of this model is that there is a local

minimum in the absorption coefficient near 0.95 cm at one atmosphere pressure.

Also since the 1.35 cm radiometer is centered on a resonance and has a band-

width (250 mHz) which is small compared to the pressure broadened line width

(2.7 mHz/mb) over the region of the atmosphere likely to contain substantial

amounts of water vapor (below the 200 mb level), the contribution to the bright-

ness temperature of this channel is approximately inversely proportional to the

pressure at which the water vapor is found. Accordingly, the brightness tem-

peratures will be interpreted in terms of a weighted water vapor content V

where
$$V = \int \rho(h) \times \frac{1000 \text{ mb}}{p(h)} dh$$

where $\rho(h)$ is the density of water vapor as a function of height, h and p (h) is

the pressure profile.

The model used for the absorption coefficient of liquid water clouds, Rayleigh

absorption, is discussed in Gunn and East (1954). The principal assumption here

is that the size of the droplets is small compared to the wavelength divided by the

index of refraction of water. For the calculations here this means that the particles

must be much smaller than 2 mm diameter. Since the cloud particle spectrome-

ter rarely indicated any particles larger than 0.1 mm (Fowler et al., 1974), this

assumption is certainly reasonable. The dielectric constant used for this model

is that given by Lane and Saxton (1952). Since the real part of the dielectric constant of ice is only about 3 and the imaginary part is less than 10^{-2}, the effect of atmospheric ice particles is negligible.

Calculating the emissivity of a general surface is quite difficult and has not yet been done rigorously; however, it is quite simple to calculate the emissivity of a smooth dielectric interface by use of the Fresnel relations (Jackson, 1962) to calculate the (electric field) reflectivity R (θ, ϕ) from the dielectric properties of the surface as a function of viewing angle and polarization. The emissivity is then simply

$$\epsilon = 1 - |R(\theta, \phi)|^2$$

The Lane and Saxton (1952) dielectric constant data include the effect of salinity and are appropriate for use in calculating sea water emissivities.

For calculating the brightness temperature expected for a particular situation, the atmosphere is divided into 100 layers, each 0.2 km thick and characterized by a temperature, pressure, water vapor content and liquid water content. For downward-viewing radiometers, the calculation begins at the top layer with the 3°K cosmic background temperature, which is propagated downward through each of the 100 layers, reflected off the ocean surface and propagated back up to the altitude of the radiometer. For upward-viewing radiometers, the cosmic background is simply propagated downward to the radiometer altitude.

For each of the radiometers under consideration, the expected brightness temperatures for a number of situations were calculated. From these calculations, relationships between the atmospheric water (vapor and liquid) content were derived. For the low moisture values expected in the Bering Sea region

In the winter, a linear approximation is adequate:

$$T_B = A + BV + CL$$

where L is the net liquid water content and V is the weighted water vapor content as previously defined, except that the water vapor and liquid water above the aircraft are given a reduced weight since they are seen only in reflection. In the case of the lowest altitude run, virtually the entire atmosphere is above the aircraft eliminating the need for the different weights above and below the flight level, so the V and L values solved for represent the full vertical column. For the 0.81 cm upward-viewing channel, the value of V is the unweighted net water vapor above the aircraft. The values of A, B and C for the 4 flight altitudes are given in Table 5.2. In the downward-viewing radiometers, the value of A is primarily the sea surface emission with small contribution from cosmic background and atmospheric oxygen. The values of B and C give the sensitivity to water vapor and liquid water clouds, respectively. The values for C vary with assumed altitude for the 0.81 cm radiometer because the assumed cloud altitude, and thus temperature, was different in each case; the cloud layer was within the 2 km above the aircraft altitude. The value of C for the 11 km run was not calculated as the temperature would have been below that for spontaneous nucleation so liquid water would not likely exist above this level. For the lowest altitude run, an uncertainty of 1 gm/cm^2 in the water vapor content would cause an uncertainty of 6°K in the brightness temperature which, in turn, is equivalent to 7 mg/cm^2 uncertainty in the cloud liquid water content. Thus we may assume a water vapor content of 1 gm/cm^2 and find that: $L = 1.1 (T_B - 18°K)$ mg/cm^2 with an ambiguity contribution of less than 7 mg/cm^2 caused by water vapor.

Similarly for the 2 km run, we find that $L = 1.0 \, (T_B - 9)$ with an ambiguity of less than 3 mg/cm^2 and that $L = 0.9 \, (T_B - 7.7)$ with an uncertainty of less than 1 mg/cm^2 for the 4 km run.

The effect of wind is to roughen the ocean surface and to produce foam. Nordberg et al (1971) found that at a wavelength of 1.55 cm the net effect was to increase the brightness temperature at nadir by 1.2°K for each meter per second of wind speed above the 7 m/s foam threshold. In order to simplify the analysis, it has been assumed that the same relationship applies to the other wavelengths and viewing angles considered here. This very simple assumption clearly ignores the spectral variation of the ocean surface signature, but will prove to be adequate for the present purpose. An attempt to define a better model is the subject of Paper No. 6.

We thus have a series of equations relating the observed brightness temperatures to wind speed, and integrated liquid water and water vapor content.

$$T_{B\,2.8\,H} = A_{2.8\,H} + B_{2.8\,H}V + C_{2.8\,H}L + D\,(w - w_0)$$

$$T_{B\,2.8\,V} = A_{2.8\,V} + B_{2.8\,V}V + C_{2.8\,V}L + D\,(w - w_0)$$

$$T_{B\,1.55} = A_{1.55} + B_{1.55}V + C_{1.55}L + D\,(w - w_0)$$

$$T_{B\,1.35} = A_{1.35} + B_{1.35}V + C_{1.35}L + D\,(w - w_0)$$

$$T_{B\,0.96} = A_{0.96} + B_{0.96}V + C_{0.96}L + D\,(w - w_0)$$

where w is the surface wind speed and $D = 1.2$°K/m/s and $w_0 = 7$ m/s. Any three of these equations can be inverted for V, L and w and any combination of four or all five can be inverted in a least square brightness temperature error

135

sense as well. The inversions have been performed for the last three and for all five of these equations for each of the flight levels such that:

$$
\begin{pmatrix} V \\ L \\ W \end{pmatrix} = \begin{pmatrix} M_1 \end{pmatrix} \begin{pmatrix} T_{B1.55} - A_{1.55} + D w_0 \\ T_{B1.35} - A_{1.35} + D w_0 \\ T_{B0.96} - A_{0.96} + D w_0 \end{pmatrix}
$$

$$
\begin{pmatrix} V \\ L \\ W \end{pmatrix} = \begin{pmatrix} M_2 \end{pmatrix} \begin{pmatrix} T_{B2.8H} - A_{2.8H} + D w_0 \\ T_{B2.8V} - A_{2.8V} + D w_0 \\ T_{B1.55} - A_{1.55} + D w_0 \\ T_{B1.35} - A_{1.35} + D w_0 \\ T_{B0.96} - A_{0.96} + D w_0 \end{pmatrix}
$$

where M_1 is a 3×3 matrix and M_2 is a 3×5 matrix. The values are given in Tables 5.3 and 5.4 respectively.

In the earlier discussion of the instruments, it was mentioned that the approximate residual error in the measurements after the calibration biases were applied would be about $2°K$ for each radiometer. The reflection of this error on the determination of V, L and W can be calculated under the assumption that these errors are independent. These are given for both the 3-channel and 5-channel inversions in Table 5.5. Note that the addition of the 2.8 cm data drastically improves the quality of the wind speed measurement, significantly improves

136

the cloud liquid water measurements and hardly improves the water vapor measurement at all. It is also apparent that the uncertainty in the water vapor and liquid in the atmosphere is greatly increased for the lowest level run since the atmosphere is seen only in reflection off the surface.

5.5 MICROWAVE MEASUREMENTS

The one-minute averages of the brightness temperatures as measured by the downward-viewing radiometers are shown in Figures 5.5 through 5.8 plotted as a function of latitude. In most cases, the features can be related among all the channels but the overall slopes may be quite different. In particular, the 2.8 cm brightness temperature is greater at the northern end of every run than it is at the southern end, while the 1.35 cm shows little overall slope and the 0.96 cm shows the opposite slope in several cases. There is little in common among the various runs; the details of the meteorological conditions changed sufficiently to erase most small scale features in the roughly one half hour time separation of the runs.

The performance of the sensors was quite good during these runs. One one-minute sample of data for the horizontal channel of the 2.8 cm radiometer was lost due to a malfunction at about 57°N during the 4 km run and a sequence of points between 55°N and 55.7°N was lost for both polarizations on the 0.16 km run but a single one-minute average at the southern extreme of the run was obtained. A single one-minute sample of data from the 1.55 cm radiometer was lost near 56.7°N on this run also.

The 0.81 cm upward-looking radiometer data for the two lowest altitude runs are shown in Figure 5.9. These data are shown with two ordinates, brightness

137

temperature and integrated liquid water content above the aircraft. The very nearly direct relationship between the two has been established earlier. The dashed lines shown here are the estimates of the liquid water content based on the cloud particle spectrometer data as discussed in the Appendix. Much more structure is observed here than in the downward-viewing radiometers because these data are 5-second averages at half-minute intervals rather than the full minute averages of the data from the other radiometers. The 0.81 cm data for the 4 and 11 km runs were featureless and are not plotted here. For these runs, the average brightness temperatures were 6.7°K and 3.8°K with standard deviations of 0.8°K and 1.1°K respectively.

When the downward-viewing radiometer data are operated on with the matrices which have been derived, the brightness temperature data are inverted to yield estimates of the surface wind speed, cloud liquid water content and weighted water vapor content of the atmosphere. The results of this inversion are shown in Figures 5.10 through 5.13 for each of the runs. In each case, the solid line results from the three-channel (1.55 cm, 1.35 cm and 0.81 cm) inversion, the X's from the 5 channel inversion. The dashed line is the independent estimate obtained from meteorological and in situ observations as discussed in the Appendix.

5.6 DISCUSSION

The data set most easily interpretable is the upward-viewing 0.81 cm radiometer (Figure 5.9). It has been shown that the brightness temperatures measured by this sensor can be related to the liquid water content of the clouds with little ambiguity. What ambiguity there is results from scale factor uncertainties of the order of ten percent because of uncertainties in the temperature

to assign to the clouds, as well as the ambiguities in offset due to the water vapor uncertainty which are no more than 7 mg/cm^2 at the lowest altitude. This measurement is clearly a more reliable measure of the integrated liquid water than the estimates based on a small number of in situ measurements because of the difficulty in relating the water droplet density at a few levels to the total integrated water content of a column. The order-of-magnitude agreement between the two is, nonetheless, quite good. It can be seen in these data that the liquid water content between 55°N and 55.5°N is in the neighborhood of 20 to 30 mg/cm^2 and is fairly constant. In the area of the front (55.5°N to 56°N), the instability of the atmosphere produces a highly structured situation with cloud liquid water contents varying from near 0 to 45 mg/cm^2 in a short space. The cloud particle spectrometer data also indicate a maximum of this magnitude in the same area. The broad peak in the dashed line is meant to indicate that peak values of the order of 50 mg/cm^2 might be expected near 56°N (the area of strong convection): the expected average value would be in the neighborhood of 20 mg/cm^2. North of 57°, although the cloud particle spectrometer and visual observations indicated considerable cloudiness, the radiometer data show that the clouds contained very little (less than 5 mg/cm^2) liquid water. The measurements of liquid water above 2 km show that the clouds south of 55.2°N are confined primarily to the bottom 2 km of the atmosphere which is consistent with the cloud observations summarized in Figure 5.3.

The upward-viewing radiometer showed a RMS fluctuation of 1.1°K for the 4 km run as compared to 0.8°K for the 11 km run. This excess can be explained with an average of less than 1 mg/cm^2 liquid water above the 4 km level, which is consistent with the assumption used in the Appendix that the clouds above 4 km consisted almost entirely of ice.

The cloud liquid water interpretations made from the downward-viewing radiometers are in substantial agreement, given that the details of the situation must certainly change over the better than two-hour span of the measurements. The 20-30 mg/cm^2 south of 55.5°N, the structure and variability in the immediate neighborhood of the front (55.5 - 56.5°N), and the general dryness north of 57°N are observed in all cases. Although the observation times are the same, one would not expect the downward-looking data from the 0.16 km run to show the sharp maximum seen in the upward-looking data. At this altitude, the downward-looking measurements contain cloud information only through diffuse reflection off the rough sea surface, thereby sampling an effective cloud area several kilometers in diameter, which is larger than one would expect for a convection cell such as would produce the sharp maximum seen in the upward-looking data.

North of 55.5°N, the inversions for weighted water vapor agree well with the estimates developed in the Appendix. In this region, the estimate is based primarily in the assumption of 95% relative humidity in the liquid water clouds so the uncertainty in the estimate is dominated by the uncertainty in the temperature profile so one would expect this estimate to be accurate to within 10%. However, south of 55.5°N all the microwave data indicate considerably more vapor than arrived at by meteorological reasoning. The key to the decrease in the estimate in this region is the assumption of 20% relative humidity in the clear air mass; 50% would be required to bring the humidity data into agreement. This would be unexpected but quite possible, so that the humidity data can be reconciled with reasonable meteorological assumptions.

The wind speed determinations showed similar agreement. The main wind feature was an increase from about 10 m/s to 20 m/s from the south to the north of the front. This was observed in all the microwave determinations with overall agreement of the order of 3 m/s RMS deviation. The primary discrepancy is that the estimate of surface wind which was made by extrapolating the inertial navigation system data to the surface shows a much more abrupt wind change across the front than is seen in the microwave data. A large contributor to this discrepancy is that the extrapolation algorithm used was changed abruptly at the position of the front, whereas a more gradual change would have been more realistic. Also, the 5-channel inversion, which is dominated by the 2.8 cm data, shows a larger gradient than the 3-channel inversion where the wind speed comes primarily from the 1.55 cm measurements. This implies that the assumption of the same wind speed effect in all channels is inadequate, which is not surprising. The horizontally polarized 2.8 cm measurements should show a roughness contribution which should be absent or quite small in the other measurements (Stogryn, 1967; Hollinger, 1971). The foam contributions should be comparable for all channels, thus the roughness contribution enhances the effect for the 2.8 cm measurements as compared to the other channels.

5.7 CONCLUSION

We have shown that from simple models an algorithm can be developed to relate microwave radiometric measurements to surface wind speed, liquid water content, and water vapor content over the oceans. When this algorithm is applied to real data, the results are consistent with estimates of these parameters arrived at independently. While it was necessary to adjust the absolute calibration of four of the radiometers (see "Calibration Bias," Table 5.1) in order to obtain

consistent inversions, the same adjustments were used in making twenty-four independent comparisons (two inversions for three parameters at four levels). Therefore, these adjustments do not greatly reduce the significance of the over-all consistency. Moreover, these biases are understandable in terms of the calibration targets actually used on these instruments. We have shown that these meteorological parameters can indeed be measured with useful accuracy with passive microwave techniques. The most significant question that must be settled to improve these determinations is a much more accurate measurement of the microwave effect of the wind speed.

5.8 APPENDIX: ESTIMATES OF WATER VAPOR,

LIQUID WATER AND WIND SPEED

The estimation of the meteorological parameters for comparison with their values which were derived from the radiometric data necessitated a considerable amount of judgment as to the vertical variations, since only measurements at four discrete levels were taken. Further, the in situ measurements of water vapor were not reliable so relative humidity values appropriate to the meteorological situation had to be assigned to each air mass. Finally, extrapolation of the surface winds was needed since these could be significantly different from the winds which were measured by the inertial navigation system at the 160 m flight altitude.

To determine the weighted water vapor content, the vertical temperature structure along the flight path was determined from the aircraft temperature measurements and any conventional data available. The relative humidity of the air masses was then estimated, with 95% assumed for all areas of dense cloudi-ness, 40% for the thin cirrus area found in the warm air aloft, and 20% for the

cold, dry air behind the front. The assumption of near saturation should be quite accurate for the cloud-filled areas. The other areas would be associated with very cold temperatures whose water vapor contents would not be large even under saturated conditions; hence, errors in the estimate of relative humidity would create only moderate errors in the overall estimate of integrated water vapor. Finally, values of absolute water vapor and atmospheric pressure were determined for each 0.2 km layer of the atmosphere up to 10 km, and weighted water vapor values were computed with appropriately reduced weight above the aircraft for 0.5° latitude intervals and are shown in Figure 5.10 through 5.13. These calculations result in weighted water vapor contents ranging from 1.3 gm/cm^2 to 1.9 gm/cm^2; the corresponding range of the more conventional unweighted water vapor content is 1.0 gm/cm^2 to 1.4 gm/cm^2, so that the assumption of 1 gm/cm^2 uncertainty in the water vapor content in the interpretation of the 0.81 cm upward viewing radiometer is quite conservative.

The in situ measurements of liquid water were used to estimate liquid water contents of the clouds encountered. Above 4 km it appeared that the clouds were primarily frozen and little liquid water was present. The integration of liquid water is based on the lower cloud levels for which data was available at 4, 2, and 0.16 km. In the 2 km run, the clouds above the aircraft have reduced weight as in the case of water vapor. These results are indicated also in Figures 5.9 – 5.13 by dashed lines. The broad maximum shown at 56°N must not be interpreted literally but peaks of this magnitude may be expected on a more localized basis in this area.

Surface winds were estimated from the 160 m winds encountered by the aircraft. North of 56°N, considerable turbulence and mixing characterized the low

levels. Because of this, it was assumed that the surface winds should be equal to 160 m winds. This was supported by surface observations made in the area. South of 56°N, the air was warmer than the underlying ocean, a situation which tends to inhibit convection and turbulence. Thus the change in the wind with height should reflect the decreasing effect of friction and may be approximated by the Ekman spiral. Under such conditions, the surface wind speed should be approximately 0.61 of the wind speed found above the friction layer (Pettersen, 1956). Since the wind speed and direction encountered at 160 m correlates well with that at 2 km, it can be assumed that this wind represents free flow. Following this reasoning, the surface wind speed is assumed to be 0.61 of the 160 m speed. This leads to a decrease of 8 m/s in the surface wind across the front, a decrease which is supported by an observed decrease in foam from 20-25% down to 5%. Two-minute averages of these values are shown in Figures 5.9-5.13.

ACKNOWLEDGMENT

REFERENCES

1. Blau, H. H. Jr., M. L. Cohen, L. B. Lapson, P. von Thuna, R. T. Ryan and D. Watson, "A Prototype Cloud Physics Laser Nephelometer" Applied Optics, 9 1798 – 1803 (1970).

2. Danielson, E. F., "The Laminar Structure of the Atmosphere and its relation to the concept of a tropopause" Archiv für Geophysik und Meteorologie, Klimatologie A Vol. II #3 (1959).

3. Fowler, M. G., E. W. Fasci, Jr., H. H. Blau Jr., "The Bering Sea Expedition – Flight 10, Cloud Microstructure Studies" Final Report Contract Number NAS5-21910, Environmental Research and Technology Inc., Lexington, Massachusetts, (1974).

4. Gunn, K. L. S. and T. U. R. East, "The Microwave Properties of Precipitation Particles", Quart. J. Met. Soc., 80 522-545, 1954.

5. Hollinger, J. P., "Passive Microwave Measurements of Sea Surface Roughness", Trans. IEEE Geoscience Electronics, GE-9, pp. 165-169 (1971).

6. Lane, J. A. and J. A. Saxton, "Dielectric Dispersion in Pure Polar Liquids at Very High Radio Frequencies", Proc. Roy. Soc. London A, 214, pp. 531-545, 1952.

7. Meeks, M. L. and A. E. Lilley, "The Microwave Spectrum of Oxygen in the Earth's Atmosphere", J. Geophys. Res. 68, 6, 1963.

8. Nordberg, W., J. Conaway, D. B. Ross, and T. Wilheit, "Measurements of Microwave Emission from A Foam-Covered Wind Driven Sea", J. Atmos. Sci., 28, 429-435, 1971.

9. Peak, W. H., R. L. Riegler, and C. A. Shultz, "The Mutual Interpretation of Active and Passive Microwave Sensor Outputs", Proc. 4th Symp. on Remote Sensing of Environment, Univ. of Mich., 1966.

10. Pettersen, S., "Weather Analysis and Forecasting", Vol. I, McGraw Hill Book Company, New York (1956).

11. Ryan, R. T., H. H. Blau, Jr., P. C. von Thuna, M. L. Cohen and G. D. Roberts, "Cloud Microstructure as Determined by an Optical Cloud Particle Spectrometer", Journal of Applied Meteorology 11, 149-156 (1972).

12. Staelin, D. A., "Measurements and Interpretation of the Microwave Spectrum of the Terrestrial Atmosphere Near 1 Centimeter Wavelength", J. Geophys. Res., 71, 2875-2881, 1966.

13. Stogryn, A., "The Apparent Temperature of the Sea at Microwave Frequencies", Trans. IEEE Ant. and Prop., AP15 278-286, 1967.

14. Wilheit, T. T. Jr., "Microwave Absorption and Emission by Atmospheric Oxygen" PhD Thesis Massachusetts Institute of Technology (1969).

Table 5.1

Radiometer Characteristics

Wavelength	2.8 cm	1.55 cm	1.35 cm	0.96 cm	0.81 cm
Frequency	10.7 GHz	19.4 GHz	22.2 GHz	31.4 GHz	37.0 GHz
Viewing Angle	38° Aft of Nadir	Scanned	Nadir	Nadir	25° Left of Zenith
NE ΔT as Averaged	0.13° K	0.16° K	0.09° K	0.09° K	0.8° K
Calibration Bias	-17.3° K	-1.6° K	-12.4° K	-7.6° K	—

Table 5.2

Brightness Temperature Constants

Flight Altitude	11 km			4 km			2 km			0.16 km		
	A	B	C	A	B	C	A	B	C	A	B	C
2.8 cm Horiz.	94.8	.73	.14	94.3	.77	.14	93.7	.79	.14	93.1	.40	.07
2.8 cm Vert.	132.6	.58	.11	132.2	.59	.11	131.9	.58	.11	131.3	.31	.05
1.55 cm	126.1	5.43	.33	125.7	5.69	.33	125.4	5.87	.33	124.9	3.32	.19
1.35 cm	130.6	14.47	.41	130.2	14.88	.41	129.8	15.36	.41	129.3	9.17	.24
0.96 cm	144.9	4.91	.69	144.4	4.66	.69	143.8	4.84	.69	143.0	2.70	.41
0.81 cm	4.0	1.5	—	6.7	4.2	1.12	8.7	5.10	1.00	12.0	6.00	.87
	$°K$	$\dfrac{°K\ cm^2}{gm}$	$\dfrac{°K\ cm^2}{mg}$	$°K$	$\dfrac{°K\ cm^2}{mg}$	$\dfrac{°K\ cm^2}{mg}$	$°K$	$\dfrac{°K\ cm^2}{mg}$	$\dfrac{°K\ cm^2}{mg}$	$°K$	$\dfrac{°K\ cm^2}{mg}$	$\dfrac{°K\ cm^2}{mg}$

For all radiometers: $D = 1.2°K\text{-sec}/m$

$W_0 = 7\ m/sec$

Table 5.3

Matrix Elements for M_1, Used In 3-Channel Inversions

Altitude	Row/Column	1.55 cm	1.35 cm	0.96 cm	
11 km	V	-.084	.108	-.024	gm/cm^2 °K
	L	-3.02	.306	2.71	gm/cm^2 °K
	W	2.04	-.572	-.637	m/s °K
4 km	V	-.082	.105	-.023	gm/cm^2 °K
	L	-3.01	.301	2.71	mg/cm^2 °K
	W	2.05	-.581	-.635	m/s °K
2 km	V	-.080	.103	-.023	gm/cm^2 °K
	L	-3.01	.294	2.71	mg/cm^2 °K
	W	2.05	-.584	-.634	m/s °K
0.16 km	V	-.129	.167	-.038	gm/cm^2 °K
	L	-4.91	.471	4.44	mg/cm^2 °K
	W	1.97	-.536	-.598	ms °K

Table 5.4

Matrix Elements for M_2, Used In 5-Channel Inversions

Altitude	Row/Column	2.8 cm H	2.8 cm V	1.55 cm	1.35 cm	0.96 cm	
11 km	V	-.022	-.021	.0040	.083	-.043	gm/cm² °K
	L	-.652	-.805	-.065	-.539	2.06	mg/cm² °K
	W	.481	.481	.170	-.036	.227	m/s °K
4 km	V	-.022	-.020	.004	.080	-.042	gm/cm² °K
	L	-.648	-.800	-.069	-.553	2.07	mg/cm² °K
	W	.445	.481	.169	-.036	-.227	m/s °K
2 km	V	-.021	-.020	.004	.078	-.041	gm/cm² °K
	L	.646	-.795	-.072	-.563	2.08	mg/cm² °K
	W	.445	.481	.161	-.034	-.228	m/s °K
0.16 km	V	-.035	-.031	.004	.130	-.068	gm/cm² °K
	L	-1.03	-1.36	-.078	-.862	3.33	mg/cm² °K
	W	.425	.468	.168	-.040	-.189	m/s °K

Table 5.5

Error Estimates

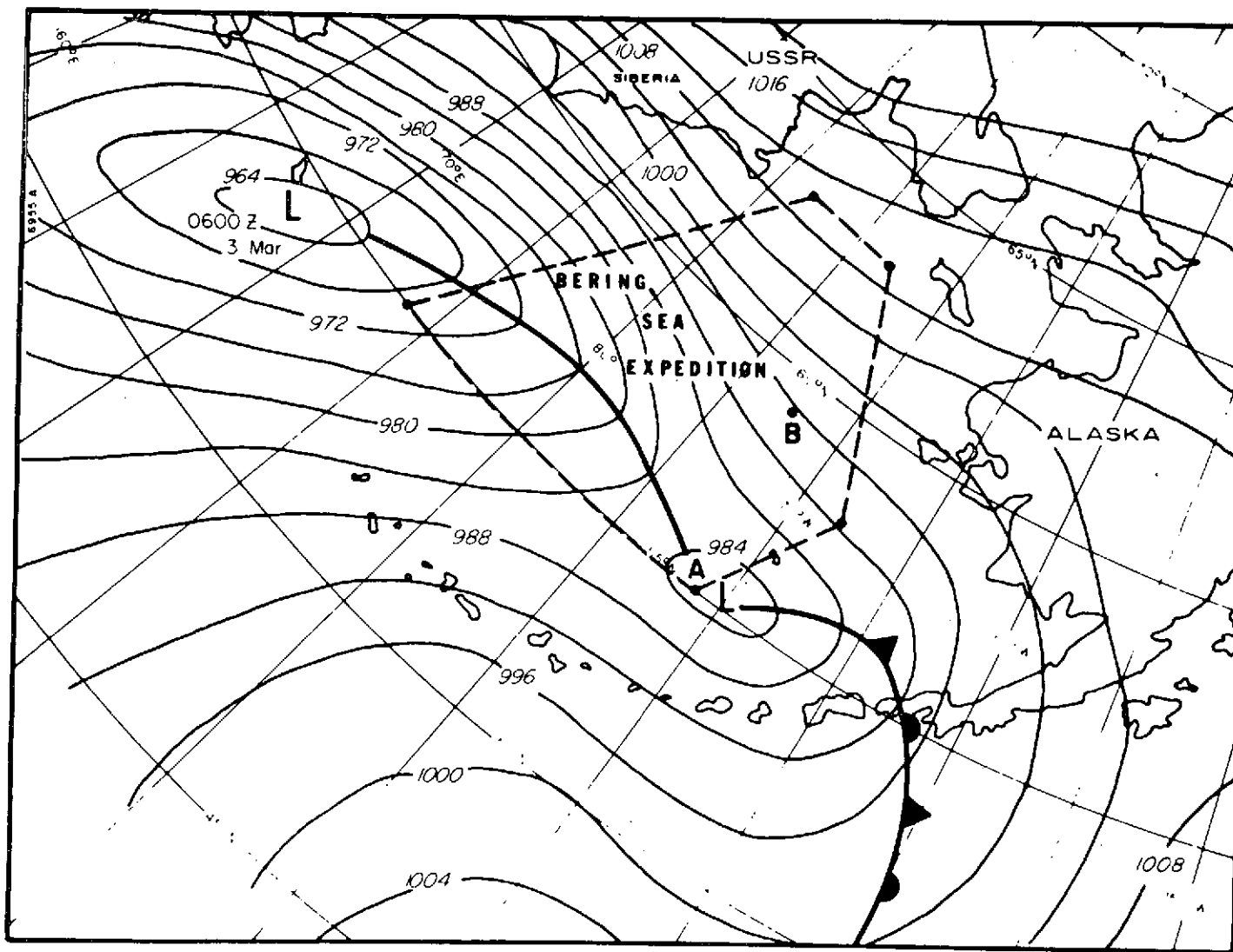|		3 Channel Inversion	5 Channel Inversion	
11 km	V	.28	.20	gm/cm^2
	L	8.1	4.7	mg/cm^2
	W	4.4	1.4	m/s
4 km	V	.27	.19	gm/cm^2
	L	8.1	4.8	mg/cm^2
	W	4.4	1.4	m/s
2 km	V	.26	.19	gm/cm^2
	L	8.1	4.8	mg/cm^2
	W	4.4	1.4	m/s
0.16 km	V	.43	.31	gm/cm^2
	L	13	7.6	mg/cm^2
	W	4.2	1.4	m/s

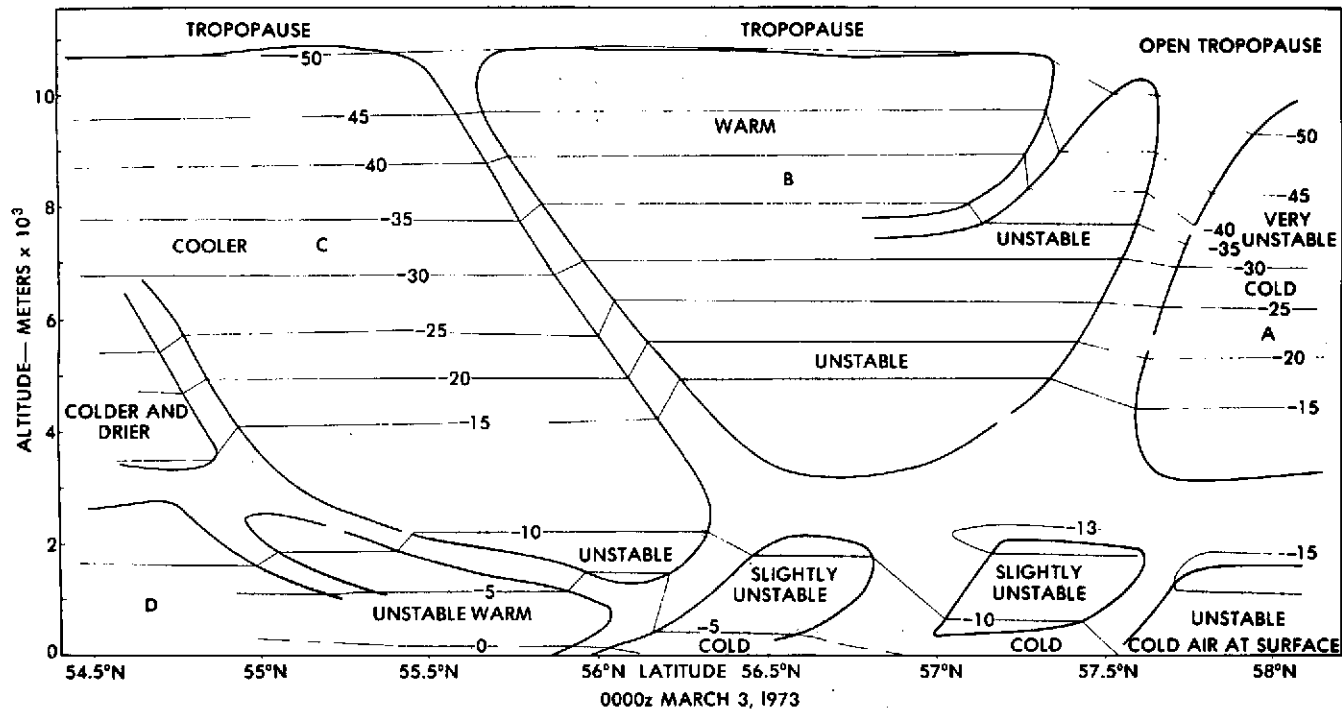Figure 5.1. Surface Chart for the BESEX Area 0000 GMT March 3, 1973

Figure 5.2. Air Masses Along the CV-990 Flight Track

Airmass Distributions

A - Cold and unstable air out ahead of upper level warm front.

B - Warm air advected in by primary system at upper levels. Now stopped because of primary system's vertical structure.

C - Cooler and slightly drier air coming in aloft, followed by even cooler air at high levels farther back (far left).

D - Modified air following passage of warm front occlusion.

ALTITUDE—METERS × 10^3

TROPOPAUSE   NO CLOUDS

OPEN TROPOPAUSE

10

THIN VEIL CIRRUS

CIRUS AND CIRRUS PATCHES

CIRROSTRATUS

8

THIN CIRROCUMULUS REGION

CIRROCUMULUS

THIN ALTOSTRATUS

6

COLDER AND DRIER AIR

ALTOSTRATUS OR NIMBOSTRATUS

CLEAR LAYER

4

ALTOCUMULUS (LAYERED)

THIN LAYERS OF ALTOCUMULUS (SEMI – TRANSPARENT)

2

STRATOCUMULUS AND CUMULUS

STRATOCUMULUS

STRATOCUMULUS MULTIPLE LAYERS

LOWER LEVEL CUMULUS (SHOWERS)

STRATUS FRACTUS   STRATUS FRACTUS

0

54.5°N   55°N   55.5°N   56°N LATITUDE 56.5°N   57°N   57.5°N   58°N
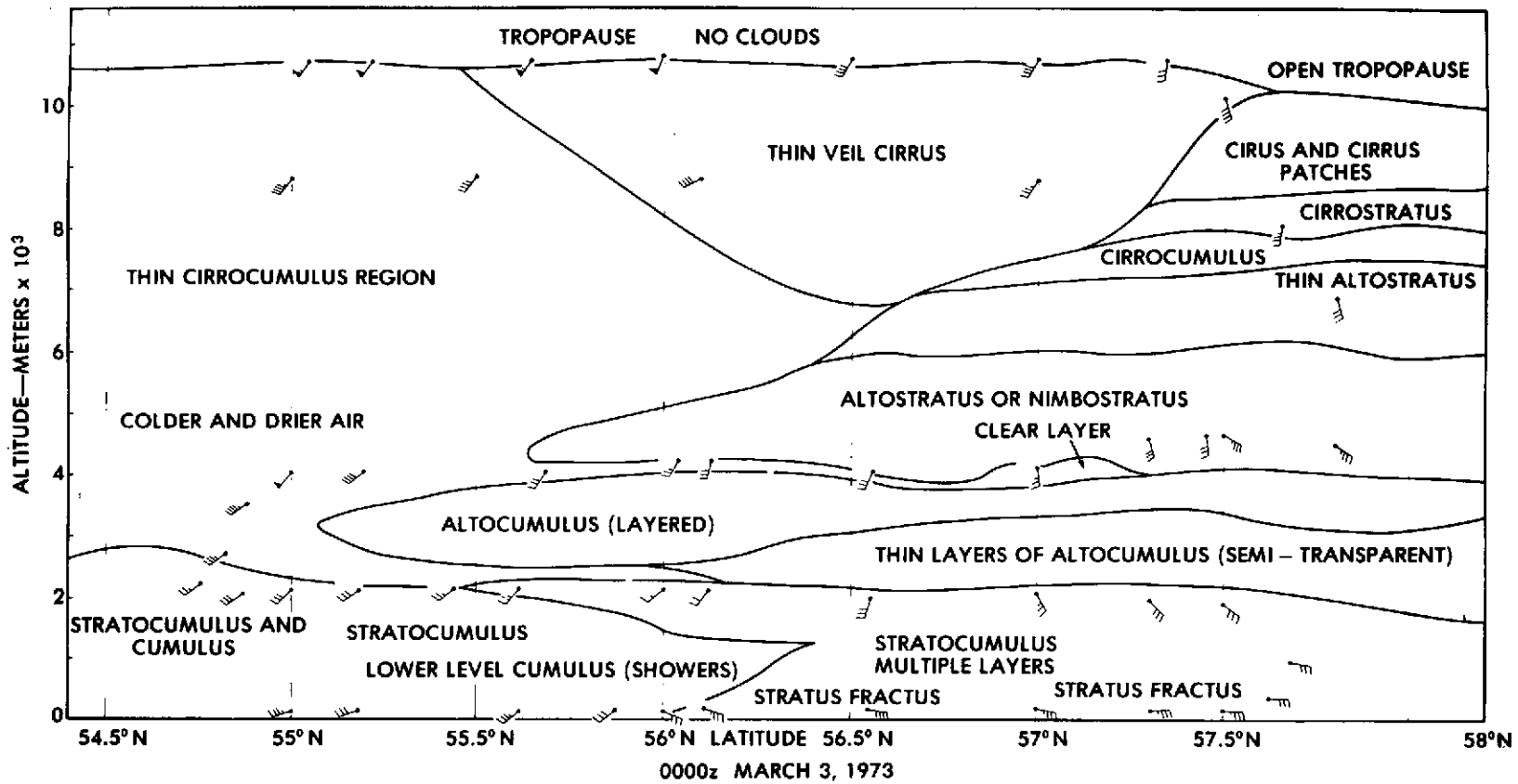
0000z MARCH 3, 1973

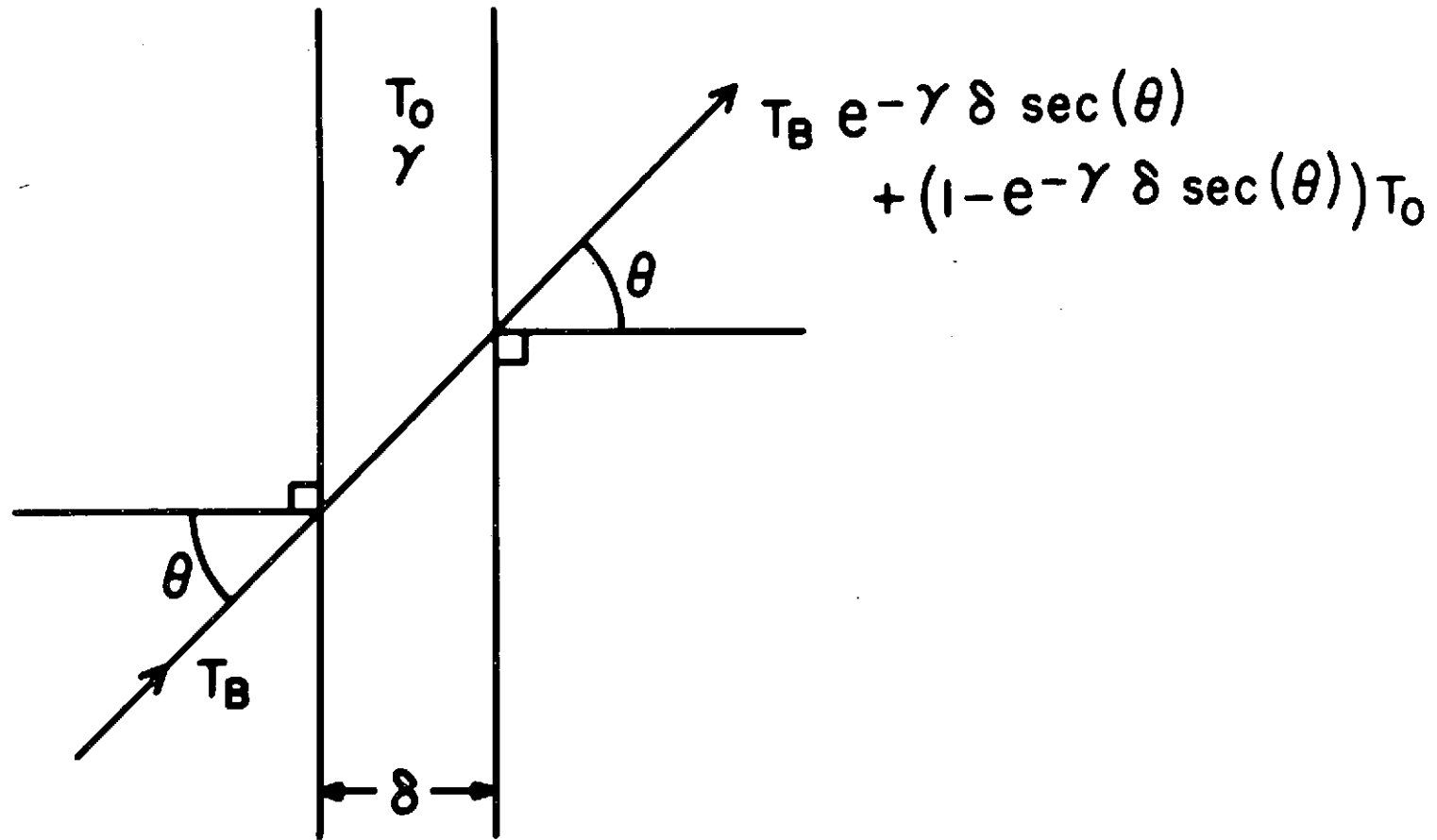Figure 5.3.   Clouds, Temperatures and Winds Along the CV-990 Flight Track

Figure 5.4. Effect of an Absorbing Slab on Microwave Brightness Temperatures
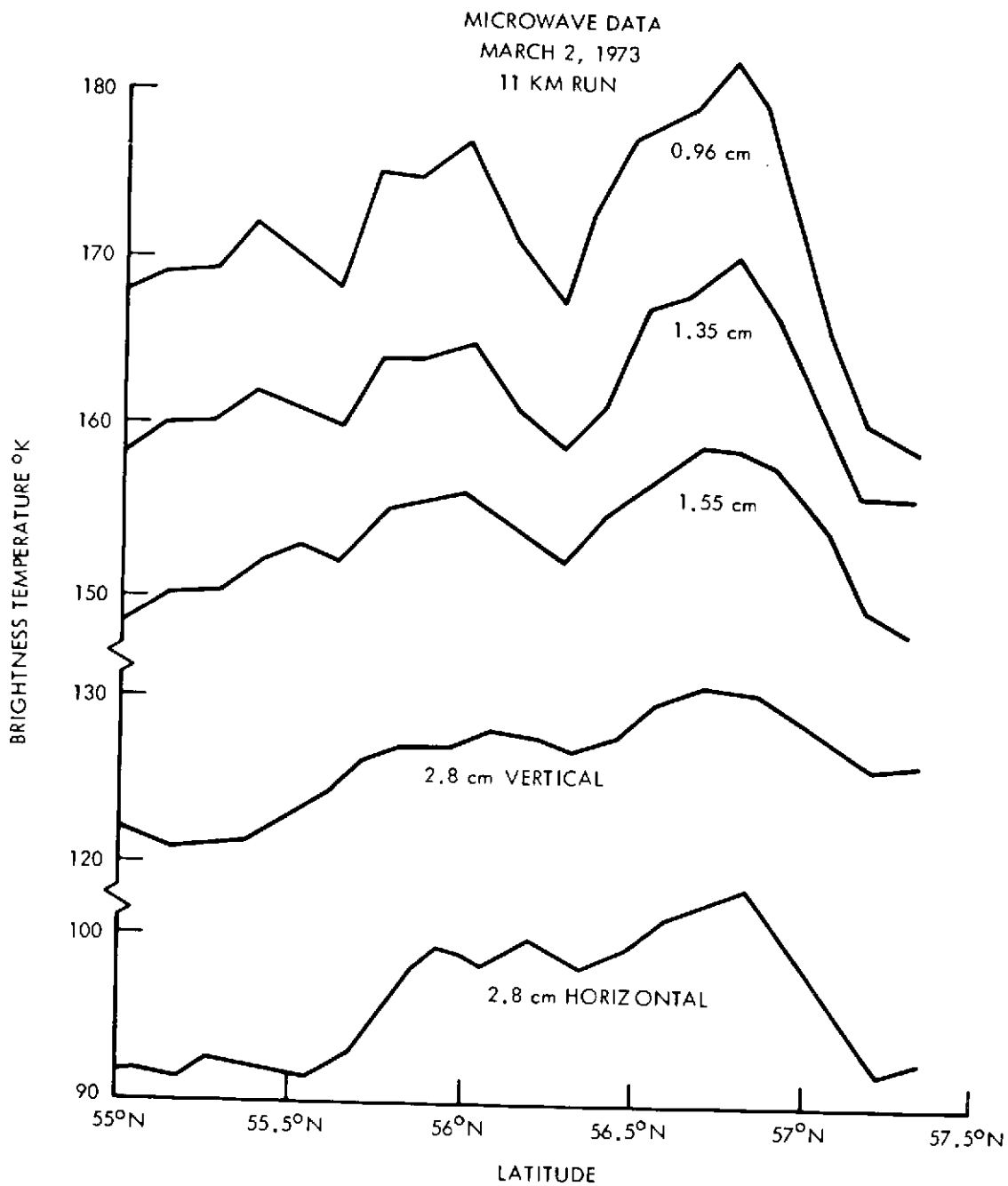
Figure 5.5. Downward Viewing Microwave Radiometer Measurements for the 11 km Run
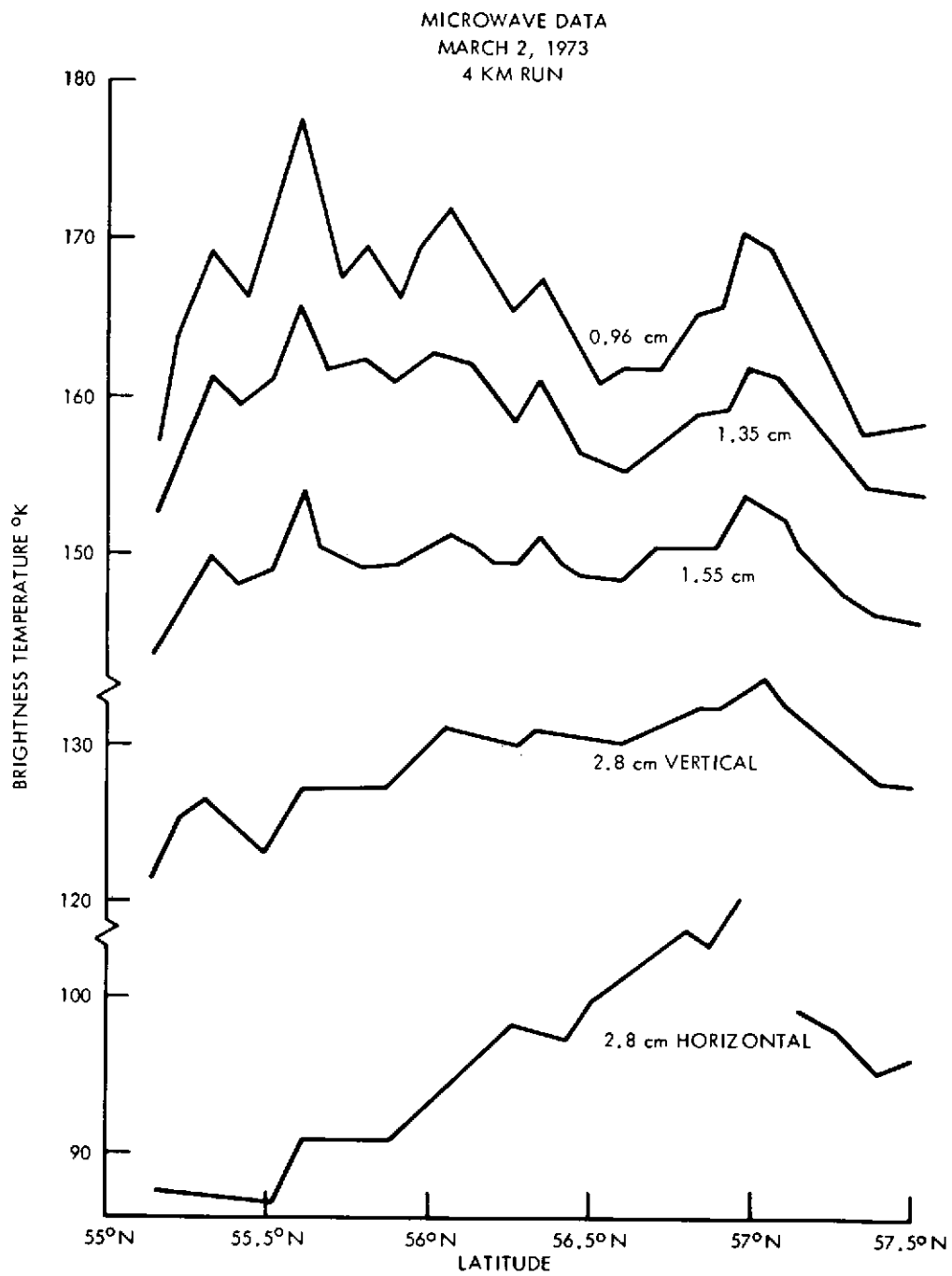
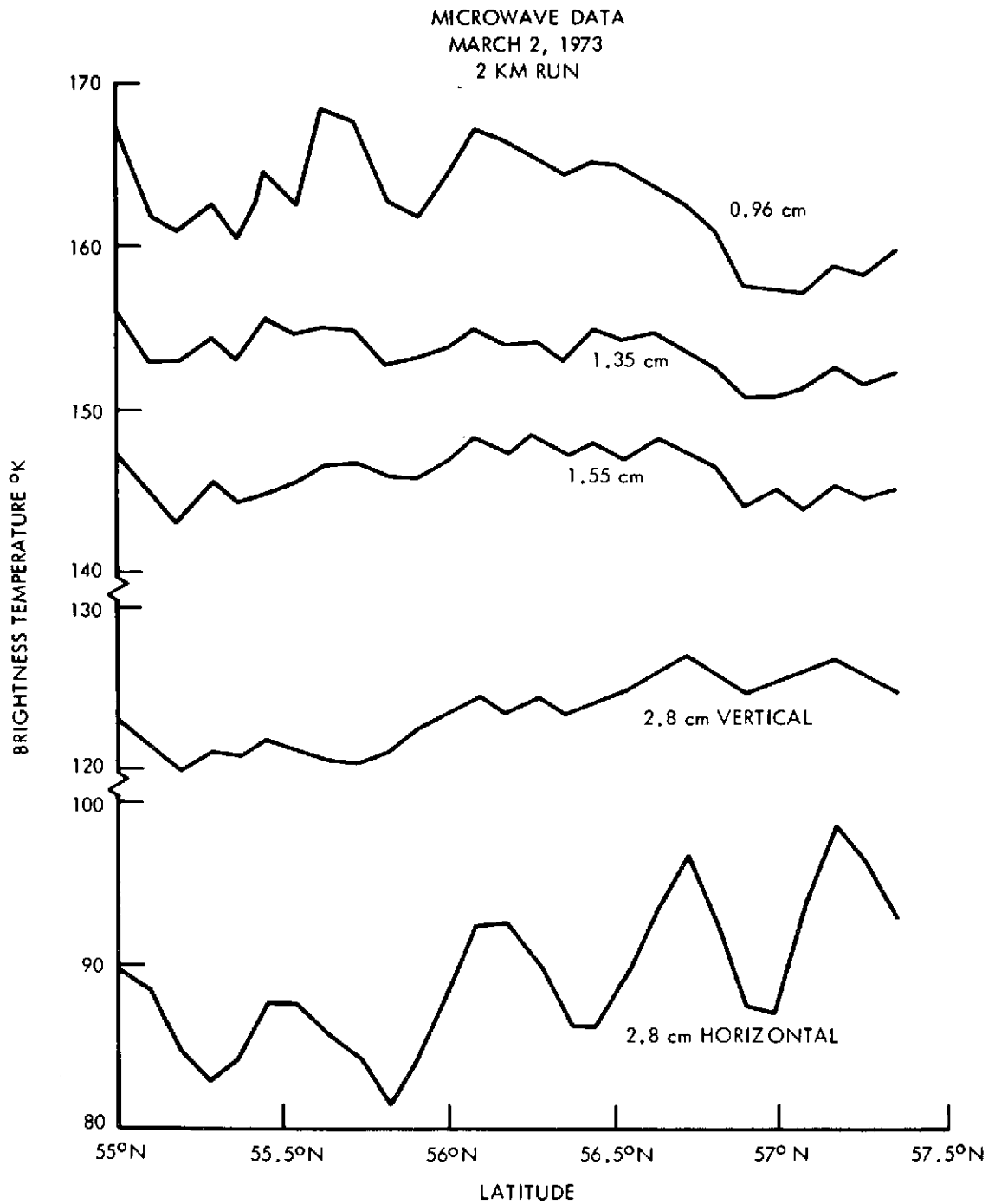Figure 5.6. Downward Viewing Microwave Radiometer Measurements for the 4 km Run

Figure 5.7. Downward Viewing Microwave Radiometer Measurements for the
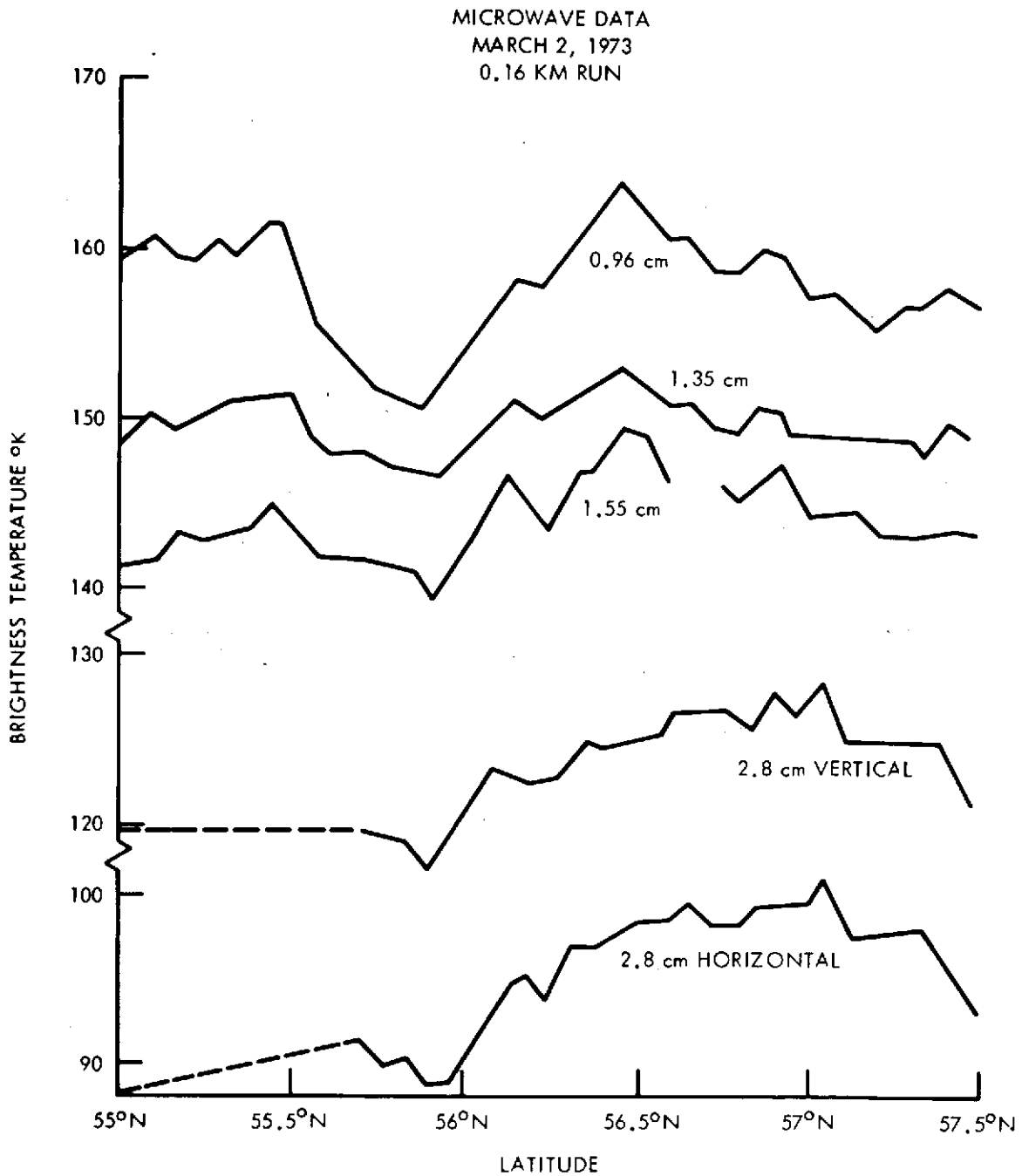2 km Run

Figure 5.8. Downward Viewing Microwave Radiometer Measurements for the 0.16 km Run
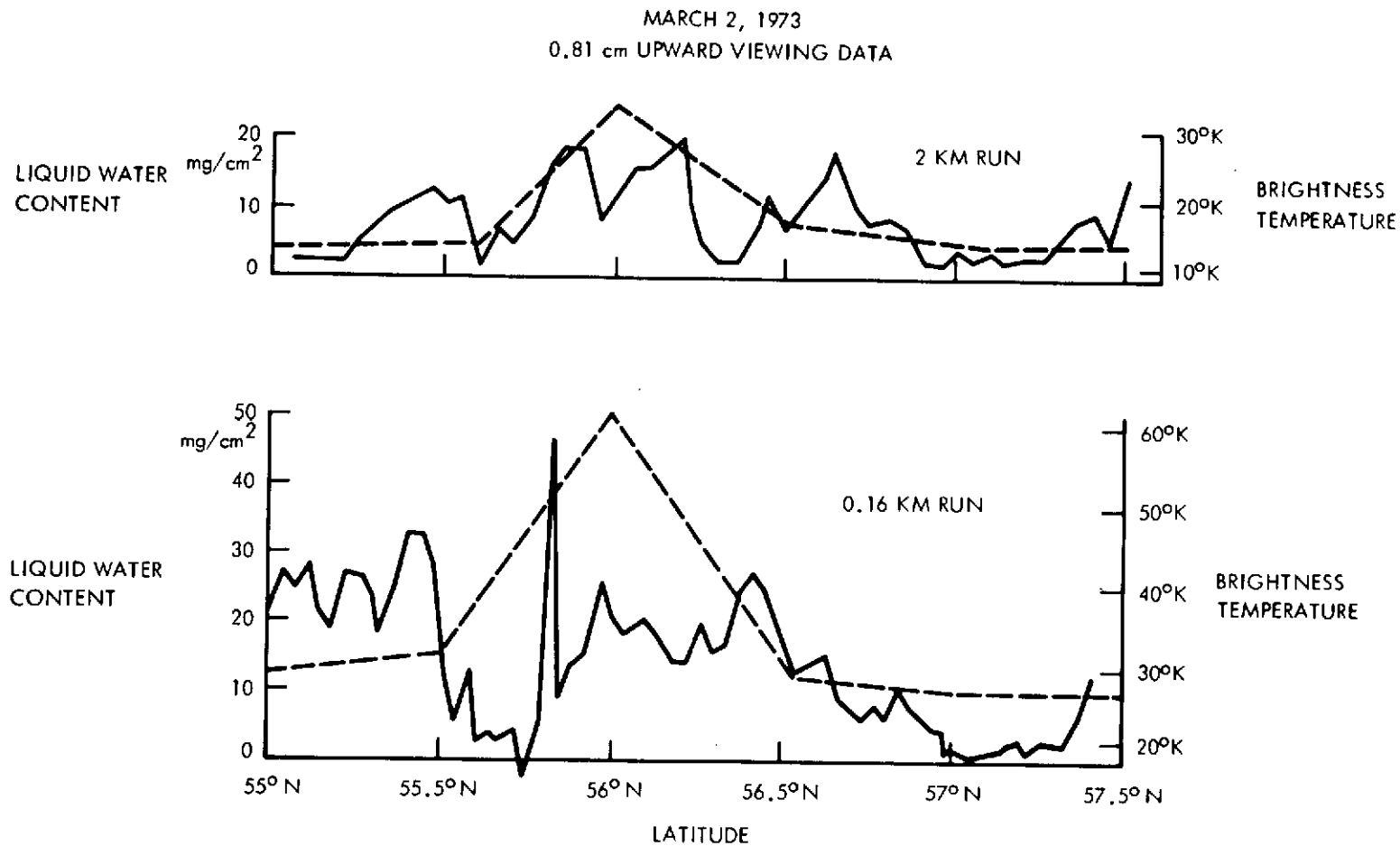
MARCH 2, 1973
0.81 cm UPWARD VIEWING DATA

Figure 5.9. 0.81 cm upward viewing radiometer measurements. The solid line is the radiometric data; the dashed line is the estimate of cloud liquid water based on the in situ observations.

Figure 5.10. Determinations of surface wind speed, cloud liquid water content and weighted water vapor content from the microwave measurements. 11 km run. The solid line results from 3 channel inversions, the X's from 5 channel inversions. The dotted line is an independent estimate based on meteorological observations.

161

MARCH 2, 1974
4KM RUN
INVERSION RESULTS

WIND SPEED

WEIGHTED WATER
VAPOR CONTENT

LIQUID WATER
CONTENT

Figure 5.11. Determinations of surface wind speed, cloud liquid water content and weighted water vapor content from the microwave measurements. 4 km run. The solid line results from 3 channel inversions, the X's from 5 channel inversions. The dotted line is an independent estimate based on meteorological observations.
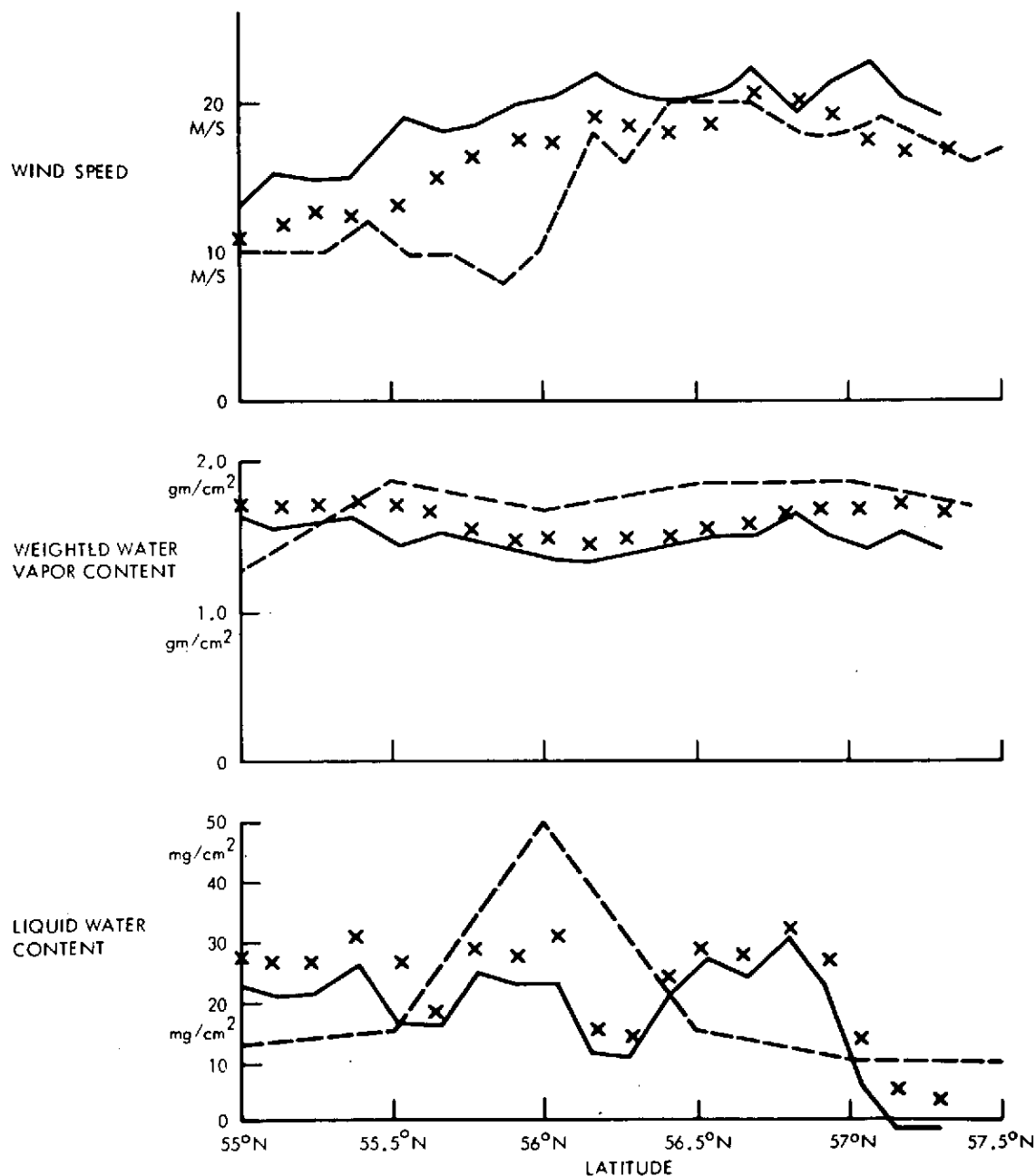
Figure 5.12. Determinations of surface wind speed, cloud liquid water content and weighted water vapor content from the microwave measurements. 2 km run. The solid line results from 3 channel inversions, the X's from 5 channel inversions. The dotted line is an independent estimate based on meteorological observations.
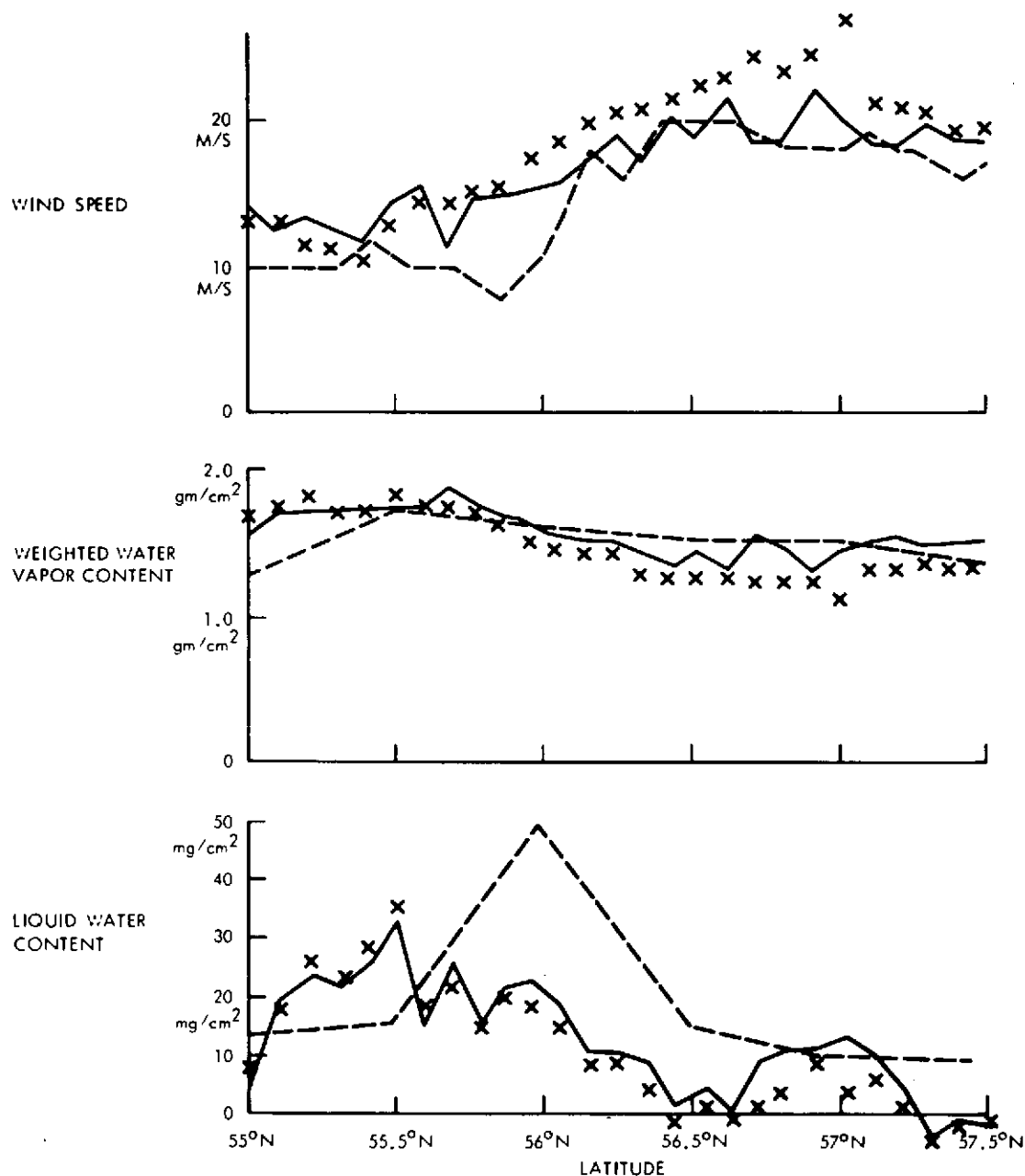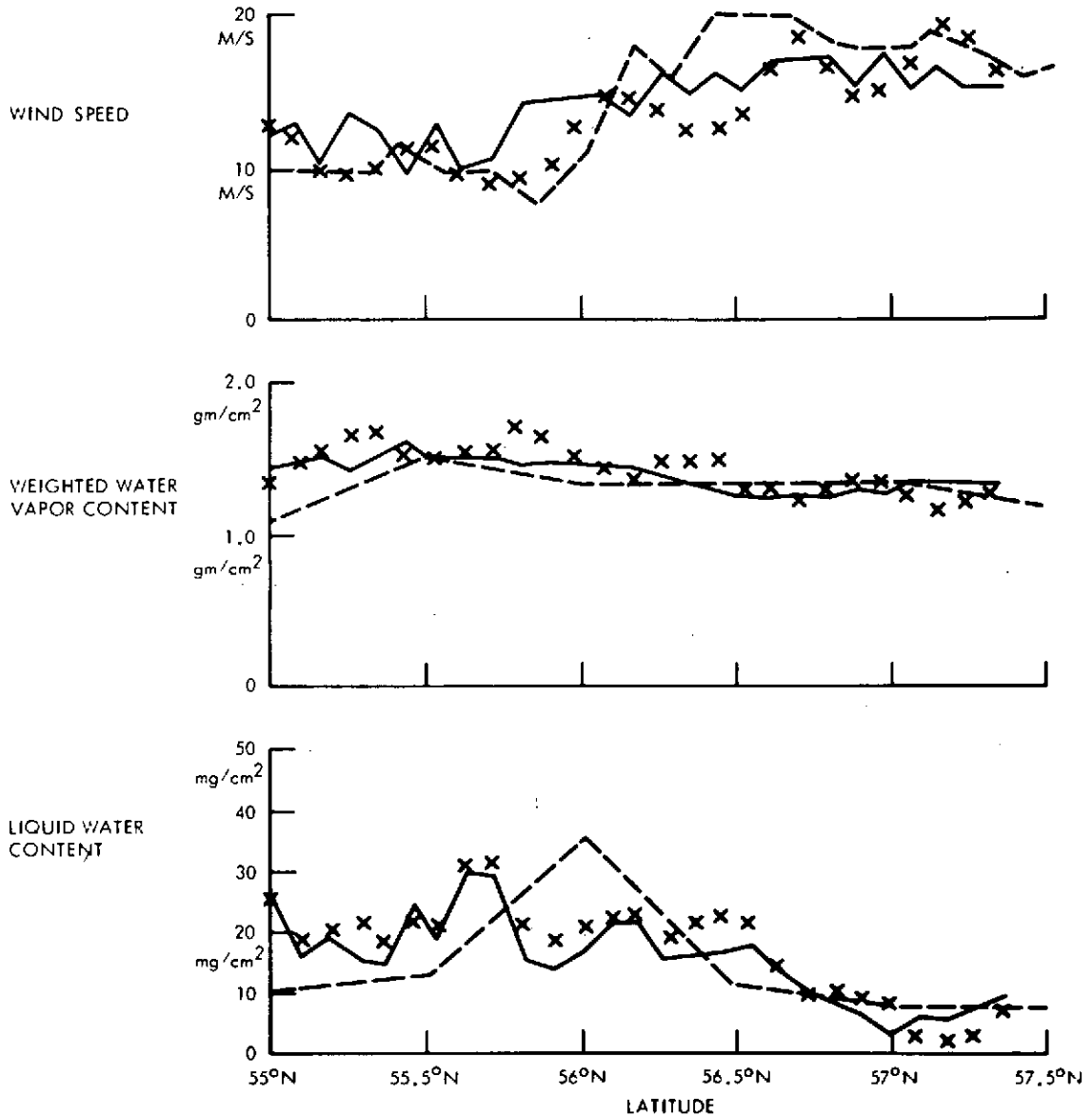
Figure 5.13. Determinations of surface wind speed, cloud liquid water content and weighted water vapor content from the microwave measurements. 0.16 km run. The solid line results from 3 channel inversions, the X's from 5 channel inversions. The dotted line is an independent estimate based on meteorological observations.

PAPER NO. 6

ANALYSIS OF THE CONVAIR-990 PASSIVE MICROWAVE OBSERVATIONS OF THE SEA STATES DURING THE BERING SEA EXPERIMENT

William J. Webster, Jr.*

Thomas T. Wilheit*

Duncan B. Ross[†]

Per Gloersen*

---

*National Aeronautics and Space Administration, Goddard Space Flight Center, Greenbelt, Maryland 20771

[†]National Oceanic and Atmospheric Administration, Atlantic Oceanographic and Meteorological Laboratories, Miami, Florida 33149

Paper No. 6

ANALYSIS OF THE CONVAIR-990 PASSIVE MICROWAVE
OBSERVATIONS OF THE SEA STATES DURING
THE BERING SEA EXPERIMENT

William J. Webster, Jr.

Thomas T. Wilheit

Duncan B. Ross

Per Gloersen

ABSTRACT

Observations of microwave brightness temperature made over the wavelength range from 21 cm to 0.81 cm show that the variation of brightness temperature with increasing wind speed is linear and is primarily a function of the percentage white water coverage. The frequency dependence of the wind speed sensitivities for winds greater than 10 m/s shows that the sea-air boundary layer (i.e. the white water layer) is a thin dielectric layer. The nadir angle dependence of the brightness temperature at 1.55 cm shows that, for horizontal polarization, the wind speed dependence becomes stronger as the angle of observation increases from nadir. The variation of brightness temperature with distance from the edge of the ice (fetch) shows that the brightness temperature decreases with decreasing fetch and that this change is primarily due to the decrease in areal coverage of thin foam streaks. A three-component model for the sea-air boundary layer based on the passive microwave observations is proposed.

ANALYSIS OF THE CONVAIR-990 PASSIVE MICROWAVE

OBSERVATIONS OF THE SEA STATES DURING

THE BERING SEA EXPERIMENT

6.1 INTRODUCTION

The Option A and B flights of the Convair-990 during the Bering Sea Experiment have provided data on the brightness temperature of the sea (T_B^{sea}) over a wide range of ocean conditions and over a wide span of wavelengths. In Table 6.1, the radiometers used in this study are listed. From these observations, we have deduced the wind speed sensitivity and the white water sensitivity of the individual wavelengths and polarizations.

Numerous aircraft and ocean platform observations have demonstrated the variation of T_B^{sea} with ocean surface conditions. Aircraft measurements at 1.55 cm by Nordberg et al (1969) suggested a strong variation of brightness temperature with increasing sea roughness. Subsequent observations (Nordberg, et al, 1971) showed that, above the critical wind speed for the formation of white caps (Munk, 1947), T_B^{sea} varies approximately linearly with wind speed and that this increase is due primarily to the change of the white water coverage. It was also suggested that there is a different dependence on wind speed for viewing angles off nadir. In an attempt to separate the white water influence from changes in wave structure, Hollinger (1970, 1971) made multi-frequency observations from an ocean platform. He specifically excluded actively breaking waves from his measurements. He concluded that, while horizontal polarization shows a substantial wind effect, there is only a very small effect for vertical polarization or near nadir observations.

167

In what follows, we show that the data obtained during the Bering Sea Experiment confirm and extend the results reported previously. We find that for nadir and vertical polarization observations the variation of white water coverage dominates the change in observed brightness temperatures. The data permits a determination of some of the properties of the boundary layer between the water and the air. The data also show the influence of fetch when high wind speeds must be considered. It is apparent that a neglect of fetch in the reduction of observations can contribute an important error in the implied wind speed.

6.2 THE VARIATION OF BRIGHTNESS TEMPERATURE
WITH WIND SPEED

We have examined the variation of T_B^{sea} with wind speed ($\bar{U}_{155}$) measured at 155 m aircraft altitude for each wavelength and polarization for wind speeds greater than 10 m/s and under fully developed conditions. In order to reduce the importance of transient features, the observations were averaged over periods much longer than the time constants of the radiometers, typically 4 minutes. To minimize the contribution from the atmosphere below the aircraft and to avoid a contribution from aircraft reflections, only data taken at about 155 m altitude were used.

The component of the atmospheric emission (T_B^{sky}) reflected from the ocean surface makes an important systematic contribution to the observed T_B^{sea}. We have made use of simultaneous measurements of T_B^{sky} at 0.81 cm to remove the reflected sky component from the down-viewing measurements. T_B^{sky} for each frequency was obtained by assuming the sky brightness temperature was determined by clouds and therefore scaling the 0.81 cm measurement by a square law dependence on wavelength. This scaling appears to be good except

near the water vapor resonance at 1.35 cm. Mean reflectivities were calculated using the Fresnel equations, the dielectric constant data of Lane and Saxton (1952) and assuming a specular sea. A sea temperature of 0°C was assumed. The assumptions made in this calculation should not make an error of more than 0.5°K in the reflected T_B^{sea} calculation at 0.81 cm, less at longer wavelengths. It should be noted that the specular sea assumption is equivalent to assuming that large angle scattering is unimportant for all wind speeds. This assumption will be less accurate at the higher wind speeds.

The corrected data are the products of the surface emissivity and thermodynamic temperature. These data, weighted directly by the number of minutes in the averages, were fit to a line by the method of least squares. Table 6.2 presents the slopes of the least squares lines and the formal standard error of the slopes. Examples of these curves are given in Figures 6.1 and 6.2. Figure 6.1 gives T_B^{sea} vs $\overline{U}_{155}$ for 1.55 cm, nadir, and 38° horizontal and for 21 cm. Figure 6.2 gives 0.81 cm H and V and 6.0 cm H and V. Each figure also contains the result of a 6 minute average from 23/24 February when the wind speed was very low (5.1 m/s) and there was virtually no white water present. These low wind speed points were not included in the analysis but indicate the difference in the wind speed effect for wind speeds above and below 7 m/s.

In Figure 6.3, we plot the slopes of the T_B^{sea} vs $\overline{U}_{155}$ curves as a function of frequency. Note that a smooth curve passing through the nadir and vertical polarization measurements would rise from 1.4 GHz (21 cm) to roughly 11 GHz (2.7 cm). Theoretical studies (Stogryn, 1967, Wu and Fung, 1972) as well as Hollinger's (1970, 1971) experimental results indicate that the nadir and vertical polarization data should represent primarily a white water effect. The horizontal

169

polarization data combine the white water effect with a substantial roughness contribution.

Figure 6.4 gives the calculated emissivity curve whose shape is consistent with the sensitivity curve of Figure 6.3. The emissivity curve was calculated assuming that the index of refraction of the sea-air boundary layer, which we identify with the white water, varies linearly from the value for water to that for air in a distance of 1.5 mm. The calculation was performed by dividing the interface layer into 100 steps and solving the boundary value problem for each edge in succession. The actual depth of the layer is most important in determining the rise in the sensitivity curve of Figure 6.3.

The 1.5 mm layer depth is very small compared to the apparent depth of sea foam and it is of interest to speculate on its physical significance. Laboratory measurements (Williams, 1971) and theoretical calculations (Droppleman, 1970) show that scattering or attenuation within the foam is unimportant. These studies suggested that the most important factor is the distortion of the water surface at the interstices of the bubbles. Thus the 1.5 mm depth refers to the region immediately above the ocean surface where sea water is being lifted by surface tension or turbulent processes.

6.3 POLARIZATION AND ANGLE DEPENDENCE OF T_B^{sea}

Because of the presence of white water and the change of wave structure, the angular dependence of the emission from a smooth sea is different from that for a rough, foamy sea. Data from the 1.55 cm scanning radiometer, which covers nadir angles from 0° to 50°, illustrates this. In Figure 6.5, we plot the angle dependence of T_B^{sea} for a low wind speed case (23/24 February) and a high wind speed case (7/8 March). These measurements were corrected for

reflected sky emission as described above. Note that the decrease of brightness temperature with nadir angle is much greater for the low wind speed case. The presence of roughness and white water in the high wind speed case has decreased the angle dependence as well as increased the T_B^{sea} at nadir.

Theoretical calculations of the emission from a rough but not foamy sea show that the dependence on changing wave structure is greater for horizontal polarization (Wu and Fung, 1972). In agreement with these predictions, Table 2 shows that the slopes of the T_B^{sea} vs wind speed curves are highest for horizontal polarization. Because the white water signature is only weakly polarized and since the wave contribution is negligible for vertical polarization, the increase in the slope for the horizontal polarizations over the slope for vertical polarization is due to changing wave structure. This increase is in approximate agreement with the foam-free measurements (Hollinger, 1971). Further, the residual slope follows the predicted trend of increasing toward higher frequencies (Wu and Fung, 1972).

6.4 THE INFLUENCE OF FETCH, WAVE STRUCTURE AND WHITE WATER VARIATION

During the flights of 23/24 February and 7/8 March, we obtained extensive observations at low (about 155 m) altitude. In each case, approximately one hour of data was obtained along a track at an angle of about 30° to the edge of the ice from a point about 300 km seaward to slightly north of the ice edge.

The flight of 23/24 February was made under conditions of light (about 5 m/s) winds. The radar survey made by the USSR aircraft indicates some swell and very little wind wave activity within the test area at this time (Martsinkevitch, L. M., 1973, Personal Communication). The microwave data

171

shows little or no change as the aircraft approached the edge of the ice. Figures 6.6 and 6.7 show one minute averages for several of the radiometers during this period. Note that the data are corrected for reflected sky emission as described previously.

As the edge of the ice is approached, there does appear to be a very slight change in T_B^{sea} at each frequency. The observed infrared temperature of the sea surface decreases by about three degrees during this period, which is adequate to account for the change in T_B^{sea}. Note that the decrease in the thermodynamic temperature causes an increase in the brightness temperature at 0.81 cm. This is because the emissivity is a function of temperature and at 0.81 cm decreases fast enough with increasing temperature that $d(eT_s)/dT_s < 0$. The results are summarized in Table 6.3. The calculated temperature sensitivities are based on the Lane and Saxton (1952) dielectric constant measurements, while the observed sensitivities were determined by a least squares analysis of T_B^{sea} as a function of the infrared temperature corrected for aircraft altitude. The table confirms the predicted trend and shows that the highest sensitivity to surface temperature is for 6.0 cm, vertical polarization.

The flight of 7/8 March yielded the highest wind speeds and foam coverages observed during the joint experiment. Table 6.3 gives the white water coverage obtained from nadir camera observations using the method of Ross and Cardone (1974). The table also gives the wind speed at 20 m altitude assuming a logarithmic profile (Cardone, 1969) between the aircraft and the sea and using the wind speeds determined from the aircraft inertial navigation system at about 155 m altitude averaged over one minute.

As the table shows, the total white water coverage begins to decrease after approximately 00^h14^m. The percentage of white caps remains roughly constant over most of the interval and it is primarily the steaks which decreased. During the same interval, the winds at 20 m altitude rose from 22.6 m/s to 24.7 m/s. The infrared temperature remains constant at about +0.5°C until severe spray and precipitation invalidate the measurements. Based on the 23/24 February data, we do not expect an ocean surface temperature gradient of more than 3°C from the beginning of the 155 m track to the ice edge.

The USSR radar survey of the area (Belousov et al, 1973) showed that wind waves were dominant over swell during the March 7/8 flight. Since the wind was blowing nearly perpendicular to the ice edge, the 155 meter track was obtained for a fetch which decreased continuously from about 250 km to 0 km. This changing fetch yielded changes in the wave structure and the white water in a measurable way. Therefore, we can use the polarization properties of the emission from the sea to separate the dependence on white water from the dependence on waves.

In Table 6.4, we give the sensitivities of T_B^{sea} to observed white water. The sensitivities were determined by a least squares analysis of the corrected T_B^{sea} for each wavelength and polarization as a function of the total white water coverage observed photographically. The nadir and vertical polarization sensitivities follow a similar wavelength dependence to the wind speed sensitivities. In this case, the data show the properties of the sea-air boundary layer without the confusion of a large change in wind speed.

The total white water values from Table 6.3 have been plotted in Figure 6.8. Note the essentially linear relationship between fetch and percentage white water

173

at least up to 250 km (00^h04^m). Similarly, some of the T_B^{sea} measurements are also plotted in Figures 6.8 and 6.9. Although the visible white water percentage changed by about 40%, only 3% being due to actively breaking waves, the largest decrease in T_B^{sea} is about 5°K. That is about half of the wind and foam effects remained at the zero fetch limit even though the visible white water had nearly disappeared (except at 21 cm). This suggests that aircraft photographic measurements of the visible white water cannot determine the total contribution to T_B^{sea} in a fetch limited case. Some of the white water contributing to T_B^{sea} may not be visible photographically. Alternatively, the decrease in white water may be balanced by an increase in the short wave contribution.

During the 155 meter pass, the surface winds ($\bar{U}_{20}$) rose from 22.6 to 24.7 m/s as the aircraft approached the ice. If we ignore fetch, rising wind speed would contribute an increase of about 2°K for horizontal polarization over the period of the decreasing white water observations. Since the white water coverage changed by about 40%, this wind speed change would appear as a white water sensitivity of -0.05°K/percent. If we also ignore the very small roughness effect predicted for vertical polarization (Wu and Fung, 1972), the combination of the vertical polarization measurements and the wind speed rise predict a horizontal polarization sensitivity of about 0.05°K/percent. This is as observed except for 0.81 cm.

We speculate that the short waves, which are important for the wave slope influence on T_B^{sea}, should be fully developed almost immediately. If so, the data indicate a decrease in at least part of the amplitude spectrum of the short gravity and capillary waves with increasing fetch. The decrease seems to be in response to the variation of the wind speed with fetch. This is consistent with

the results of Hasselman et al (1973), who attributed the observed reduction
of high frequency wave energy with increasing fetch to non-linear interactions
with the longer growing waves.

6.5 DISCUSSION

From analysis of the Convair-990 observations, we find:

1. The variation of T_B^{sea} with wind speed $(\overline{U}_{155})$ is linear between 11 m/s
   and 27 m/s under fully developed conditions. Below the critical wind
   speed for the formation of white water, the data suggest a variation with
   a much smaller slope.

2. The nadir angle dependence of T_B^{sea} at 1.55 cm shows that the strength
   of the wind speed effect increases as the nadir angle increases.

3. The low wind speed observations show no dependence on fetch, while the
   high wind speed observations show that T_B^{sea} varies through the change
   in white water coverage and wave structure with fetch.

4. The frequency dependence of the wind speed sensitivities and of the white
   water sensitivities is consistent with a model in which the sea-air
   boundary layer is a dielectric layer about 1.5 mm thick.

Very limited observations have suggested that white caps have a different
emissivity from streaks (Nordberg et al, 1971; Ross et al, 1970). Observa-
tions of simulated foam (Williams, 1971) and calculations of the emissivity of
a foam layer as a function of depth (Droppleman, 1970) support this suggestion.
The Convair-990 microwave data do not allow us to directly separate the white
caps from the streaks in an unambiguous way, however.

Since the white cap coverage was only about 5% over the bulk of the 7/8
March observations, even a unit emissivity for the white caps would not account

175

for the effect observed at wavelengths shorter than 6 cm. The important part of the white water for the short wavelength microwave observations must be the thin streaks. In many cases, the streaks are so thin as to escape photographic detection.

Thus, the following model (see Figure 6.10) emerges: the interface between the sea and the air is a dielectric layer with thick spots (several cm), thin spots (about 1.5 mm) and voids. The thick spots correspond to the white caps and the thin spots correspond to the streaks. The total area covered by the thick and thin spots increases as the wind speeds increases; the total area of the thin spots in much greater than the thick spots. In addition to the change of the areal coverage of the white water components with wind speed, the small scale roughness of the sea increases at least up to 23 m/s for fully developed seas. The small scale roughness spectrum, however, appears to be fetch dependent, decreasing with increasing fetch.

ACKNOWLEDGMENT

BIBLIOGRAPHY

Belousov, P., Zhilko, E. O., Zagorodnikov, H. H., Kornienko, V. I., Loshchidov, V. S. and Chel'shev, K. B., 1973, in Results of the Soviet-American Experiment, A. I. Voyeykov Main Geophysical Observatory, Leningrad, USSR.

Cardone, V. J., 1969, Rep. TR69-1, Geophys. Sci. Lab. N.Y.U.

Droppleman, J. D., 1970, J.G.R., 75, 696.

Hasselman, K., Barnett, T. P., Bouws, E., Carlson, H., Cartwright, D. E., Enke, J. A., Grenapp, H., Hasselman, D. E., Kruseman, P., Meerburg, A., Müller, P., Olbers, D. J., Richter, K., Sell, W., and Walden, H., 1973, Engänzungsheft zur Deutschen Hydrographischen Zeitschrift, Reih A Nr 12, Deutsches Hydrographisches Institut, Hamburg, BDR.

Hollinger, J. P., 1970, J.G.R., 75, 5209.

Hollinger, J. P., 1971, I.E.E.E. Trans. Geosci. Elect., GE-9, 169.

Lane, J. and Saxton, J., 1952, Proc. Roy. Soc., A213, 531.

Munk, W. H., 1947, Journ. Marine Res., 6, 203.

Nordberg, W., Conaway, J. and Thaddeus, P., 1969, Q.J.R. Meteor. Soc., 95, 408.

Nordberg, W., Conaway, J., Ross, D. B., and Wilheit, T. T., 1971, J. Atmos. Sci., 28, 429.

Ross, D. B., Cardone, V. J., and Conaway, J. W., Jr., 1970, I.E.E.E. Trans. Geosci. Elect., GE-8, 326.

Ross, D. B. and Cardone, V., 1974, J.G.R., 79, 444.

Stogryn, A., 1967, I.E.E.E. Trans. Ant. Prop., AP-15, 278.

Williams, G., Jr., 1971, I.E.E.E. Trans. Geosci. Elect., GE-9, 24.

Wu, S. T. and Fung, A. K., 1972, J.G.R., 77, 5917.

Table 6.1

Microwave Radiometers Used in Sea State Study

Wavelength	Frequency	Polarization	Nadir Angle	Sensitivity
21.0 cm	1.42	Nadir	0°	2.5°K (1 second)
6.0 cm	4.99	Vertical	38°	2.0°K (1 second)
6.0 cm	4.99	Horizontal	38°	10.0°K (1 second)
2.8 cm	10.69	Vertical	38°	3.0°K (1 second)
2.8 cm	10.69	Horizontal	38°	3.0°K (1 second)
1.55 cm	19.35	Horizontal	scanner	2.0°K (47 ms)
0.95 cm	31.4	Nadir	0°	0.3°K (1 second)
0.81 cm	37.0	Vertical	38°	2.4°K (1 second)
0.81 cm	37.0	Horizontal	38°	2.4°K (1 second)
0.81 cm	37.0	Zenith	115°	0.9°K (1 second)

Table 6.2

Measured Slopes of Wind Speed vs. Brightness Temperature Curves

Wavelength (cm)	Polarization	Slope $\left(\dfrac{°K}{\text{meter per second}}\right)$
21.0	Nadir	0.205 ± 0.051
6.0	V – 38°	0.450 ± 0.056
6.0	H – 38°	0.989 ± 0.095
2.8	V – 38°	0.659 ± 0.172
2.8	H – 38°	1.180 ± 0.042
1.55	Nadir	0.860 ± 0.103
1.55	H – 12°	0.931 ± 0.126
1.55	H – 24°	0.999 ± 0.075
1.55	H – 38°	1.016 ± 0.097
0.95	Nadir	0.739 ± 0.095
0.81	V – 38°	0.535 ± 0.087
0.81	H – 38°	1.257 ± 0.293

Table 6.3

Comparison of Observed and Predicted Temperature Dependence

Wavelength (cm)	Polarization	$\dfrac{\Delta T_B}{\Delta T_s}$ Observed	$\dfrac{\Delta T_B}{\Delta T_s}$ Predicted
21.0	N	0.3 ± 0.4	-0.05
6.0	V – 38°	0.8 ± 0.6	$+0.5$
6.0	H – 38°	3.8 ± 3.7	$+0.3$
2.8	V – 38°	0.8 ± 0.7	$+0.4$
2.8	H – 38°	1.4 ± 1.5	$+0.2$
1.55	N	0.5 ± 0.7	$+0.02$
0.95	N	-0.6 ± 0.4	-0.02
0.81	V – 38°	-2.4 ± 1.7	-0.3
0.81	H – 38°	-1.2 ± 0.8	-0.3

Table 6.4

White Water Analysis 7/8 March Low Pass

Time (GMT)	White Caps (%)	White Caps and Streaks (%)	20 m Wind Speed (m/s)	Time (GMT)	White Caps (%)	White Caps and Streaks (%)	20 m Wind Speed (m/s)
0000:00	2.9	35.2	22.6	0020:00	12.1	24.6	
0001:00	1.4	28.8		0021:00	8.0	20.1	
0002:00	4.6	35.0		0022:00	2.0	12.4	
0003:00	6.2	37.0		0023:00	6.0	21.6	23.7
0004:00	6.0	42.2	22.6	0024:00	3.4	22.7	
0005:00	2.5	40.4		0025:00	2.3	25.2	
0006:00	2.5	37.5		0026:00	1.4	11.4	24.2
0007:00	1.7	36.7		0027:00	2.5	14.3	24.2
0008:00	2.0	30.9	22.6	0028:00	2.1	11.5	
0009:00	2.6	44.6		0029:00	1.9	15.0	
0010:00	8.2	36.3	22.6	0030:00	2.3	10.5	
0011:00	4.3	39.7		0031:00	3.1	7.7	
0012:00	1.6	40.5		0032:00	1.8	5.4	24.2
0013:00	3.7	37.7	22.6	0033:00	1.85	6.4	
0014:00	1.3	28.5		0034:00	1.9	12.2	
0015:00	7.3	25.5		0035:00	2.6	3.7	
0016:00	5.2	31.7		0036:00	3.9	8.1	
0017:00	0.5	26.0	22.6	0037:00	3.0	4.4	24.2
0018:00	1.2	22.5		0038:00	1.0	1.0	
0019:00	2.1	27.0		0039:00	1.9	1.8	
				0040:00	2.2	7.6	24.7
				0041:00	1.5	2.9	
				0041:30	3.0	13.8	
				0043:00	6.2	15.5	24.7
				0047:00	2.0	2.0	
				0048:00	4.5	5.1	
				0049:00	5.0	4.1	

Table 6.5

Variation of T_B^{sea} with White Water Coverage

Wavelength (cm)	$\dfrac{\triangle T_B}{\triangle \text{ White Water}} \left(\dfrac{°K}{\text{percent}}\right)$
21.0	-0.068 ± 0.100
6.0 V – 38°	$+0.102 \pm 0.090$
6.0 H – 38°	$+0.047 \pm 0.030$
2.8 V – 38°	$+0.135 \pm 0.080$
2.8 H – 38°	$+0.082 \pm 0.070$
1.55	$+0.081 \pm 0.050$
0.95	$+0.063 \pm 0.050$
0.81 V – 38°	$+0.102 \pm 0.060$
0.81 H – 38°	$+0.116 \pm 0.060$
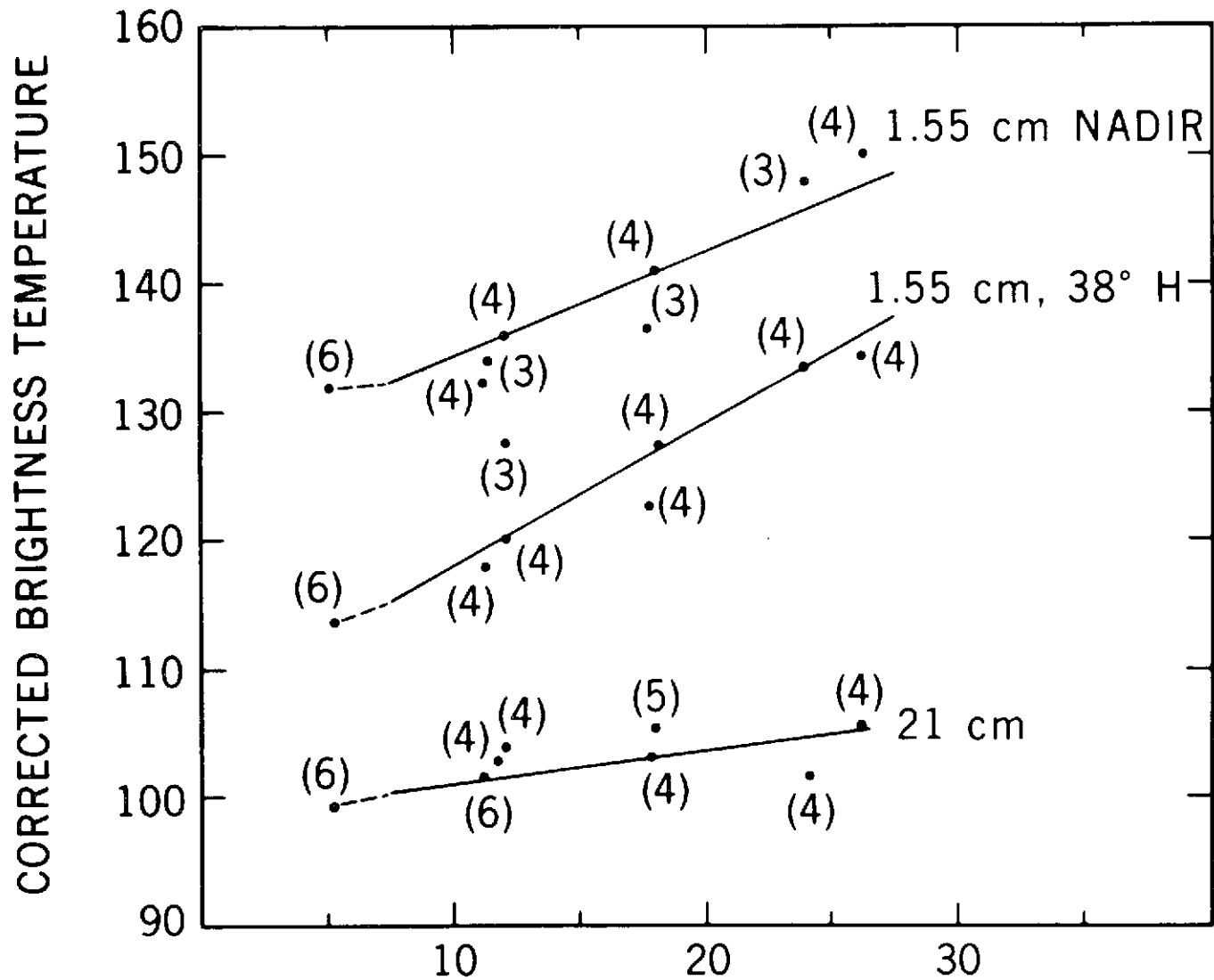
Figure 6.1. T_B^{sea} vs. Wind Speed ($\overline{U}_{155}$): 21 cm, 1.55 cm Nadir and 1.55 cm Horizontal
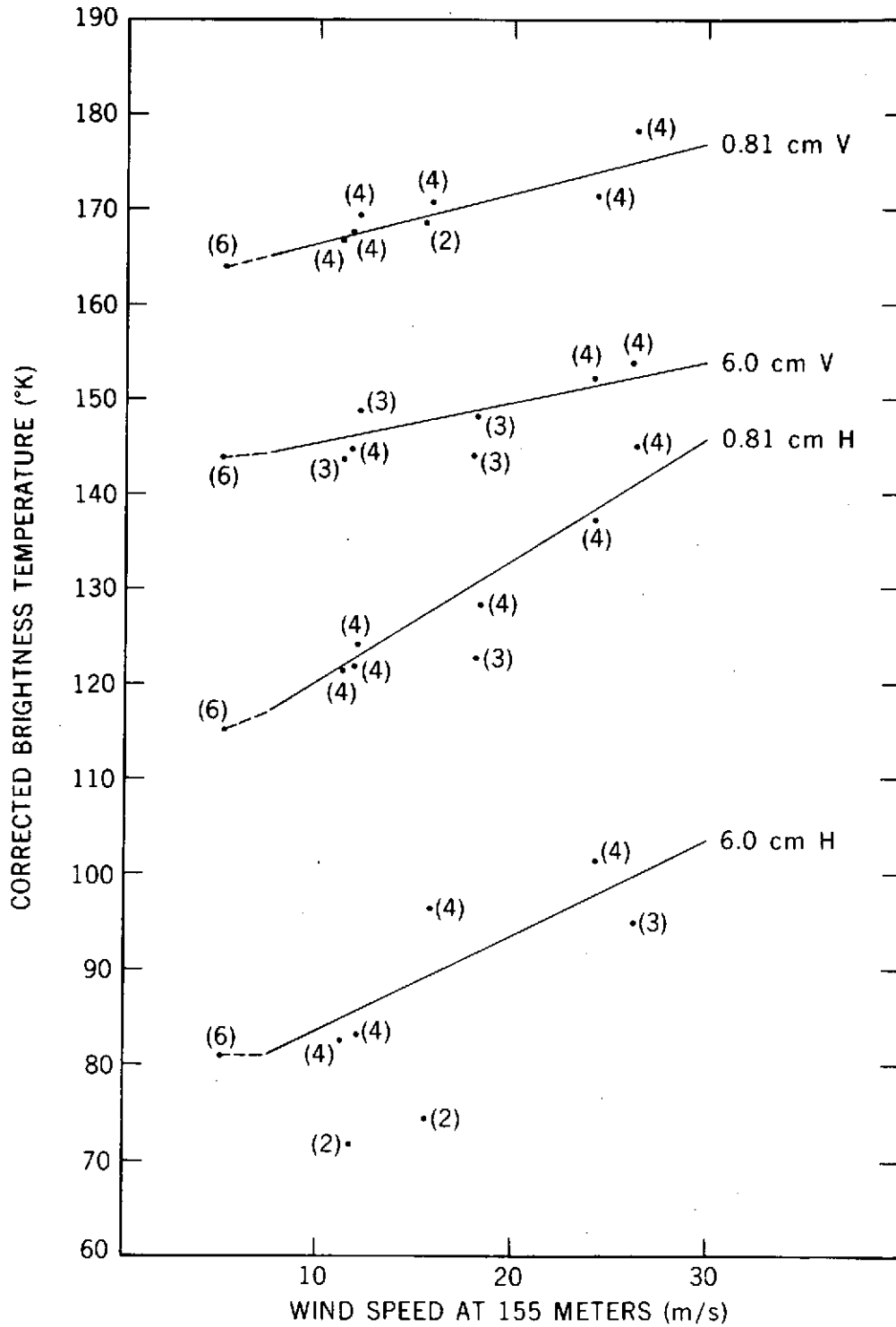
Figure 6.2. T_B^{sea} vs. Wind Speed ($\overline{U}_{155}$): 0.81 cm V and H and 6.0 cm V and H

T_B AS A FUNCTION OF WIND SPEED: SLOPE VS FREQUENCY
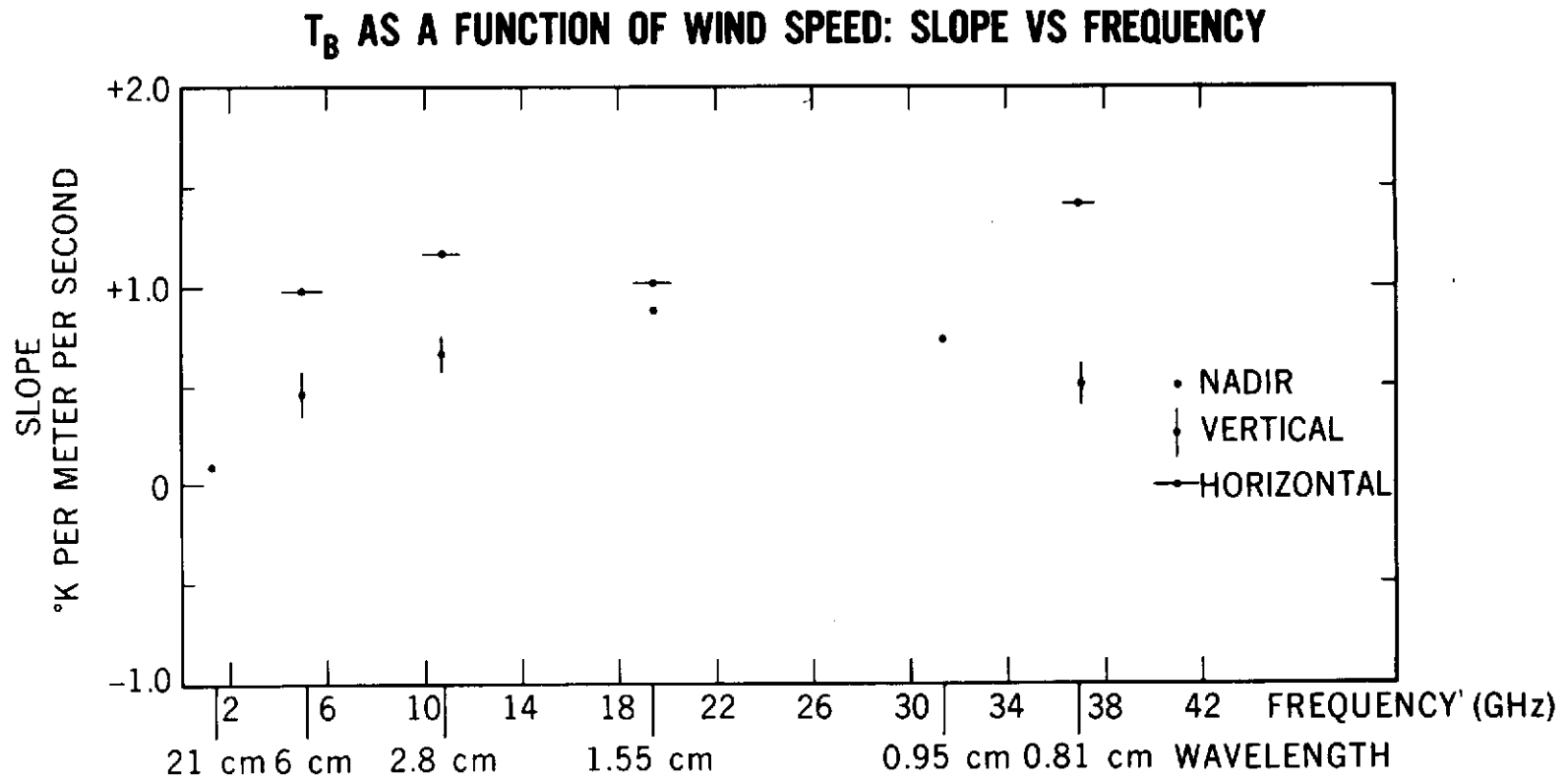
Figure 6.3. Slopes of T_B^{sea} vs. Wind Speed Curves as a Function of Frequency and Wavelength
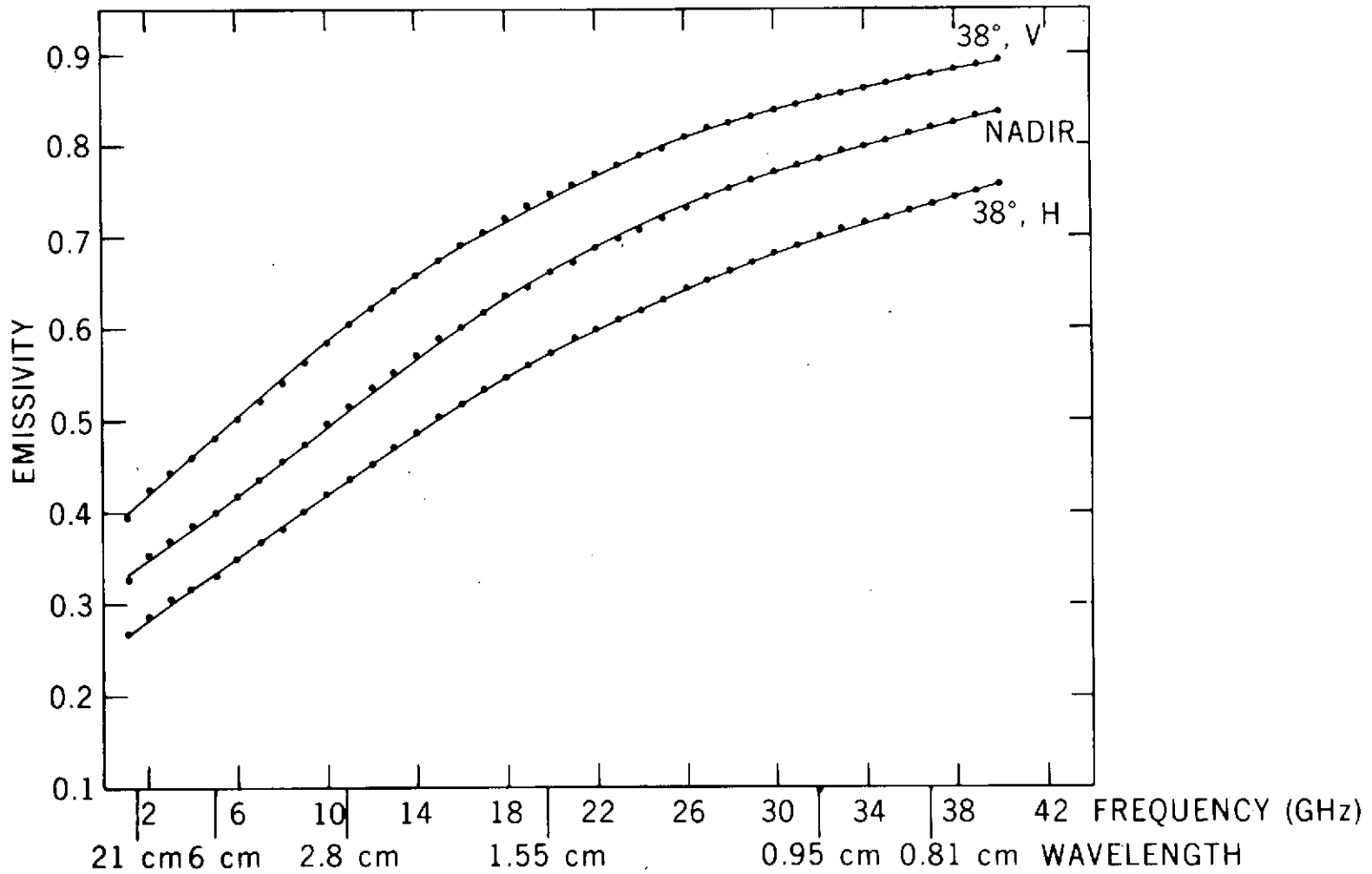
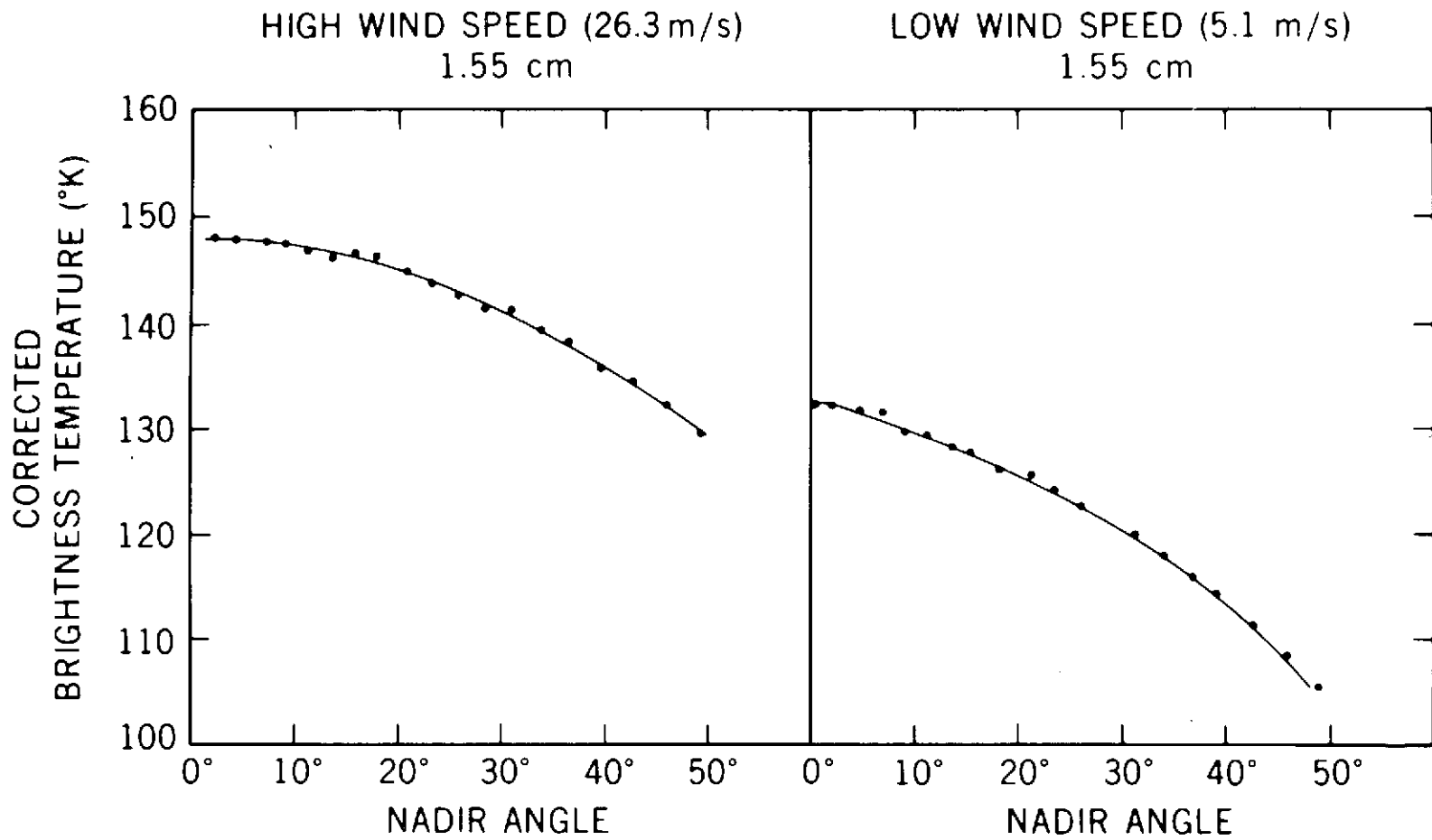Figure 6.4. Calculated Emissivity of the Boundary Layer Between the Sea and Air as a Function of Frequency and Wavelength

Figure 6.5. Angle Dependence of T_B^{sea} at 1.55 cm for High and Low Wind Speeds
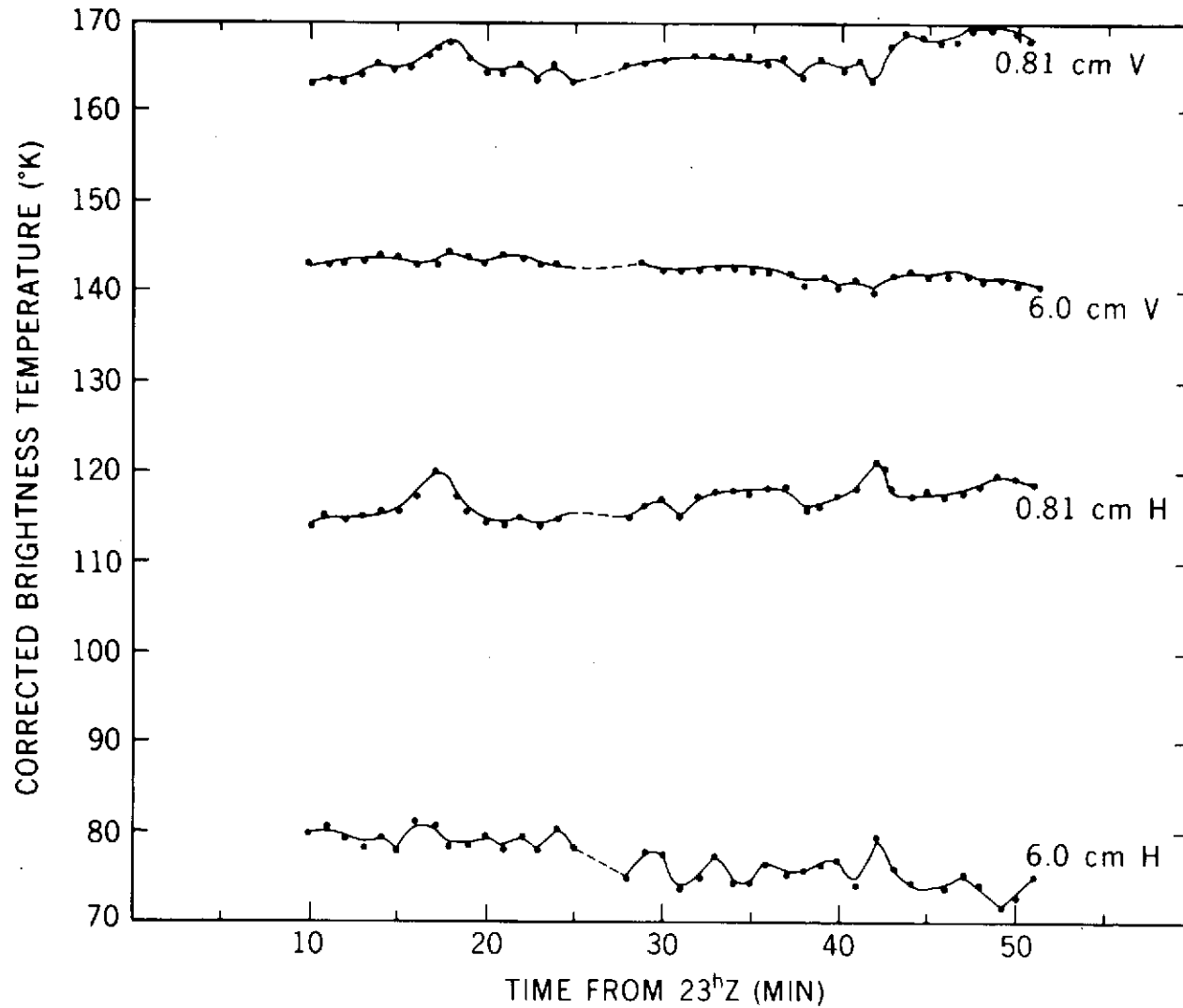
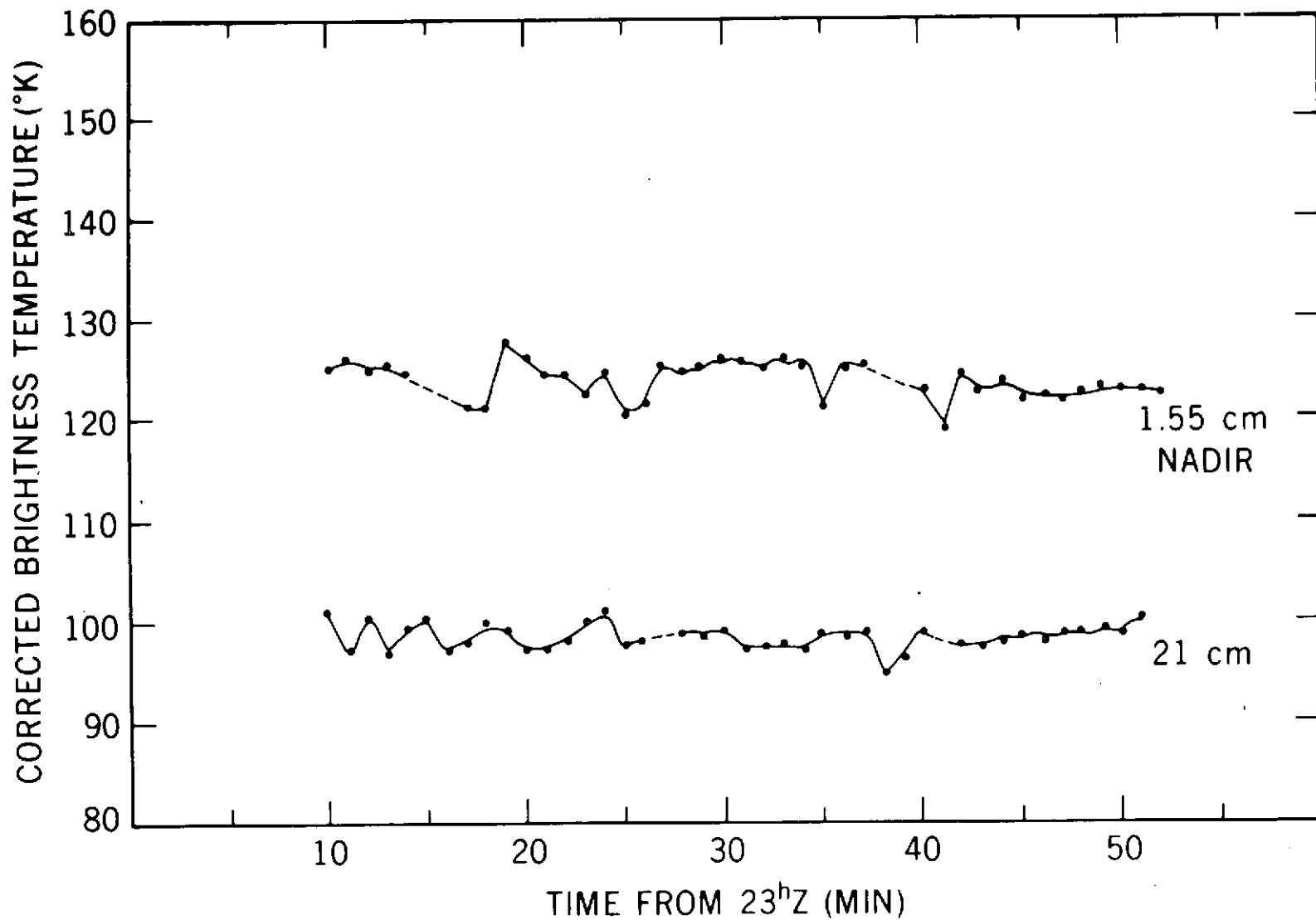Figure 6.6. 6.0 cm and 0.81 cm H and V, One Minute Averages From 23/24 February, 155 m Altitude

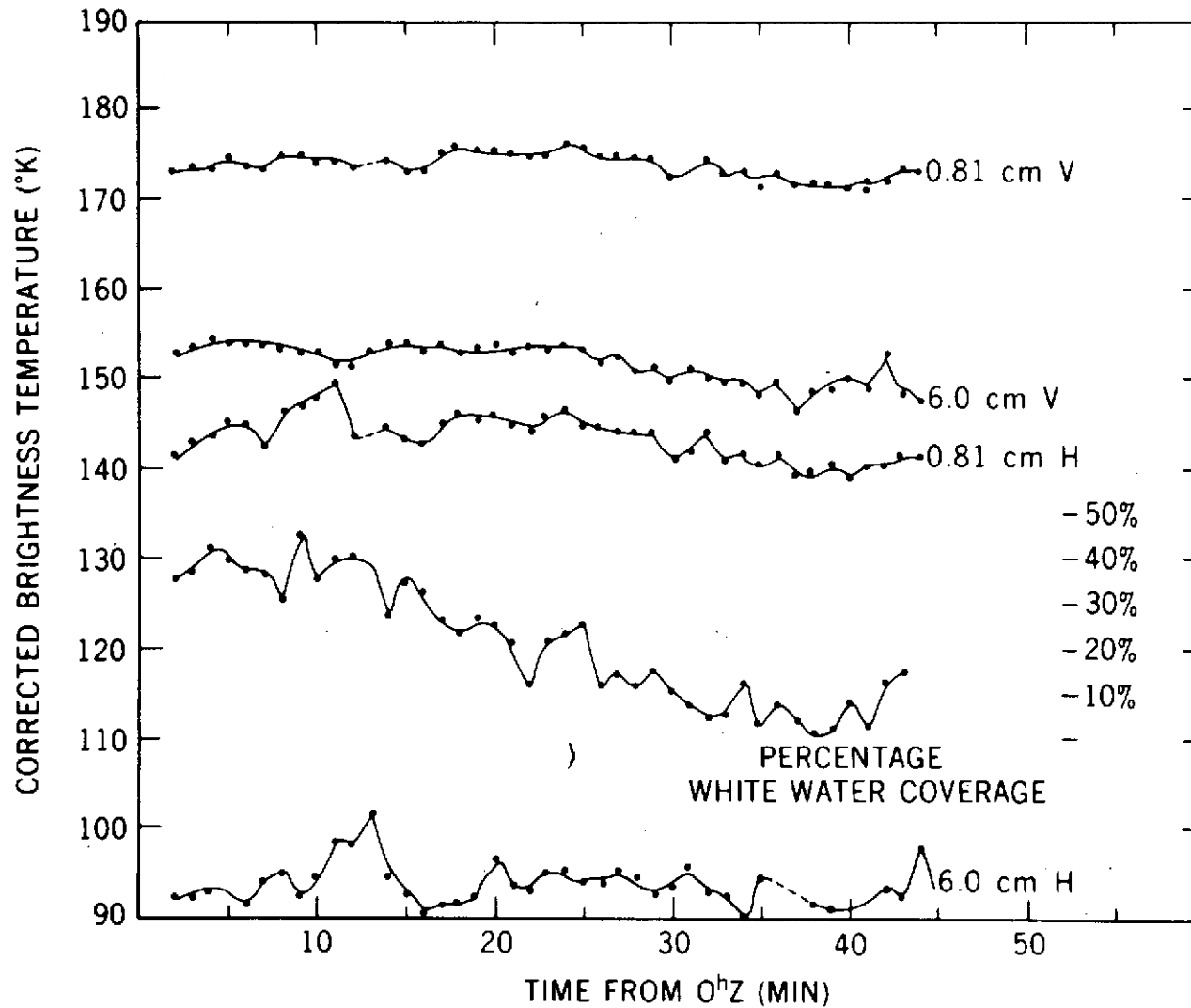Figure 6.7. 21 cm and 1.55 cm Nadir, One Minute Averages From 23/24 February, 155 m Altitude

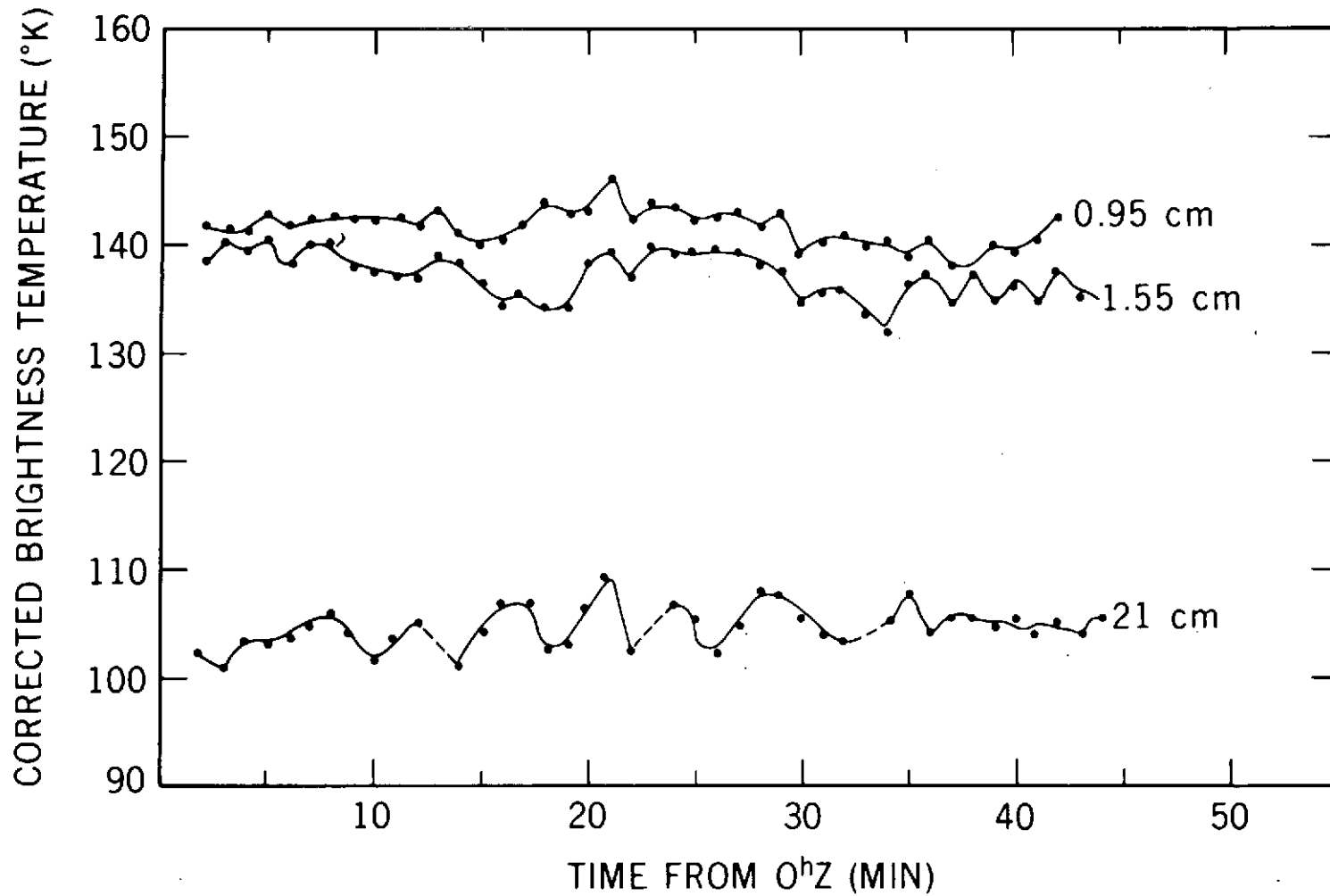Figure 6.8.   6.0 cm and 0.81 cm H and V, One Minute Averages From 7/8 March, 155 m Altitude
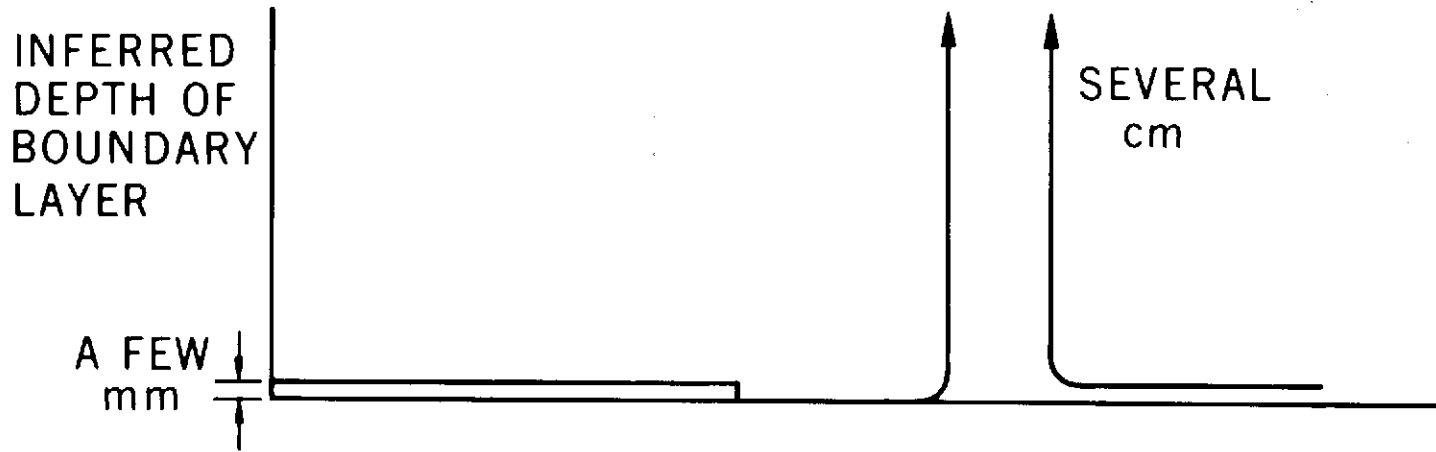
Figure 6.9. 21 cm, 0.95 cm and 1.55 cm Nadir, One Minute Averages From 7/8 March, 155 m Altitude

INFERRED
DEPTH OF
BOUNDARY
LAYER

SEVERAL
cm

A FEW
mm

WHITE CAP

FOAM STREAKS

FOAM STREAKS

WATER SURFACE

Figure 6.10. Cross Section View of Model Sea-Air Boundary Layer

The
End
9/9/72